1-10-2013

Computational Fluid Dynamics based redesign of the Magnetically Levitated Blood Shearing Device for Hemolysis Predictions

Shanoo Revankar

Computational Fluid Dynamics based redesign of the Magnetically Levitated Blood Shearing Device for Hemolysis Predictions

By

SHANOO REVANKAR

A Thesis Presented in Partial Fulfillment of the Requirements for

the Degree of *Master of Science* in Mechanical Engineering

Department of Mechanical Engineering

Rochester Institute of Technology

Kate Gleason College of Engineering

Department of Mechanical Engineering

Rochester, NY, 14623

January 10, 2013

Approved by:

Dr. Steven W. Day _____

Department of Mechanical Engineering (Thesis Advisor)

Dr. Risa J. Robinson _____

Department of Mechanical Engineering

Dr. Karuna Koppula _____

Department of Chemical Engineering

Rochester Institute of Technology

Kate Gleason College of Engineering

Department of Mechanical Engineering

Rochester, NY, 14623

Acknowledgment

I want to thank Dr. Steven Day for giving me an opportunity to work on the blood pump project and his guidance and patience throughout my work. I also want to acknowledge the FDA Critical Path Initiative Project for providing financial support for this work. I would also like to thanks the rest of my committee: Dr. Risa Robinson and Dr. Karuna Koppula for their guidance and help.

I want to thank the staff at the Mechanical Department: William Finch, Diane Selleck, Diedra Livingston, Vanessa Mitchell and Jill Ehmann, Hillary McCormick for all their support.

Lastly, I want to thank Yoshita Revankar (mother) and Kalidas Revankar (father) and my brother Dwitiy for their love and support.

Dedication

This work is dedicated to Dr. Steven Day for his kind support and help throughout my time at, The Biomedical Device Lab at Rochester Institute of Technology.

And

To my mother and father

Abstract

Annular Couette type blood shearing devices have been used for analysis of blood damage related to device induced shear stress. Two important factors in predicting cell damage are the magnitude of stress and the duration of exposure to the stress. Several previous devices for blood damage analysis consist of concentric cylinders with one cylinder rotating and the other held stationary. This generates a Couette flow between the cylinders. In a typical apparatus, the shear stress can be controlled by varying the rotation of the inner cylinder and the exposure time can be controlled by controlling the axial velocity of the fluid through the device. The higher the rotational speed the higher the magnitude shear stress. However, apparati are susceptible to a flow instability at high rotational speeds. This flow instability is characterized by toroidal vortices and may be predicted by the Taylor number, which is related to the fluid viscosity, gap and rotational speed. If the critical Taylor number is exceeded, Taylor vortices will exist. Taylor vortices are undesirable because blood cells may become entrapped in these vortices and increase exposure time thus leading to distorted hemolysis data. Because shear stress is also a function of the gap and rotational speed, the avoidance of Taylor vortices places limits the shear stress and exposure times that can be achieved in this type of a device. Changing the gap size and shape affects the formation of Taylor vortices. In this study several variations of the gap shape and size of the flow path of a blood shearing device are investigated numerically in order to find the geometry that has a physiologically relevant range of shear stress and exposure

time while avoiding Taylor vortices. The proposed design will be used in future studies to study the effect of shear stress on the blood for a certain exposure time.

Table of Contents

List of Figures

List of Tables

List of Equations

List of Symbols and Acronym's

Chapter 1

Introduction

1.1 Background and overview of thesis

Cardiovascular prosthetic devices serve as a lifesaving alternative to persons suffering from severe cardiovascular diseases. These devices are prone to shear induced hemolysis. Although the precise mechanism of hemolysis still remains elusive, many studies have shown that it is related to the shear history to which the blood is exposed [2]. The magnitude of shear stress and exposure time play an important role in blood damage.

It is important in the design of blood contacting medical devices to be able predict the extent of shear induced damage. This is particularly true for high flow devices such as prosthetic valves and pumps where regions of high stress are unavoidable. One of the more common models of hemolysis prediction is based on the power law form $D = A\tau^{\alpha}t^{\beta}$ where D is damage, τ- shear stress, t- time. The co-efficient A, α, β are determined by regressing the experimental data. [2]. Understanding how each of the parameters involved affect blood damage is of crucial importance to reduce clinical hemolysis. Previous studies have concentric cylinder viscometers for hemolysis study due to their efficiency in evaluating shear stress and exposure time independently. It is important to maintain a uniform shear stress in the shearing device for accurate measurement of hemolysis. Unfortunately, secondary flow effects such as formation of eddy, vortices, and regions of localized shear stress, from bearings or other mechanical

components may induce artifactual effects on the cells. In one of the more common geometries of rotating concentric cylinders the flow is susceptible to Taylor vortices which does not allow for uniform level of shear stress and exposure time.

The Mag-lev shearing device designed at RIT for blood damage analysis avoids regions of secondary stress, such as bearings and other mechanical components, but, like all rotating concentric cylinder apparatuses, is susceptible to Taylor vortices at high rotational speeds. In this work the flow path of the Mag-lev blood sharing device is redesigned in order to have least number of vortices.

The Mag-lev shearing device has an inner cylinder rotating within a stationary housing. The inner cylinder levitates inside the housing due to magnetic action and its rotation is controlled by an external control system. The device has an inlet and an outlet maintained at a certain pressure difference. The flow path of the shearing device consists of a shearing gap. This shearing gap is where the blood is sheared. The gap size between the inner rotating and outer stationary housing is maintained very small (0.125mm) which allows the blood passing through to be exposed to high levels of shear stress (shearing the blood) caused due to rotation of the inner cylinder. The gap size upstream and downstream the shearing gap/thin gap is maintained wide (1.35mm). At high rotational speeds this wide gap is affected by Taylor instability when the Taylor number associated with the rotation exceeds the critical Taylor number (Ta_{cr}= 1708).

This does not allow for accurate hemolysis predictions and thus a redesign of this wide gap is undertaken to analyze the effect on the Taylor vortices and accurate hemolysis predictions.

The first part of the thesis deals with the redesign of the wide gap size of the device upstream and downstream the shear gap. Four different designs were tested before the final design was achieved. All the designs from Design 1 to Design 4 have a different gap shape upstream and downstream the shear/ thin gap region. Design 1 is the original wide gap design. Design 4 is the final design. The criteria set for design modification was to achieve least number of Taylor vortices. The analysis to determine the formation of vortices was done using ANSYS Fluent. Since Design 4 had the least number of Taylor vortices it was further analyzed for hemolysis analysis. Hemolysis analysis was conducted using Eulerian scalar transport and Lagrangian power law models and using different sets of coefficients in literature. The values obtained through analysis are then compared to experimental results taken from Taskin *et.al*. 2012. The procedure followed for the design modification and analysis is shown in the flow chart below, Figure 1.1.

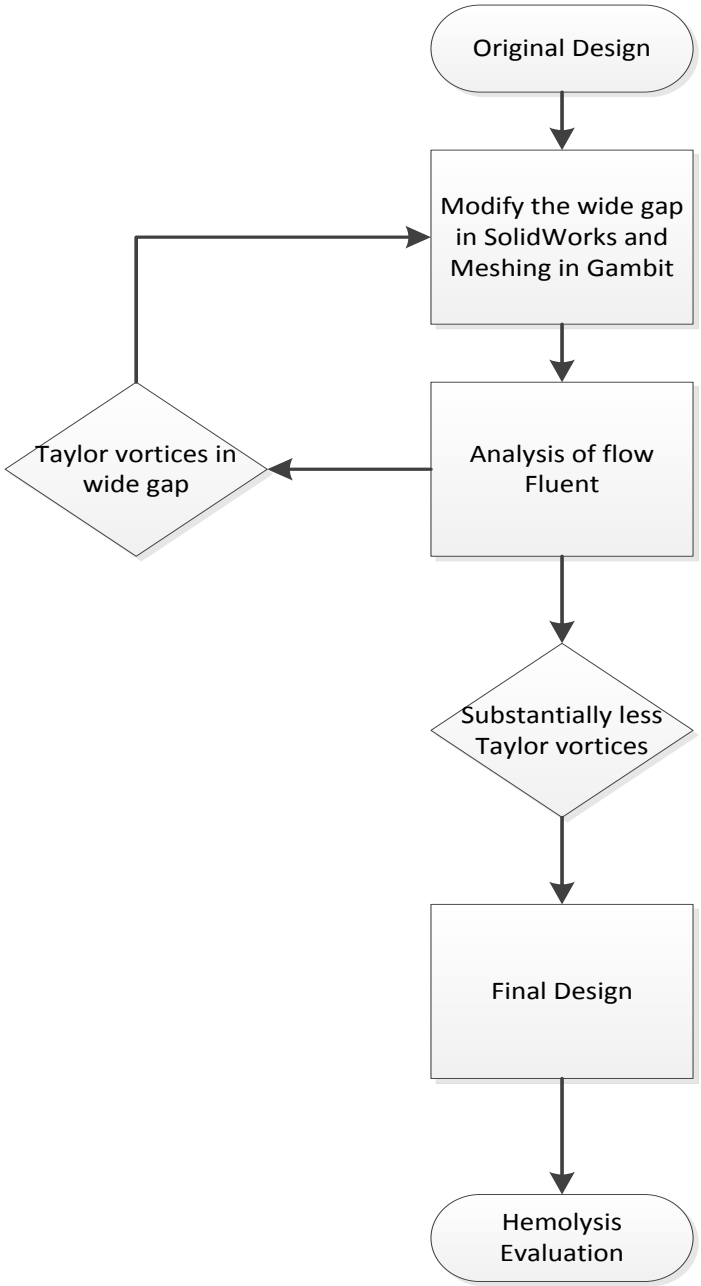

Figure 1.1 Flow chart of design refinement

Literature review

1.2 Blood

1.2.1 Blood and its properties

Blood is a mixture of cells and plasma. The cellular material consists of red blood cells, white blood cells and platelets. Apart from this water, amino acids, proteins, carbohydrates, lipids, hormones, vitamins, electrolytes, dissolved gases, and cellular wastes are also a part of blood. Plasma constitutes 54.3% of the blood while red blood cells make up 45% and white blood cells only 0.7%. Moreover, plasma is mostly 92% water along with some nutrients and waste products[2].Hemoglobin, a protein pigment found in the red blood cells is responsible for transporting oxygen and removing carbon dioxide form them. Density of blood is 1050 kg per cubic meters. It is a non-Newtonian fluid and its viscosity is taken as 3.5cP [3] **.**

1.2.2 Blood damage/Hemolysis

Blood is damaged when it flows through a rotating blood pump due to due the physiological flow fields that are present within the device. Two major types of blood damage occur known as thrombosis and hemolysis and the fluid shear near the walls and in the flow field play an important role in damaging the blood [4]. In this study we will be concentrating only on hemolysis. Shear stress and the exposure time play a significant role in damaging the flowing blood. Thus hemolysis is a function of shear stress and the exposure time to this stress.[5]. This

study is related to the damage caused due to shear stress and does not deal with the causes of damage for e.g. Surface damage.

1.2.3 Empirical studies on blood damage

This section gives a general overview of the empirical studies conducted in literature. The details of the experimental setup used in literature useful for this work are discussed later in Lagrangian Approach to Hemolysis in Section 1.6.1 in Methods of Hemolysis Evaluation.

In 1972, Leverett and Hellums have evaluated the blood damage in a rotational viscometer. They took into consideration the effects of solid surface interaction, mixing of sheared and unsheared layers, cell-cell interaction and viscous heating. Induced shear stress and exposure time are two very important parameters in the evaluation of blood wetted rotational devices. It was shown that the shear stress and the exposure time are divided into two different regimes. In the regime of relatively low exposure time and shear stress, there is relatively little damage and the damage is dominated by solid surface interaction. In the other regime at high stresses and exposure times, stress effects alone dominate and very high rates of hemolysis occur. It was found that there is a threshold value of 1500 $dynes/\ cm^2$(150Pa) above which the extensive cell damage is directly due to shear stress. The study summarized the effect of exposure time on threshold shear stress and the effect of shear stress on hemolysis. Figure 1. 2 shows the regimes detected by Leverett and Hellums. Figure 1.3 gives a summary of effect of shear stress on hemolysis for different types of exposure found in literature.

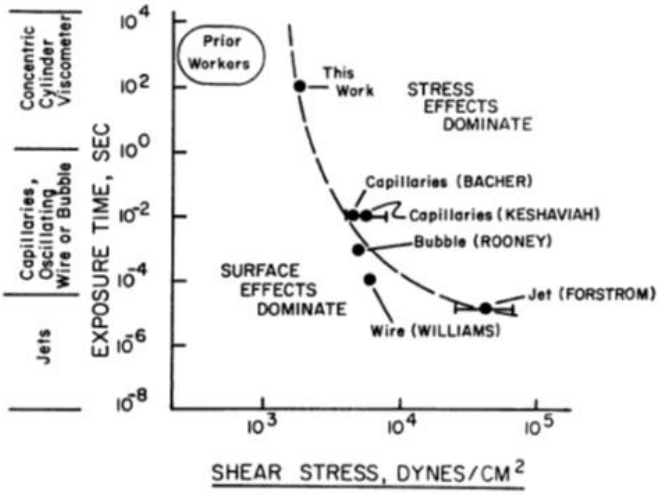

Figure 1. 2 Regimes of Shear stress and Exposure time for hemolysis by Leverett and Hellums [34]

SUMMARY OF EFFECT OF SHEAR STRESS ON HEMOLYSIS

Type of exposure	Order of magnitude of exposure time	Threshold level of damage	References and comments
	sec	*dynes/cm²*	
Turbulent jet	10^{-5}	40,000	Forstrom (1969) and Blackshear (1971)
Oscillating wire	10^{-4}	5600	Williams et al. (1970) (human and canine)
Oscillating bubble	10^{-3}	4500	Rooney (1970) (human and canine)
Capillary flow	10^{-3}	5000	Bacher and Williams (1970) (bovine blood)
Capillary flow	10^{-2}	4500–7000	Keshaviah (1970) and Blackshear (1971) (canine blood)
Concentric cylinder	10^{3}	1500	This work
Concentric cylinder, maximum stress, 600 dynes/cm²	10^{2}–10^{3}	Relatively little hemolysis per unit time	Shapiro and Williams (1970) (surface effects dominate)
Concentric cylinder, maximum stress, 250 dynes/cm²	10^{3}	Relatively little hemolysis per unit time	Knapp and Yarborough (1969) (surface effects dominate)
Concentric cylinder, maximum stress, 600 dynes/cm²	10^{3}	Relatively little hemolysis per unit time	Steinbach (1970) and Blackshear (1971) (surface effects dominate)

Figure 1.3 The Effect of Shear stress on Hemolysis[2]

In 1980 G.Heuser and R.Opitz investigated hemolysis using porcine blood by allowing it to be exposed to defined shear stresses of short duration. Shear stresses $\tau < 7 * 10^5\ dyn/\ cm^2$ (700 Pa) or 700 N/ m^2 and shearing times t_B > 3*$10^{-3} seconds$ which is 3 msec, can be obtained. The range of shear stresses and shearing times investigated are shown in Figure 1. 4

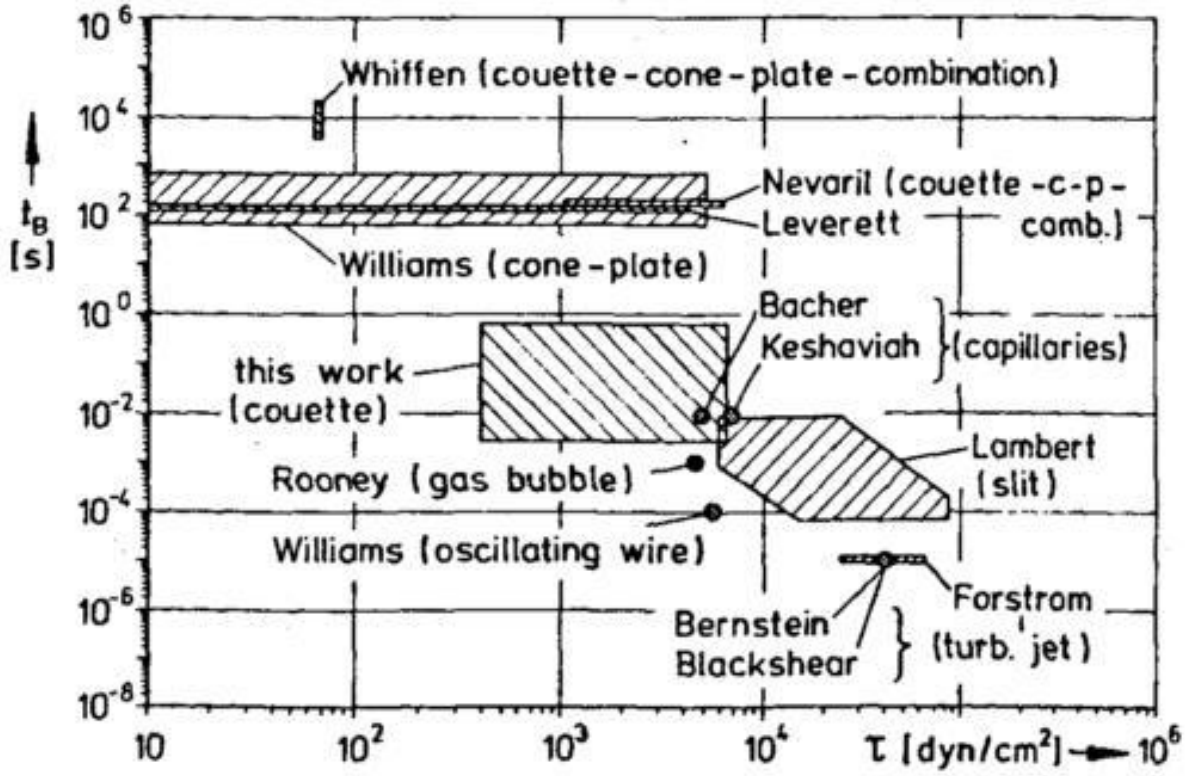

Figure 1. 4 Range of shear stresses and shearing times examined by Heuser. *et .al* [10]

Heuser also stated there are two important requirements that required to be fulfilled in order for the system to investigate shear induced hemolysis.

1. Stresses caused by the rotation have to exceed that caused by the Poiesuelle flow.

2. By limiting the flow condition to laminar flow. This way the shear stress applied is accurate. This also prevents any repeated loading of blood cells with shear stress in the vortex motion of the flow.

Experimental hemolysis was conducted by Wurzinger in 1986 using a Couette viscometer setting keeping the flow in the laminar region. [6] The viscometer consisted of two concentric cylinders with a 110μm (0.11mm) wide gap. The inner cylinder rotated upto 8000 rpm generating a shear stress of 255N/m^2(255Pa) with the least stress generated being 57 N/m^2. (57Pa). A dosing pump was used to propel the platelet suspension from a thermostated reservoir at adjustable speeds through the shearing gap thus controlling the time spent by the platelets within the field of high shear forces. No Taylor vortices were generated in the experiment. In 1990 an empirical power law correlation between shear stress and exposure time was given by Giersiepen to determine hemolysis [7]. They used the experimental data from Wurzingers experiment's in 1986 was incorporated into a mathematical correlation, which served as a basic model for the estimation of blood damage. In 2003 Paul.et al conducted experiments that covered a wider range of exposure times and shear stresses that had been covered in any single prior study. Figure 1. 5 shows the experimental set up for the experiment. Experiments are conducted at exposure times from t_{exp} =25-1250msec. And shear rates ranging from 30Pa up to 450Pa. ensuring a Taylor –Vortex free flow over a broad range of shear rates and exposure times. The width of the shear gaps is maintained H= 0.15 mm. At maximal flow the axial Reynolds number was Re = 40. The analysis was conducted in laminar conditions and Taylor number was

maintained below $Ta_{cr} = 1706$. Significant blood damage was observed for shear stresses of $\tau \geq 425\ Pa$ and exposure times of $t_{exp} \geq 620\ msec$.Maximum hemolysis within the investigated range is IH=3.5%. The blood damage detected in this study was indicated that the erythrocyte damage by laminar Couette flow had been widely overestimated in previous studies. The damage detected in previous studies was above 10 % for shear stress levels of upto700 Pa and exposure time of up to 600 msec. Figure 1.6 shows the Hemolysis correlation found in Paul *et.al's* study.

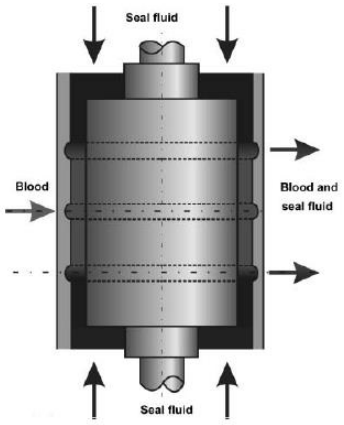

Figure 1. 5 A Couette Viscometer used by Paul.*et.al*.10

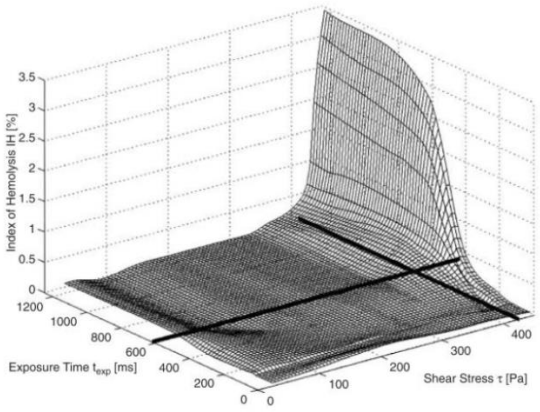

Figure 1.6 Paul's Hemolysis Correlation for flow induced blood damage up to 450Pa and exposure times of 1238ms [9]

1.2.4 Published Threshold Value

In addition to the studies summarized here, other studies have attempted to characterize the relationship between the threshold shear stress and exposure time required for blood damage. A summary of the published threshold shear stress values is given in Table 1.1

Table 1.1 Summary of Literature Threshold values [2]

	Flow condition	Blood Type	Exposure Time [s]	Shear Stress [Pa]	Name	Year
1	Concentric Cylinder		1.00E+03	25	Knapp and Yarborough	1969
2	Concentric Cylinder		1.00E+02	60	Steinbach	1970
3	Concentric Cylinder		5.50E+02	60	Shapirot and Williams	1970
4	Concentric Cylinder		1.00E+02	150	Leverett	1972
5	Concentric Cylinder		6.00E-01	700	Heuser	1980
6	Concentric Cylinder	human	7.00E-01	255	Wurzinger	1985
7	Concentric Cylinder		6.00E-01	400	Hasenkam	1988
8	Concentric Cylinder	porcine	6.20E-01	425	Paul	2003
9	Concentric Cylinder	porcine	1.20E+00	350	Paul	2003
10	Concentric Cylinder	porcine	2.40E+02	250	Sutera and Mehrajardi	1975
11	Concentric Cylinder	human	1.00E+00	250	Giersiepen	1990
12	Capillary	bovine	1.00E-03	500	Bacher	1970
13	Capillary	canine	1.00E-03	575	Bacher	1970
14	Oscillating Wire	human and canine	1.00E-04	560	Williams	1970
15	Oscillating Wire	human and canine	1.00E-03	450	Rooney	1970
16	Turbulent Jet		1.00E-05	4000	Blackshear	1970
17	Turbulent Jet	human	1.00E-03	400	Sallam and Hwang	1984
18	Turbulent Jet		1.00E-03	800	Lu	2001
19	Pump		1.00E-03	600	Grigioni	1999
20	Pump		1.00E-01	500	Song	2004
21	Pump		1.00E-03	1000	Mitoh	2003
22	Pump		3.00E-03	300	Apel	2001

1.2.5 Predictive relationships of Hemolysis

Assuming that shear stress (τ) and exposure time (t_{exp}) are the only two factors in hemolysis, they should be independently evaluated w.r.t their role in hemolysis of blood. Thus for studying blood damage it is essential to control shear stress and exposure time independently. A viscometer with a Couette setting fits the requirements since the shear stress can be controlled by controlling the rotational rate and the exposure time can be controlled by controlling the flow rate inside the device. The Couette setting is made up of concentric cylinders with a gap in between them. In 1986, Wurzinger obtained data for hemolysis in a rotating viscometer. He documented that his shear stress was less than 250 Pa with exposure time below 700 msec [8]. In 1990, Giersiepen came up with the Power law model based on Wurzinger's experimental data. Giersiepen assumed that Reynolds stresses due to turbulent flow dominated the viscous stresses due to friction occurring in the pump. Therefore, he only accounted for Reynolds stresses.

On the other hand, Apel et. al discovered that on average turbulent stress was lower than viscous stress in the pump gap region and concluded that the viscous stresses are more important than the turbulent stresses.[9]

In 1980, Heuser obtained constants for Power law model by regression analysis of experimental data taken with an exposure time of 0.0034 to 0.6 seconds for shear stresses between 40 and 700 Pa in a Couette viscometer [10]. The experiment was conducted on Couette viscometer in a laminar flow regime.

Heuser model is based on experimental data that is in the range of shear stress, which is comparable to the flow conditions in blood pumps while shear stress in Giersiepen model ranges below 250 Pa. Similarly, in 2012, Taskin *et. al*. published new constants for the blood damage model. They are shown in the equations below

Equation 1 1 Giersiepen Power Law model

$$D = \frac{\Delta Hb}{Hb} = 3.62 \times 10^{-5} \tau^{2.416} \Delta t^{0.785}$$

$$\tau - Viscous\ stress$$

$$\Delta t - Exposure\ time$$

$$D - Blood\ damage$$

Equation 1 2 Heuser Power Law model

$$D = \frac{\Delta Hb}{Hb} = 1.8 \times 10^{-7} \tau^{1.991} \Delta t^{0.765}$$

$$\tau - Viscous\ stress$$

$$\Delta t - Exposure\ time$$

$$D - Blood\ damage$$

Equation 1 3 Taskin Power Law model

$$D = \frac{\Delta Hb}{Hb} = 1.23 \times 10^{-5} \tau^{1.9918} \Delta t^{0.6606}$$

$$\tau - Viscous\ stress$$

$$\Delta t - Exposure\ time$$

$$D - Blood\ damage$$

1.3 Taylor Instability

1.3.1 Formation of Taylor vortices

The flow between rotating cylinders is susceptible to a transition from the stable Couette flow transitions to unstable secondary flow characterized by toroidal vortices. This is predicted by the Taylor number, which accounts for the formation of Taylor vortices. The Taylor vortex flow is shown in Figure 1.7. In the case of fixed cylinder geometry (constant diameter) with a known fluid (constant density and viscosity), this a result of the angular velocity of the inner rotating cylinder. The flow this nature is known as Taylor-Couette flow. The critical Taylor number is about 1708 for a rotating inner cylinder and stationary outer cylinder which was established by G.I. Taylor in his groundbreaking paper in 1923. In his experiments the length of

the cylinders in the apparatus was maintained 90 cm (0.09m) long to eliminate the end effects. The outer cylinder was 4.035 cm radius (0.0435 m). The thickness of the layer of liquid between the outer and the inner cylinder was less than 1 cm (0.001 m) for all experiments. Three different value's (R_1 = 3.00 cm, 3.80 cm and 3.55 cm) inner radii were considered. The Taylor number for different experimental set up varies however the critical Taylor number remains the same. In 1958 hot wire measurements were used by Kaye and Elgar to establish four regions for the existence of Laminar flow with and without vortices and Turbulent flow with and states that occur systematically with the increasing rotation rates of the inner cylinder. Figure 1. 8, Figure 1. 9 summarize the study.

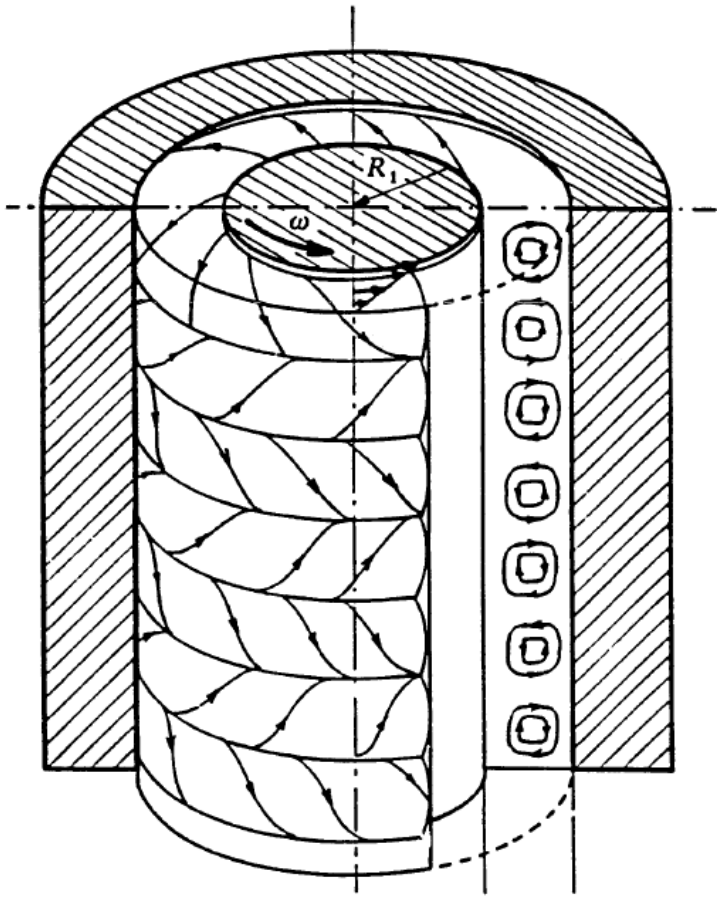

Figure 1.7 Taylor Vortex flow

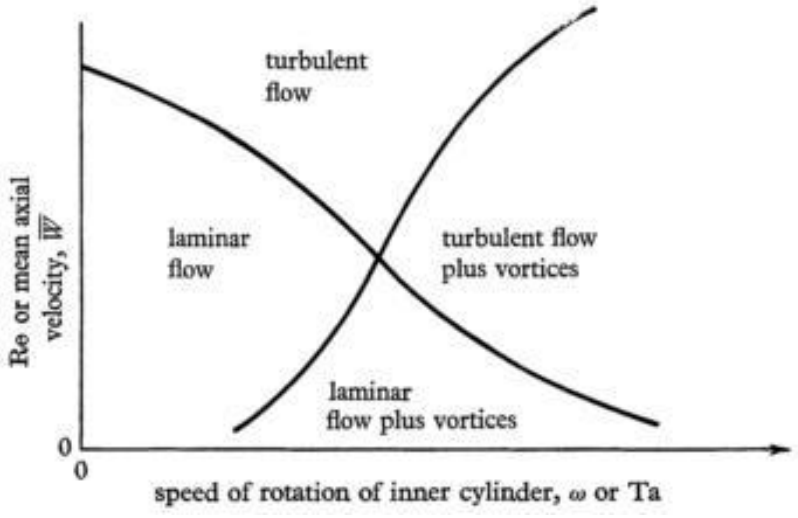

Figure 1. 8 Schematic representations of modes of flow in an annulus with an axial flow (Kaye & Elgar) [11]

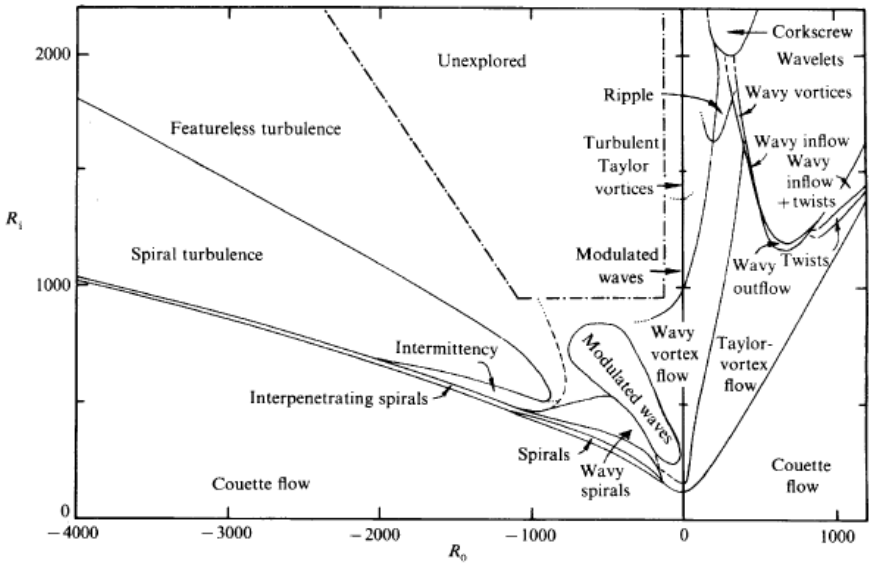

Figure 1. 9 Regimes observed in flow with independently rotating cylinders.[11]

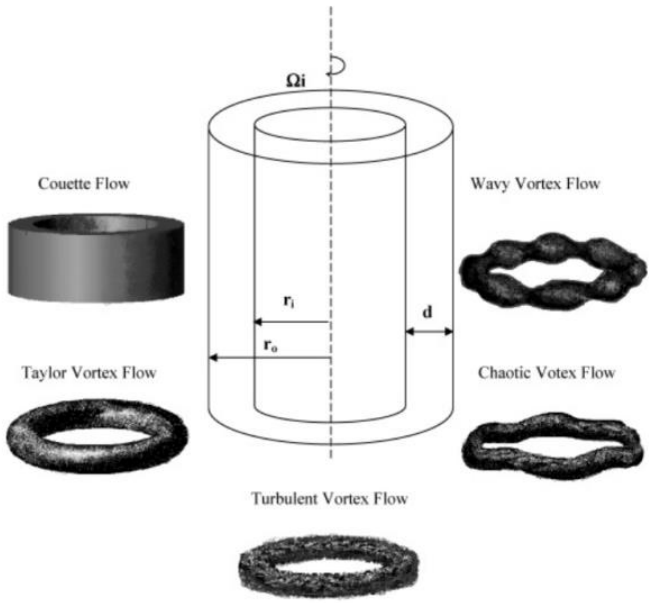

Figure 1 .10 System of concentric cylinders and various vortex patterns in the absence of an axial flow [35]

As the Taylor number increases beyond the critical Taylor number the Taylor vortex flow changes to wavy vortex flow (WVF) $Ta_{Cr} < Ta < 100Ta_{Cr}$ and finally into turbulent Taylor vortex flow (TTVF) $Ta > 1000\ Ta_{Cr}$. Figure 1 .10 shows the various patterns arising with the increasing speed.

1.3.2 CFD based flow visualizations

One of the important aspects of this work is to simulate Taylor vortices numerically. Thus it is essential to study Taylor vortex flow simulations in literature. In 2000 Baier G. used CFD based flow visualization to predict the magnitude of the vortex velocities and behavior in turbulent regimes for the development of a liquid-liquid extraction device based on the Taylor Couette flow. In his analysis he used Fluent to simulate the Taylor Couette flow.[12]. In 2003 Wavy vortex flow and turbulent Taylor vortex flow in the annular region of co-rotating cylinders was simulated by Haut et al. in CFD using the k-Epsilon model to account the turbulence parameters. In 2007 Deshmukh et.al used CFD simulation to predict the flow patterns over a large range of Reynolds and Taylor's numbers in the annular region of a centrifugal extractor. This data was then compared to the PIV and LDV data from experiments. Fluent 6.3 software was used for simulations on a 2-D axisymmetric grid. The results are summarized in Figure 1.11 . In 2008 Nyers et .al used Fluent 6.3 software along with search algorithms to detect and track vortices. The graph search method was used for vortex detection and the flood fill algorithm tracks the detected vortices. In 2008 Desevaux, P. used Fluent 6.3 to visualize the

formation and the propagation of Taylor vortices in a Taylor Couette flow of air with the sudden start of the inner rotating cylinder. These results were then compared to the results obtained from laser sheet tomography. The results of the CFD simulation agreed very well with the experimental. Thus the comparison of the experimental and the numerical results validated the CFD model. The figure below shows the propagation of the vortices in the annulus of the concentric cylinders used for this experiment.

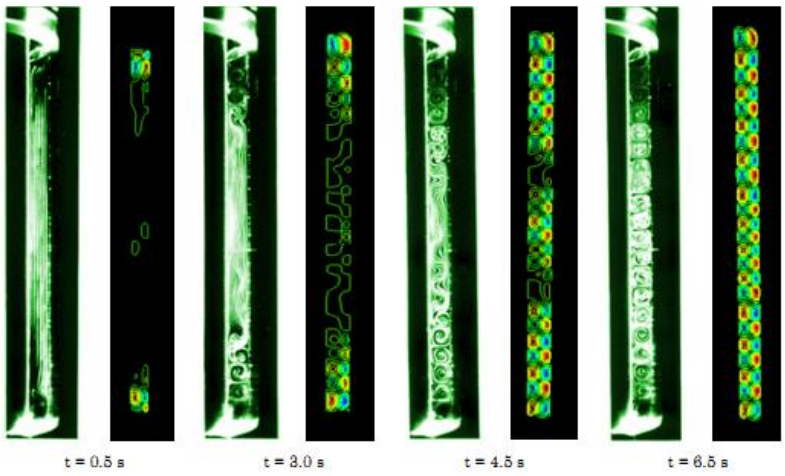

Figure 1.11 Series of flow visualizations showing the progression of Taylor cells along the annular space. [36], images on the left show results of laser tomography and CFD simulation on the right for increasing time

In 2010 H. Oualli et.al used the CFD based flow visualization approach for analyzing hydrodynamic stability in an annular space of a sinusoidal (a cylinder whose radius varied sinusoidally) inner rotating cylinder and an outer stationary cylinder. They defined a parameter

$\epsilon = \frac{R_2 - R_1}{R_1} = \Delta r / R_1$ where R_1 and R_2 are the maximum and minimum radii of the inner cylinder. This parameter was compared to the change in the critical Taylor number and the axial vorticity of the Taylor Couette flow. The objective was to find the flow response to the imposed boundary condition of the inner cylinder. It was found that as a result of the oscillations, axial and radial symmetries were broken, significant reduction in the maximum vorticity (ϵ) values is achieved and substantial enhancement of the transition from the Taylor-Couette basic flow to the vortical flow was observed. The experimental results were validated using numerical solutions where the apparatus was meshed in Gambit and analyzed in Fluent.[13]

1.3.3 Delaying the Taylor flow transition.

The transition from laminar Poiseuelle flow in a concentric cylinder to Taylor-Couette flow can be prevented by certain modifications. Researchers in the past have tried to delay the transition or the appearance of the first vortex by imposing a through flow superimposed on ordinary Taylor-Couette flow.[8], [14] Another way of delaying the transition of the Taylor vortex flow is by modulating the speed of the inner cylinder[8]. Recently Hu et.al [15], conducted a study to determine the effect of moving the inner cylinder in a sinusoidal fashion on the critical Taylor number. It was found that it was possible to raise the critical number by oscillating the through flow.

In 1999 Denne and Wimmer analyzed the travelling Taylor vortices in the conical cylinders and cone cylinder combination. They concluded that for a cone –cylinder combination

,when the vortices travel through the non-constant annulus and come to the larger radii region and consequently smaller gap sizes, the vortices decay[16]. In 2000 Wimmer and Zierep examined the transition of vortices with the change in the apex angles for cone-cone geometries. They noted that, for circular cylinders Taylor vortices appear at critical conditions at Ta=42.5 and remain wavy or turbulent till Ta=3160. However we the conical case the critical value for onset of Taylor vortices is higher and this causes a delay in the onset of vortices. Thus transition to Taylor vortex region takes place at a higher Taylor number[17]. They summarized the regime for the existence of Taylor vortices as shown in Figure 1.12.

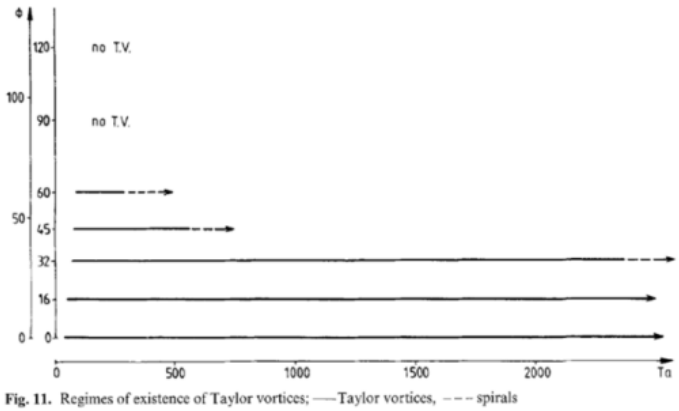

Fig. 11. Regimes of existence of Taylor vortices; —Taylor vortices, – – – spirals

Figure 1.12 The following table shows the regime of existence for the Taylor vortices.

The x axis shows the Taylor numbers while the y axis is the apex angle [17]

Richard M Lupetow [18], in his study on stability and experimental velocity field in Taylor coquette flow with axial and radial flow noted that how a combined axial and radial flow help to stabilize the overall flow. Thus the transition to Taylor vortex flow is delayed.

1.3.4 Effect of Axial flow on Taylor Couette flow

The stability of a viscous fluid between two concentric rotating cylinders with an axial flow was investigated by R.C Diprima in 1960. The critical Taylor number is computed for small Reynolds number associated with the axial flow. It was observed that the critical Taylor number increases with increasing Reynolds number.[19] The effect of axial flow on the critical Taylor number is not considered in this study.

1.3.5 Taylor Number and Gap Independence

The critical Taylor number was given by G.I. Taylor as 1708 for all ratios of inner to outer cylinder. The Taylor number for a given system varies according to the gap between the inner and outer cylinder however the critical Taylor number remains constant i.e. $Ta_{cr} = 1708$. Thus the critical Taylor number used for this work is 1708 and is gap independent.

1.4 Mag-Lev Shearing Device

1.4.1 Motivation

An important feature of a blood shearing device is that blood cells should be exposed to a uniform shear stress for a uniform exposure time. Thus a good design a blood shearing device will allow one to apply uniform shear stress for a uniform exposure time. Most of the Couette type blood shearing devices used in the literature above use seals and bearings in their design. These seals and bearings cause undesirable shear concentrations leading to non-uniform shear stress exposure. Thus they overshadow hemolysis within the desired "shear" region[20].

The following features can be identified for a blood shearing device with respect to applying uniform shear stress exposure history.

1. The device should not generate unnecessary shear stresses
2. It should be able to control shear stress and exposure time independently

1.4.2 Working of the Mag-lev shearing device

The Mag-Lev uses magnetically levitated system for its rotation. It consists of a bladeless impeller rotating within a stationary housing. It has a bump at the center for the application of shear stress. The distance between the bump the bump region and the outer housing is 0.125mm and a Couette flow condition is assumed for the flow in this gap. The applied shear stress can be controlled by controlling the rate of rotation of the inner cylinder, while the exposure time can be

controlled by the axial flow rate. This way the design generates a uniform shear stress in the shear gap region for a programmed exposure time.

1.4.3 Maglev shearing device and flow settings

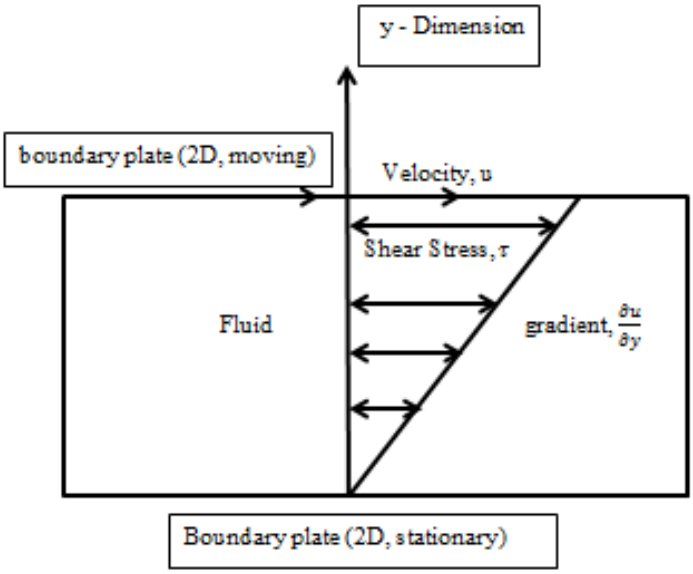

Figure 1.13 Simple Couette configuration using two infinite plates

The important aspect about this setting is that we have a constant shear stress being applied throughout the flow domain. This helps the device to apply a constant shear stress on the blood flowing through. The uniform shear stress applied is shown in the Figure 1.13

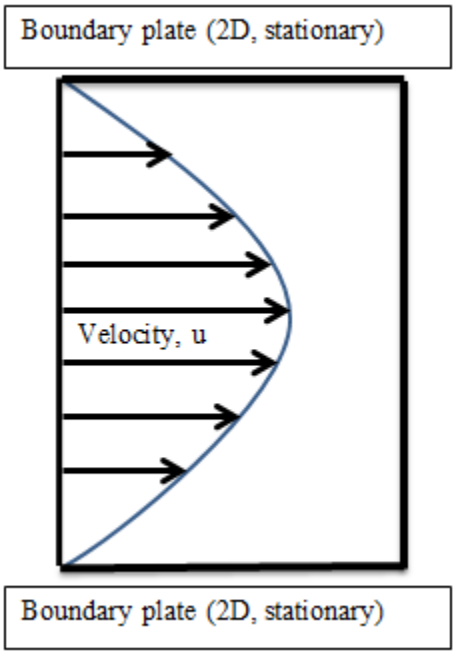

Figure 1. 14 Poiseule flow in the annulus of Couette slit between two stationary plates

The Poiseulle flow is important since it allows the control of the exposure time of the blood particles. This imposed Poiseulle flow through the flow path of the device allows the blood to be propelled at adjustable speeds axially through shearing gap, thus controlling the time spent by blood cells within the field of high shearing forces. The direction of this flow is perpendicular to direction of rotation of the inner cylinder. So we have a Poiseulle flow imposed on a Couette flow. It is also important to note that the velocity profile of a Poiseulle flow is parabolic as seen in the Figure 1. 14 which means that the particles at the center of the slit move at a higher speed than the particles near the walls. Thus not all the particles move at the same speed. This however

is not taken into consideration in this study and the exposure time calculated analytically assumes that all the blood particles are moving at the same speed.

Figure 1.15 shows the dimensions of the Mag-Lev shearing device where the thin gap allows for uniform shear stress on blood while the rest of the flow path having relaxed dimensions.

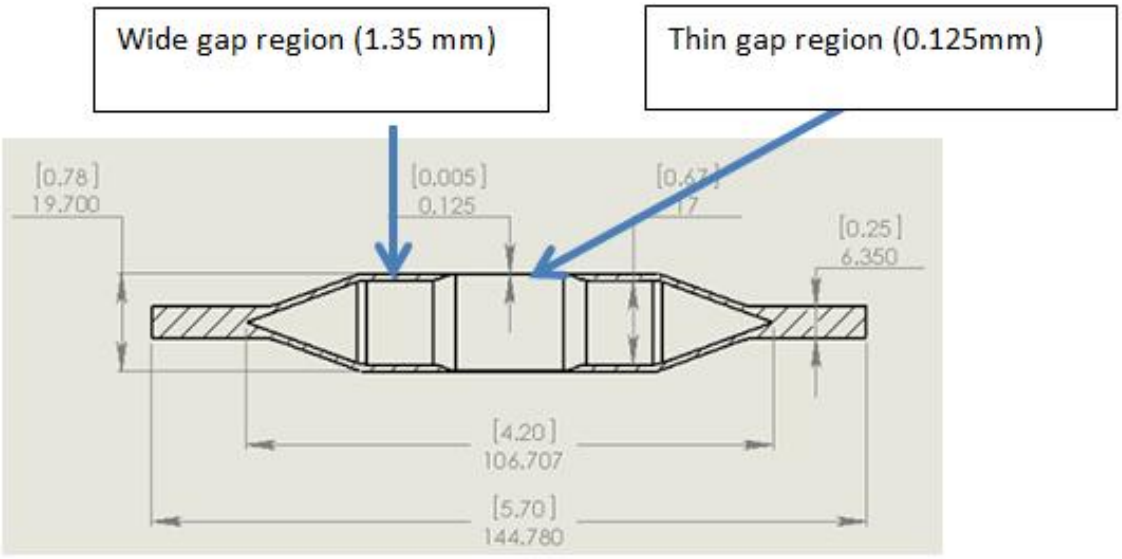

Figure 1.15 Details of the thin and the wide gap of design 1[2]

1.4.4 Components of the Mag-Lev shearing device

1. Magnetic system from LEV-VAD pump

2. outside housing

3. Impeller housing

4. Impeller rear

5. Bump

6. Inlet pipe with inner diameter of 0.25in/ 6.35mm

7. Outlet pipe with inner diameter of 0.25in / 6.35mm

The cross sectional view of the Mag-lev shearing device is shown in Figure 1.16

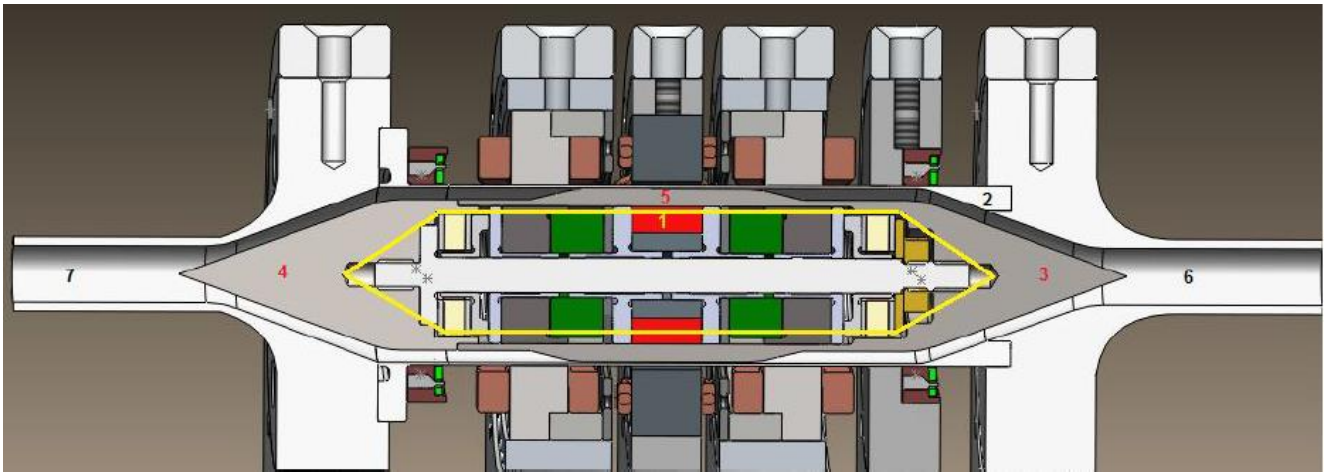

Figure 1.16 Cross-sectional view of full Mag-lev Shearing device 1 [2]

1.4.5 Drawbacks

The wide gap region is subjected to Taylor instability. The Taylor number in the wide gap region exceeds the critical Taylor number of 1708. The Table 1.2 below gives the Taylor numbers and the Reynolds numbers for this and the wide gap regions

Rotational speed [rpm]		3000	6000	9000
Rotational speed [rad/s]		314.2	628.3	942.5
Wider Gap	Re_rot	1081	2163	3244
	Ta_rot	185,764	743,058	1,67,1880
Thin Gap	Re_rot	114	229	343
	Ta_rot	168	674	1518

Table 1.2 Rotational Reynolds number in thin and wide gap regions for original geometry

The Taylor number and the Rotational Reynolds number used are given by the equations

Equation 1. 4 Rotational Taylors number [21]

$$Ta_{rot} = Re_{rot}^2 \left[\frac{1}{\eta} - 1\right]$$

Equation 1 .5 Rotational Reynolds number [21]

$$Re_{rot} = U_{rot}\, d/\nu$$

Where $d = R_2 - R_1$

$R_2 -$ Outer radius

$R_1 -$ Inner radius

$\eta = \frac{R_2}{R_1}$ radius ratio

ν = Kinematic viscosity

The formation of the Taylor vortices in the wide gap region is assumed to affect the programmed exposure time for which the blood can be exposed to shear stress. It is a question whether due to the massless particles used for hemolysis prediction using the Lagrangian method get seeded in the Taylor vortices increasing the exposure time and affecting the hemolysis data. As no particles escaped the outlet of the device, no hemolysis data could be recorded. Hence it could not be verified if the Taylor vortices affect eth exposure time for hemolysis data recorded. Thus it is essential to eliminate these vortices to allow for uniform exposure time and uniform shear stress application on blood.

1.4.6 Design Constraints

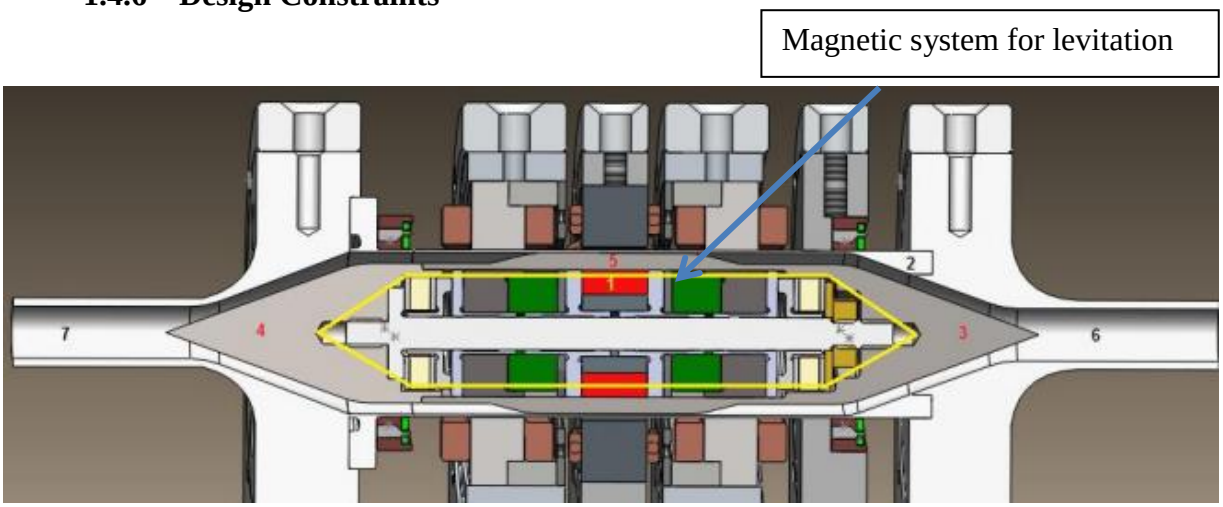

Figure 1. 17 Magnetic system used for design 1

Figure 1. 17 shows the magnetic system used for levitation in Mag-lev shearing device, design1. The length of the device shown in yellow line cannot be decreased then the current length because of the magnetic system. Hence the approach used is to reshape the flow path in the wide gap section upstream and downstream of the shear gap region.

1.4.7 CAD Model of Mag-lev shearing device

SolidWorks by Dassault Systems is used for the purpose of making the 3D Cad model. SolidWorks is a mechanical 3D CAD program. The pump geometry was modeled using Solid Works 2012. The initial design of the shearing device is shown in the Figure 1.18. The following section illustrates the changes made to the design following the flowchart shown earlier.

1.4.8 Progression of Design for the Mag-lev sharing device.

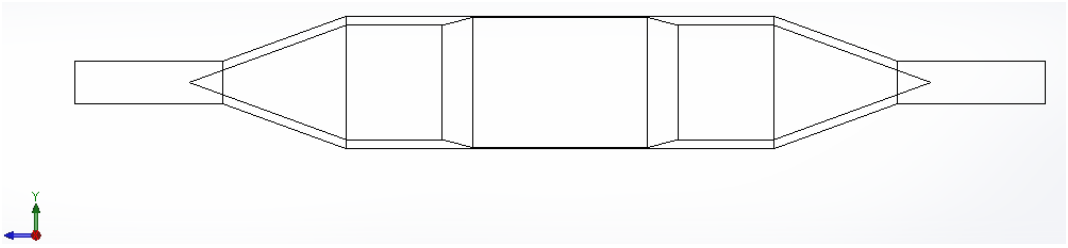

Figure 1.18 Design 1 of Mag-lev shearing device

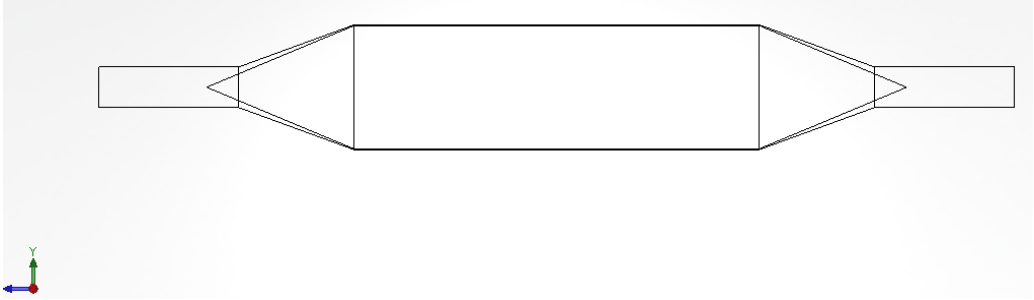

Figure 1.19 Design 2 of Mag-lev sheraring device

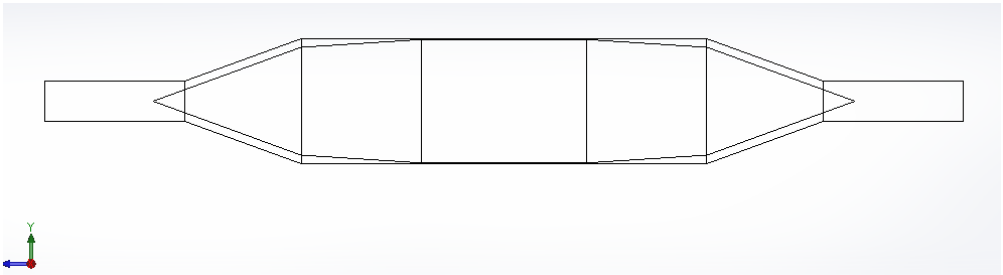

Figure 1.20 Design 3 of Mag-lev sheraring device

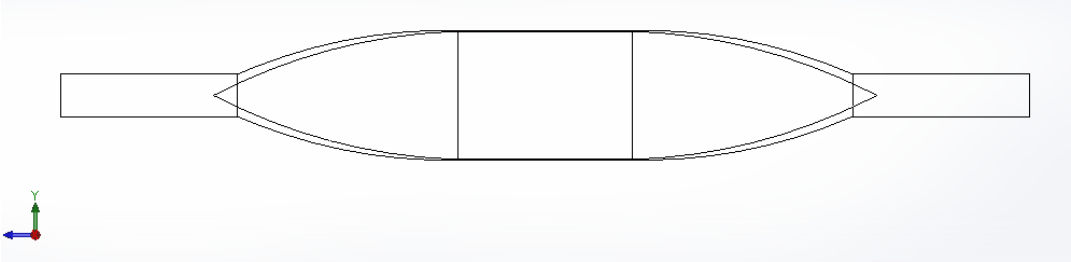

Figure 1.21 Design 4 of Mag-lev shearing device

Figures above show the different types of designs tested for the Mag-Lev shearing device with Figure 1.19 showing a uniform gap throughout the length of the device and Figure 1.20 showing a linearly increasing gap design. The Design 4 as shown in Figure 1.21 is the final design and is used for hemolysis analysis. Figure 1.22 shows the technical details of design 4 of the Mag-lev shearing device.

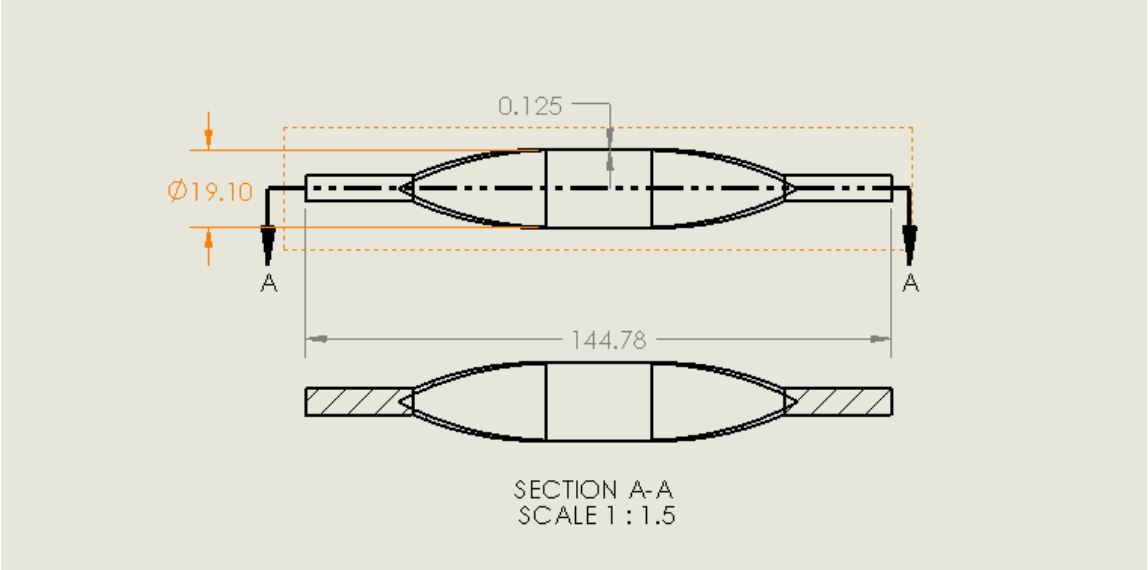

Figure 1.22 Design 4 of Mag-Lev Shearing device with the shearing gap of 0.125 mm

The design used for final numerical hemolysis is shown below in Figure 1.23

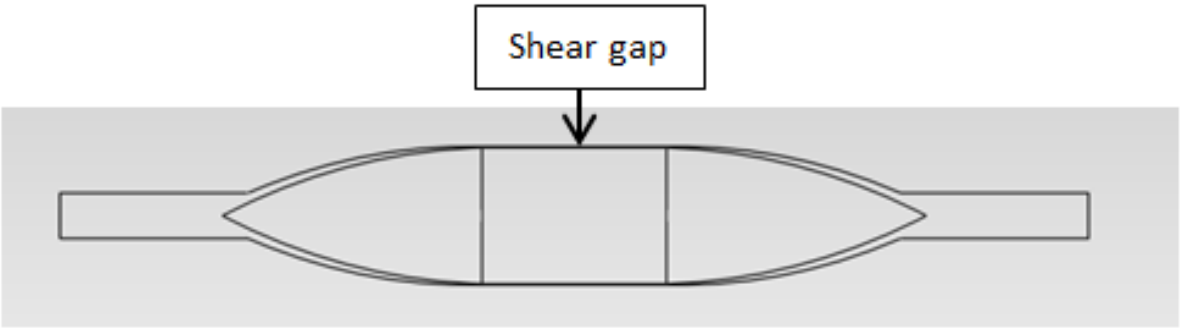

Figure 1.23 Cross section of the Mag-lev shearing device

1.5 CFD Simulation

1.5.1 Quick Background

CFD simulation is based on balance among realistic physical model, needed accuracy, computational resource, appropriate turbulent model and optimal mesh. It uses the Navier's Stokes equations to solve for flow parameters like velocity and pressure shown in equations below

Equation 1.6 Navier-Stokes equation with turbulent terms [2]

$$\frac{\partial u_i}{\partial t} + u_j \frac{\partial u_i}{\partial x_j} = -\frac{1}{\rho}\frac{\partial p}{\partial x_i} + \frac{\partial}{\partial x_i}\left(\frac{\mu}{\rho}\frac{\partial u_i}{\partial x_j}\right)$$

Equation 1.7 Continuity equation [2]

$$\frac{\partial u_i}{\partial x_i} = 0$$

1.5.2 CFD Analysis of the shearing device

CFD analysis consists of modeling the Mag-lev shearing device using Solid Works. It is then meshed in Gambit and simulated using Fluent. Once the flow solution is obtained the data is then post processed in Matlab for hemolysis analysis. The data exported from Fluent consists

velocity, strain rate, residence time along the pathlines that are released from the inlet of the shearing device.

1.5.3 Pathlines in Fluent

Pathlines are the lines traveled by neutrally buoyant particles in equilibrium with the fluid motion. Pathlines are an excellent tool for visualization of complex three-dimensional flows. These path lines were tracked and data for velocity and strain was analyzed and post processed in Matlab for hemolysis analysis.

1.6 Hemolysis Evaluation

Hemolysis evaluation will be based on two important parameters viz. exposure time and shear stress the data for which will be collected based on the release of pathlines or massless particles through the inlet of the shearing device. The details of pathlines and methods used for hemolysis evaluation are described below.

1.6.1 Methods for hemolysis evaluation

Method 1: Eulerian Approach

Eulerian approach has been used by Garon and Farinas in 2004 [22]. and Zhang in 2006 [23]. Fourgeau and Garon proposed a mathematical model to assess hemolysis by assuming the rate of hemolysis depended upon the instantaneous stress, exposure time, and damage history. A

hyperbolic advection equation was developed by the authors to assess a linearized damage function. The authors used Giersiepen power law constants Equation 1 1. The Eulerian approach determines hemolysis by using a single damage index parameter independent of exposure time The Eulerian approach determines hemolysis by using a single damage index parameter independent of exposure time.

Hemolysis Power law model has the following general form.

Equation 1.8 Linearized blood damage model

$$D = \ Ct^{\alpha}\tau^{\beta}$$

This blood damage model is non-linear with respect to time. Garon and Farinas introduced linear damage DI [22]

Equation 1.9 Linearized blood damage model

$$\boldsymbol{D_I = \ D^{1/\alpha} = C^{1/\alpha} D\ \tau^{\beta/\alpha}\ t}$$

The blood damage can be formulated as a partial differential equation discretized on Navier-Stokes computational cells. Time derivative along a streamline of the linear blood damage is constant and given by source term, I

Equation 1.10 Damage source term

$$\boldsymbol{I = \frac{D}{Dt}[D_I] = C^{1/\alpha} D\, \tau^{\beta/\alpha}}$$

The authors made following three assumptions:

1. The equation of blood damage source term applies outside the interval of definition of Giersiepen (1< t_{exp}<700ms and 0< τ <255 Pa).
2. The equation of blood damage source term applies to a material volume along a Streamline and describes the blood damage evolution inside this material volume.
3. It applies to any material volume.

A time independent average linear damage index DI with flow rate (Q) was obtained as

Equation 1.11 Average linear damage index

$$\boldsymbol{\overline{D_I} = \frac{1}{Q}\int I dV}$$

Finally, the average damage was then obtained from average linear damage index by the following equation,

Equation 1.12 Time independent average damage index

$$\boldsymbol{\overline{D} = \overline{D_I}^{\alpha}}$$

Method 2: Lagrangian approach

The Lagrangian approach tracks and treats those particles in a fluid flow. This method is used to sum up the hemoglobin leakage along streamlines. Hemolysis rate is integrated along each path line to calculate blood damage for individual red blood cells. It is assumed that the corpuscles in the blood do not deviate from the flow path of the plasma [9]

In Method 4, the rate of hemolysis is integrated along the path lines in a flow with an instantaneous scalar measure of stress and exposure time to compute accumulated hemolysis. By taking the average over a sufficiently high number of path lines, it is possible to calculate the hemoglobin release in the blood pump. This analysis provides a statistical estimate of damage to cells flowing through the pump.

Lagrangian method was previously used by Apel (2001) [9], Chan (2002) [24]Yano (2003) [62], Song (2004) [[25]and Arora (2006) [26]

Apel (2001) used Lagrangian method by tracking 1000 particles inside the Impeller micro axial pump in order to determine hemolysis. His study revealed that average shear stress inside the axial blood pump was 200 Pa with an average exposure time approximately 5 msec. Highest shear stress was found to be 1000 Pa although the exposure time was significantly short [9]

Chan (2002) compared five different blade designs for centrifugal pump while demonstrating particle tracking method by releasing 100 particles from pump inlet. He concluded that the more particles will give more accurate shear stress and exposure time results [27]

Yano (2003) used the Giersiepen power law relationship to evaluate the hemolysis occurring inside a rotary LVAD. The scalar stress values were computed at each computational node and blood element shear stress histories were determined along 937 streamlines released at the inlet of the domain. Finally, equation along with the data from the particle traces related the shear stress and exposure time to an estimate of level of hemolysis [28]

Song (2004) applied a Lagrangian approach to assess the stress distribution and related exposure time inside centrifugal blood pump by tracking 388 particles. The accumulation of shear and exposure time is integrated along the pathlines to evaluate the levels of blood damage index or blood trauma. The mean residence time found to be 0.34 msec with mean blood damage index of 0.21%. Damage indices were reasonably correlated with hemolysis levels of clinically in vitro tested pumps [25], Arora (2006) had traced 100 uniformly distributed particles over the inlet section for following them up to 1s or until they exit the device. He found 78% of the particles reach the outflow, while the rest either remain in the pump or hit the walls due to approximate errors. By using equation of NIH values per single pass though the pump [29].

To get an accurate result using Lagrangian method is to trace a sufficient number of particles inside the pump to represent an accurate shear stress and exposure time values inside the pump. This calculation requires extensive amount of computational resources. Sometimes particles can be trapped inside one region for a long time and this is called recirculation zone. Hemolysis information from these trapped particles is not reliable because the exposure time is extremely

long. It is also possible that the particles that get trapped in eth recirculation zone never really exit the device and the ones that exit the device never enter the recirculation zone.

Lagrangian Analysis

For Lagrangian analysis the following equation will be used

$$\mathrm{HI} = \sum_{Inlet}^{Outlet} C\ \Delta t_{exp}^{\alpha}\ \ \tau^{\beta}$$

Equation 1.13 Equation for Lagrangioan analysis

The Power Law Equation constants used for hemolysis calculations are summarized in Table 1.3

Table 1.3 Power Law Equation Constants and their Covering Ranges

Range					
Model	Shear Stress(Pa)	Exposure Time (s)	C	α	β
GW	<255	<700	3.62E–05	0.785	2.416
HO	<700	<700	1.80E-06	0.765	1.991
TZ	50-322	<1500	1.23E-05	0.6606	1.9918

GW, Giersiepen *et al.* constants; HO, Heuser *et al,* constants; TZ, Zhang *et al.* constants;
C α β constants of the power law equation
Experimental set up used to reach each of the constants viz. GW, HO and TZ where,

GW, Giersiepen *et al.* constants; HO, Heuser *et al*, constants; TZ, Zhang *et al.* constants

Figure 1.24 to Figure 1.26 show the experimental set up for the above mentioned constants. All the experimental set ups are Couette type settings with an internal rotating cylinder.

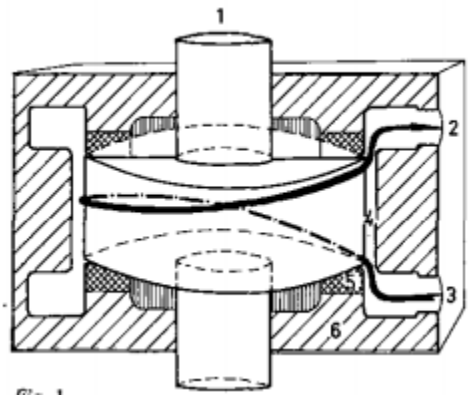

Figure 1.24 Experimental set up used by Wurzinger *et.al.* 1. Driving shaft; 2. Outlet; 3. Inlet; 4. Couette slit between stationary outer and rotating inner cylinder[30]

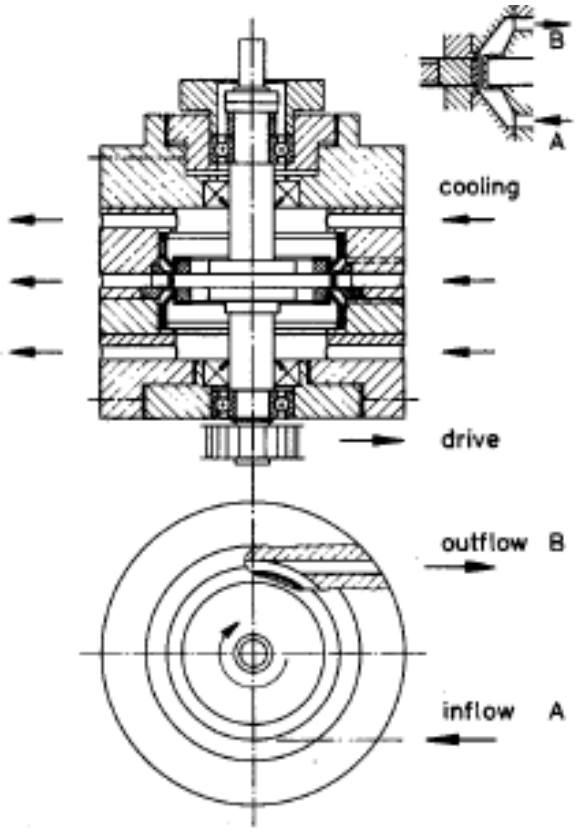

Figure 1.25 Experimental set upused by Heuser Opitz and Wurzinger for HO constants and GW constants[31]

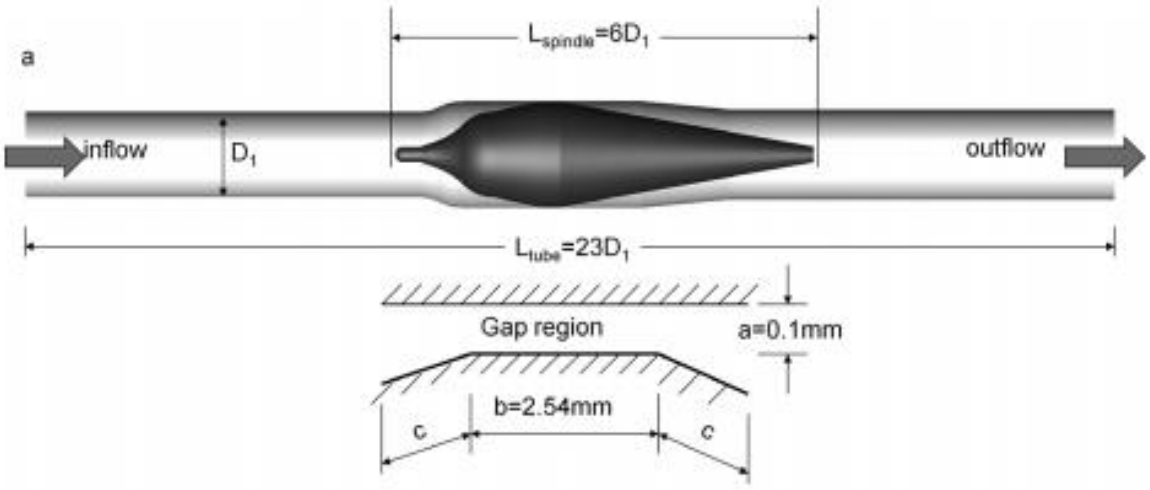

Figure 1.26 Experimental steup for Taskin.*et.al* for TZ constants[32]

Table 1.4 shows the shear stress and exposure time for different constants and this work.

	Sheas Stress (Pa)		Exposure time(msec)	
Model	Min	Max	Min	Max
HO	40	700	3	600
GW	57	255	7	700
TZ	50	320	39	1480
This work	60	230	58	230

Table 1.4 Shear stress and Exposure time ranges considered in experiments for each constant

These values are compared in Figure 1.27 and Figure 1.28 to understand how these values differ with respect to each other.

1.7 Data Comparison Graphs for all Models used

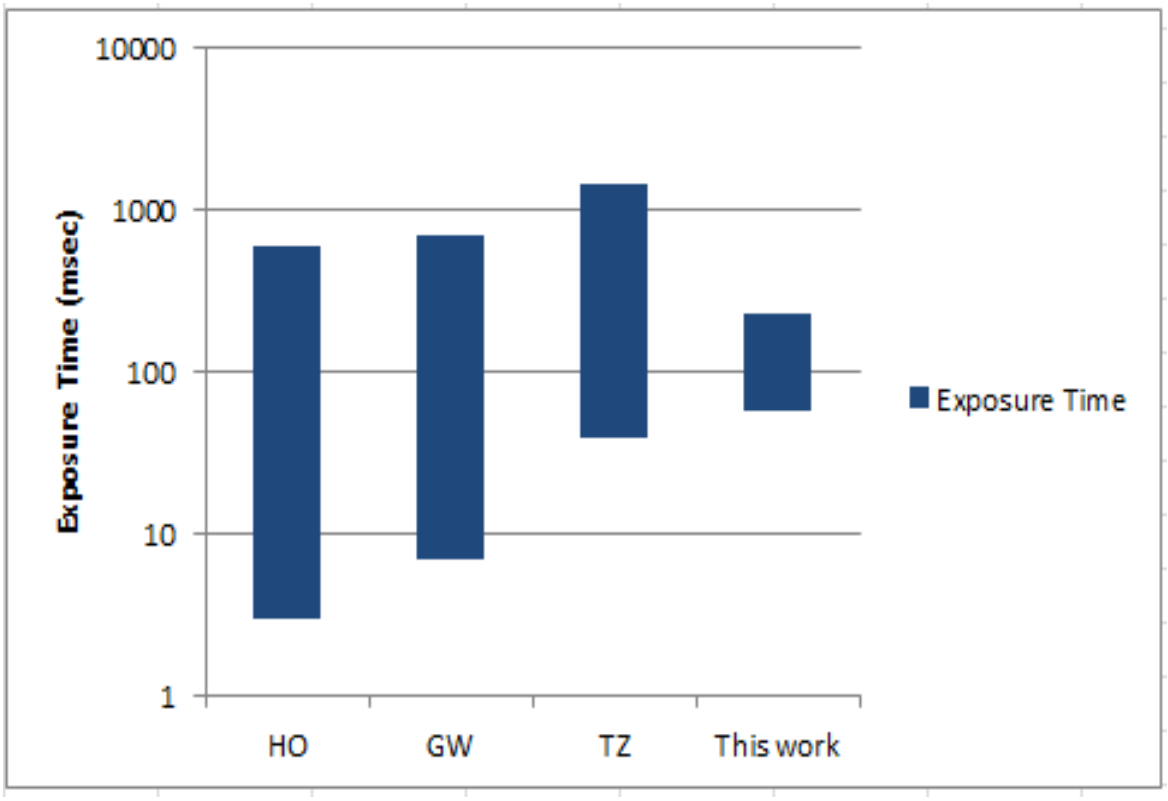

Figure 1.27 Exposure time comparison for all Models used and this work

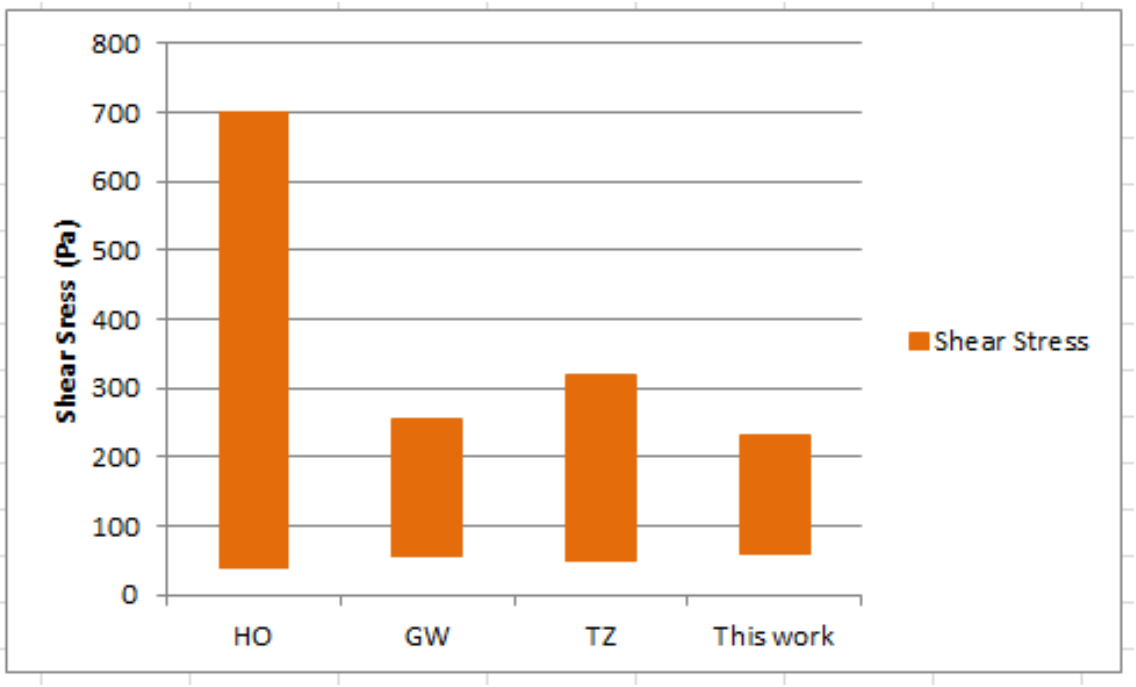

Figure 1.28 Shear Stress comparison for all Models used and this work

Variation in the value of Exposure time and Shear stress for GW, HO, TZ constants.

Giersiepen *et al.* constants; HO, Heuser *et al,* constants; TZ, Zhang *et al.* constants;

1.8 Target design parameters

The design parameters are selected as follows.

1. Shear stress generated by the new design should be greater than 150Pa since beyond this limit the cell damage is exclusively due to shear stress
2. The exposure times are varied between 58 msec $< t_{exp} <$230 msec as peer the flow rates of 50ml, 100ml, 150m/min, 200ml/min

Chapter 2

Methods

In order to properly analyze hemolysis, a given geometry is modeled using three-dimensional (3D) computer aided design (CAD) software. The fluid dynamics inside the pump can only be solved by using CFD due to the complex geometry of the pump. The primary software's that were utilized for CFD analysis are Solid Works, Gambit and Fluent.

Note on Simplification of Geometry.

The simplification of geometry by having a 2D axisymmetric geometry was thought of. However since the analysis involved the tracking of pathlines for the Lagrangian analysis a 3D model seemed appropriate. The simulation time for this 3D geometry for the finest mesh is not more than 15-20 minutes. One of the advantages of using a 2D axisymmetric geometry could be that the geometry could be meshed even finer with regards to reading 5 million cells limitation by Fluent.

2.1 Meshing – Gambit

2.1.1 Simple Geometry Meshing

Predicting Taylor vortices

In order to predict vortices correctly the numerical code was tested for a simple geometry with a gap size as that of the wide gap region in the Design 1 of the Mag-Lev shearing device. The geometry modeled in fluent is shown in the Figure 2.1. A uniform inlet velocity condition was given at the inlet and constant pressure of 200 KPa was set at the outlet. In order to predict the flow near the walls four rows of boundary layers were specified at the inlet and the outlet. Interval size from 0.3mm to 0.8mm was tested to find out if the meshing model could predict Taylor vortices. A total of 8 boundary layers were used between the inner rotating and outer stationary cylinder. Four boundary layers attached to the inner cylinder while four to the outer. No mesh refinement was conducted for these boundary layers and all the design's including simple geometry had only 8 boundary layers. The decreasing interval size increased the number of cells across the length of the whole design. The interval size used and its details have been discussed in mesh refinement section after this section. The gap for this simple geometry resembling two concentric cylinders was 1.35 mm for which the Taylor vortices should appear at 287 rpm when the Taylor number exceeds the critical Taylor number (Ta_{cr}) of 1708. The code predicted the existence of Taylor vortices for all the element sizes. These mesh cases were

further solved for mesh Independence using Fluent. Inc. and the same settings were used for analysis of following designs.

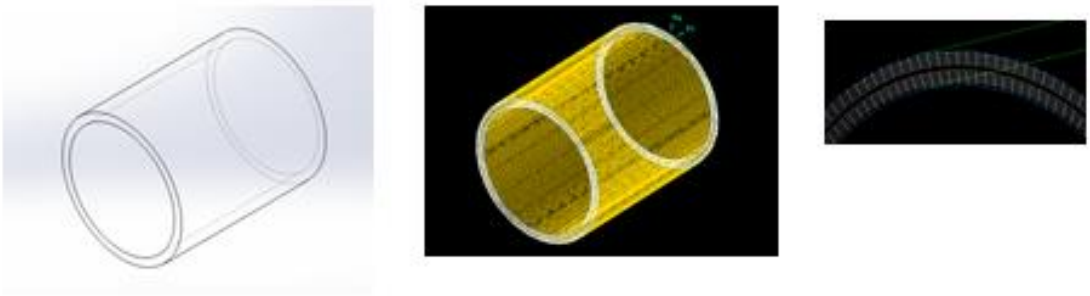

Figure 2.1 Simple concentric geometry used for testing the Numerical code used for Taylor vortex prediction showing the solid model in Solid works along with the meshing in Gambit and the Boundary layers used for at the inlet and the outlet.

2.1.2 Interval size used for Mesh Refinement

This is used to control the node spacing while meshing the faces and volume of all the geometries meshed and allows you to specify the number of intervals on the edge that need to be generated. There are three different ways in which you can control this in Gambit.

1. Interval count
2. Interval size
3. Shortest Edge (%)

We are going to used interval size in this analysis. When you select the interval size option, you must input an interval length. Gambit uses the interval length to determine the total number of intervals on the edge according to the following equation $n = \frac{L}{d}$ where n is number of intervals on the edge, L is the edge length and d is the interval size (user input).

The use of Interval size is explained in the following figures. The mesh setting for the Design 4 is used for this purpose. This is however common for all the other designs including the simple geometry mesh refinement.

The interval size (d) is user input. The edge or the face length (L) is then divided by the interval size (d) to get the value of (n). We then have n divisions on eth edge or the face considered for the operation.

The mesh section of Design 4 used for the analysis is shown in Figure 2.2.

2.1.3 Interval size Explanation

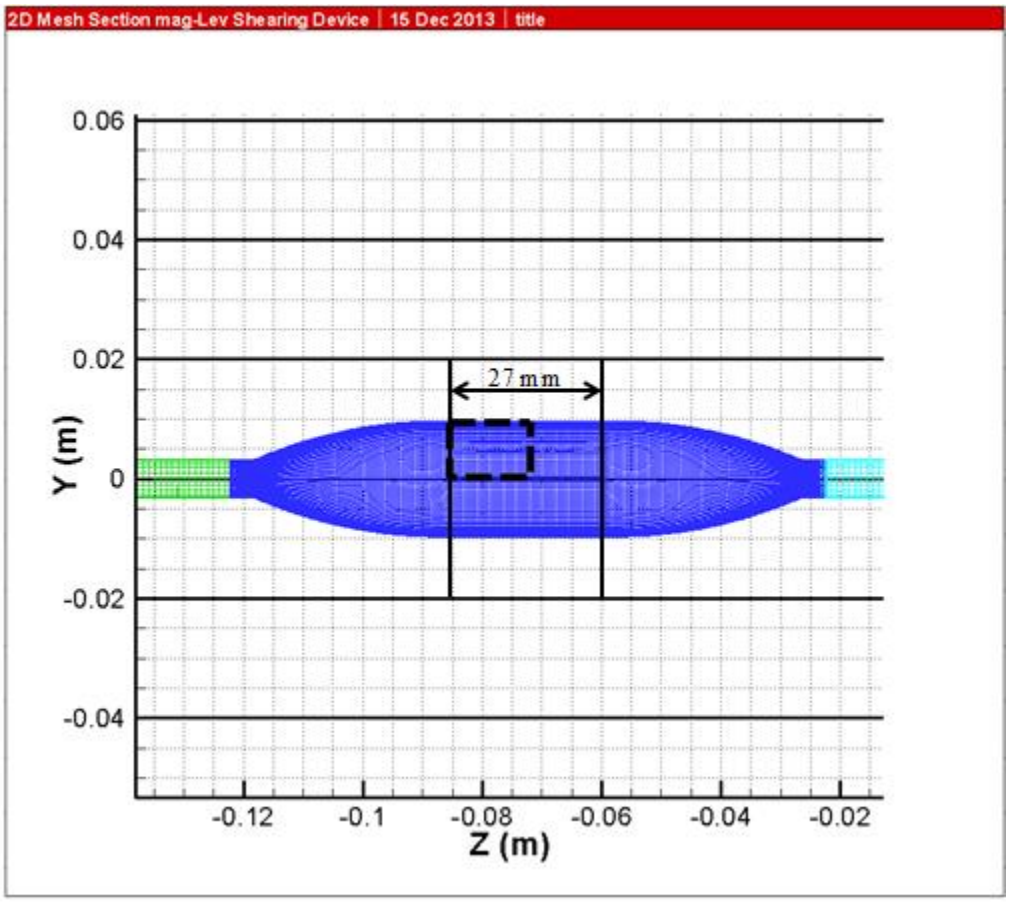

Figure 2.2 2D mesh section showing the mesh section used to describe the use of interval size.

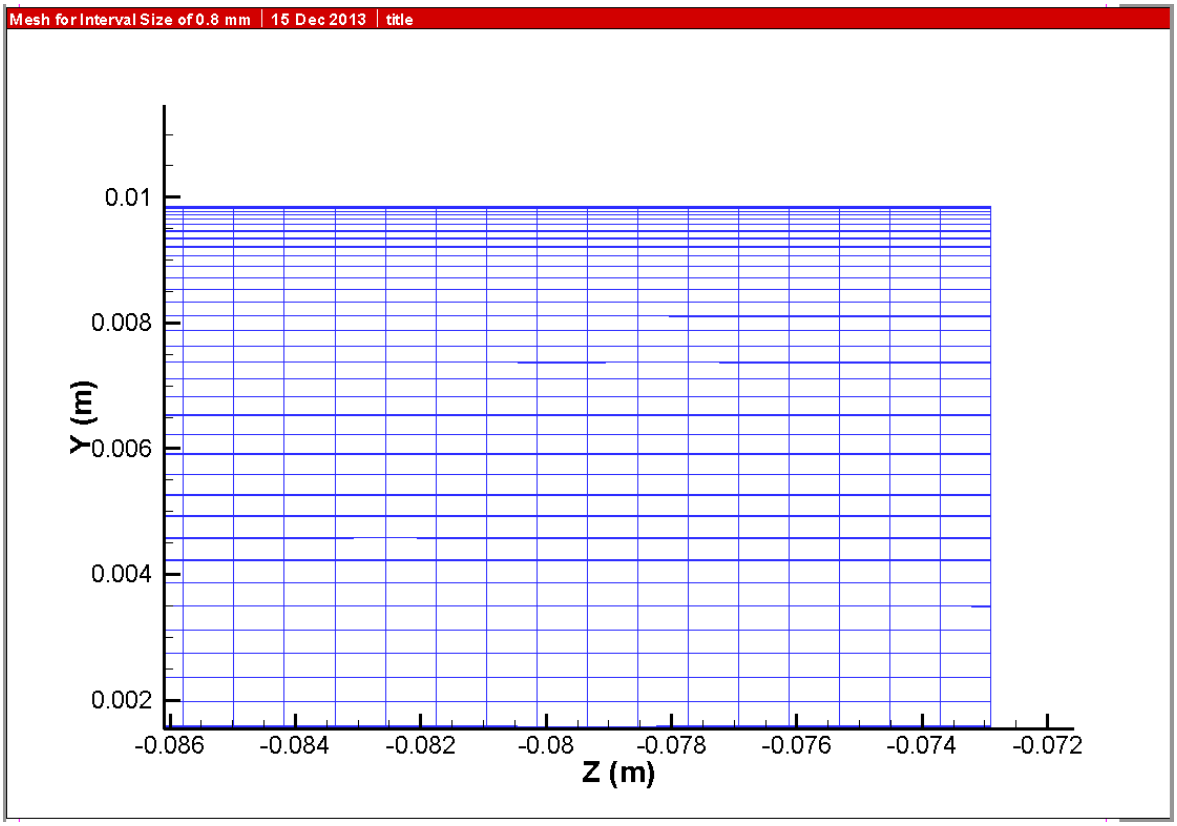

Figure 2.3 ¼ of the cross section of the mesh in the thin gap region shown for an interval size of 0.8 mm.

Figure 2.3 shows the mesh details for an interval size of 0.8 mm. We can see that the total number of columns is equal to 16. Also, 0.8mm * 16 rows = 12.8 mm which is approximately 13 mm which isapprox. length of the ¼ section of the 27 mm long thin gap section considered. For an onterval size of 0.8 mm we have 32 cell columns in the thing gap region which is 27 mm long. As the interval size decreases the number of rows increases which can be seen in the figures for interval size 0.6 mm(42 cell columns), 0.5 mm(50 cell columns) and 0.4 mm (64 cell columns).

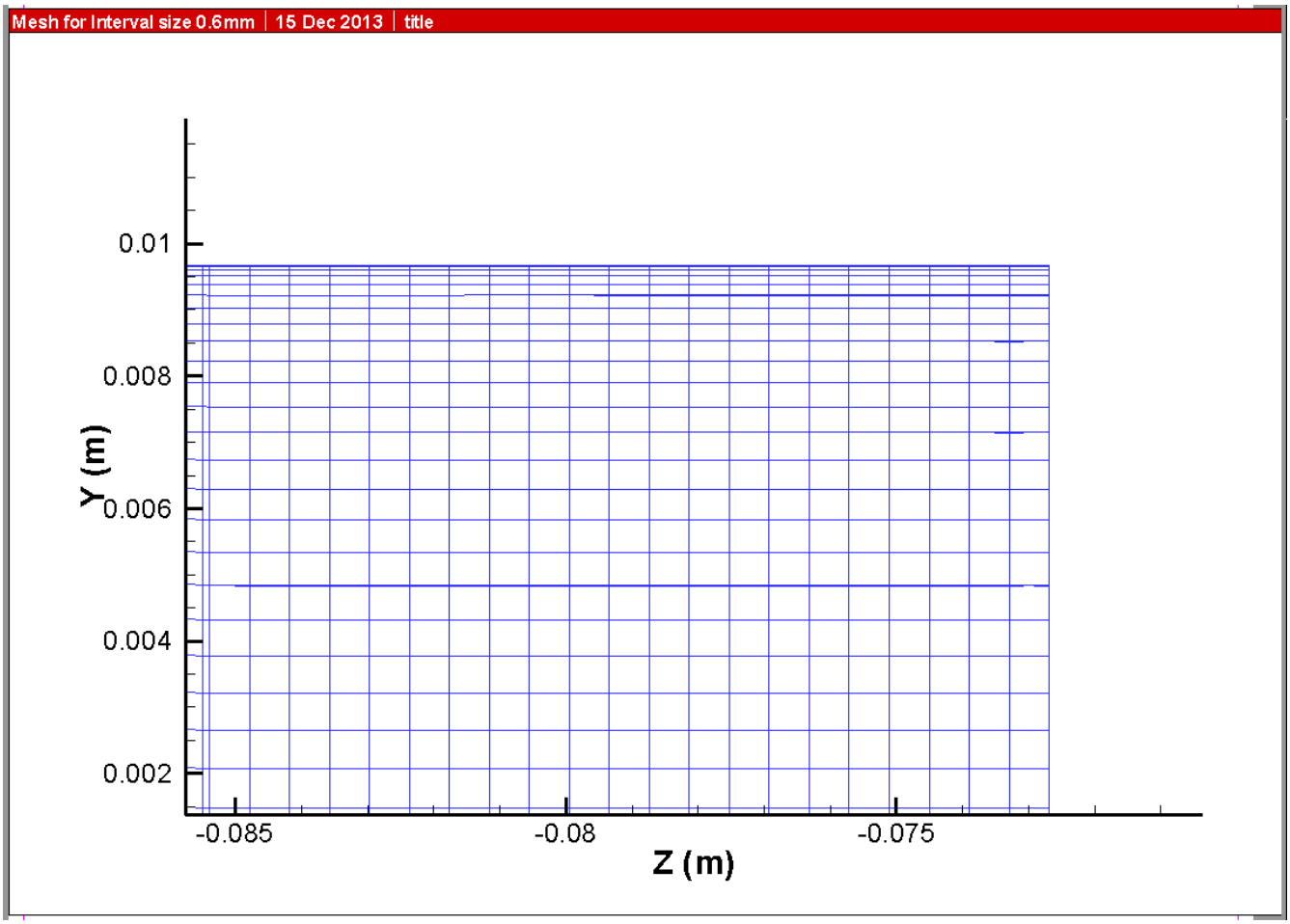

Figure 2.4 ¼ of the cross section of the mesh in the thin gap region shown for an interval size of 0.6 mm. Number of cell rows equal 21. 0.6 mm and 21 cell rows give 12.6 mm which is approximately equal to 13 mm.

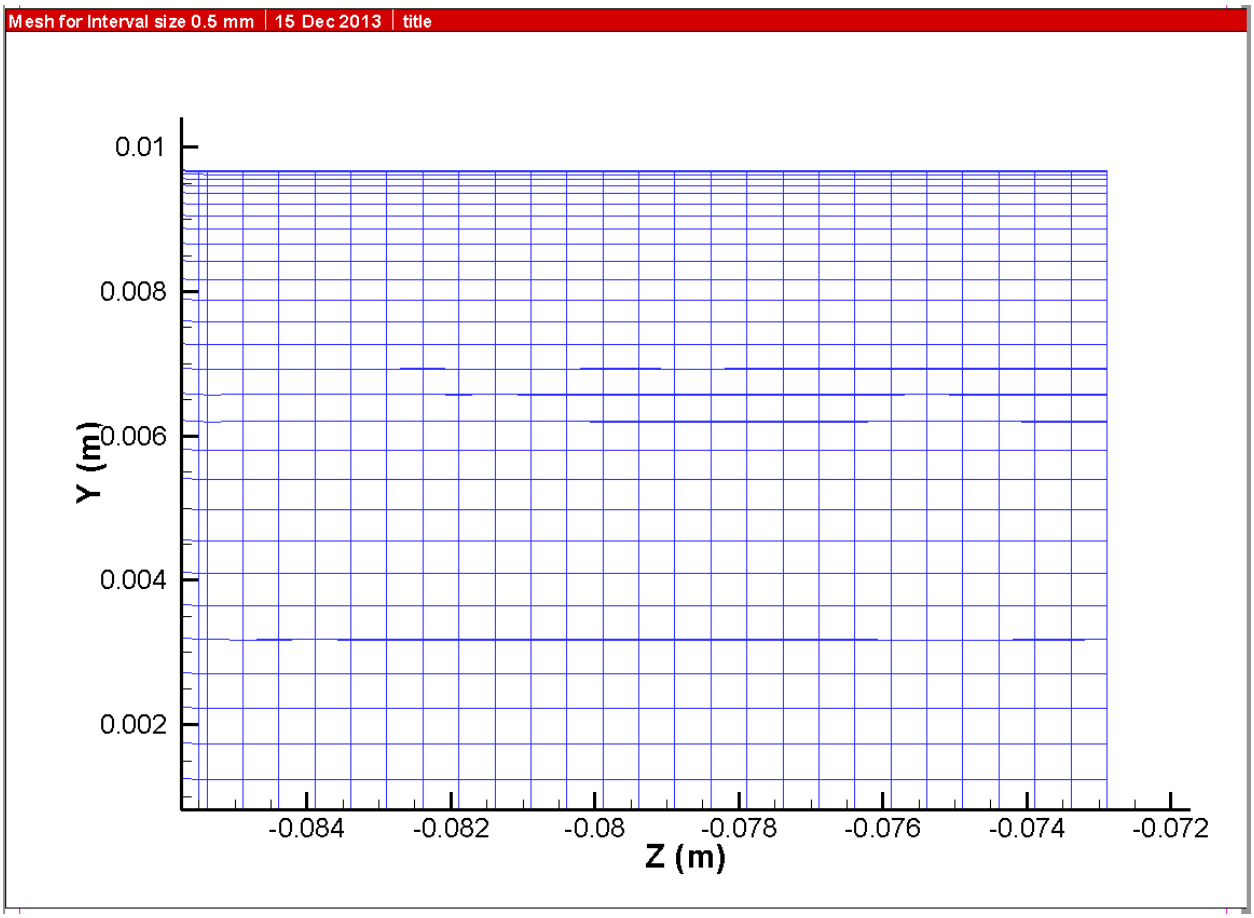

Figure 2.5 ¼ of the cross section of the mesh in the thin gap region shown for an interval size of 0.5 mm. The number of cells is 25. The number of cells when divided by the interval size 0.5 mm we get the value of 12.5 mm which is approximately equal to 13mm which is half the length of the length of the thin gap region of 27 mm.

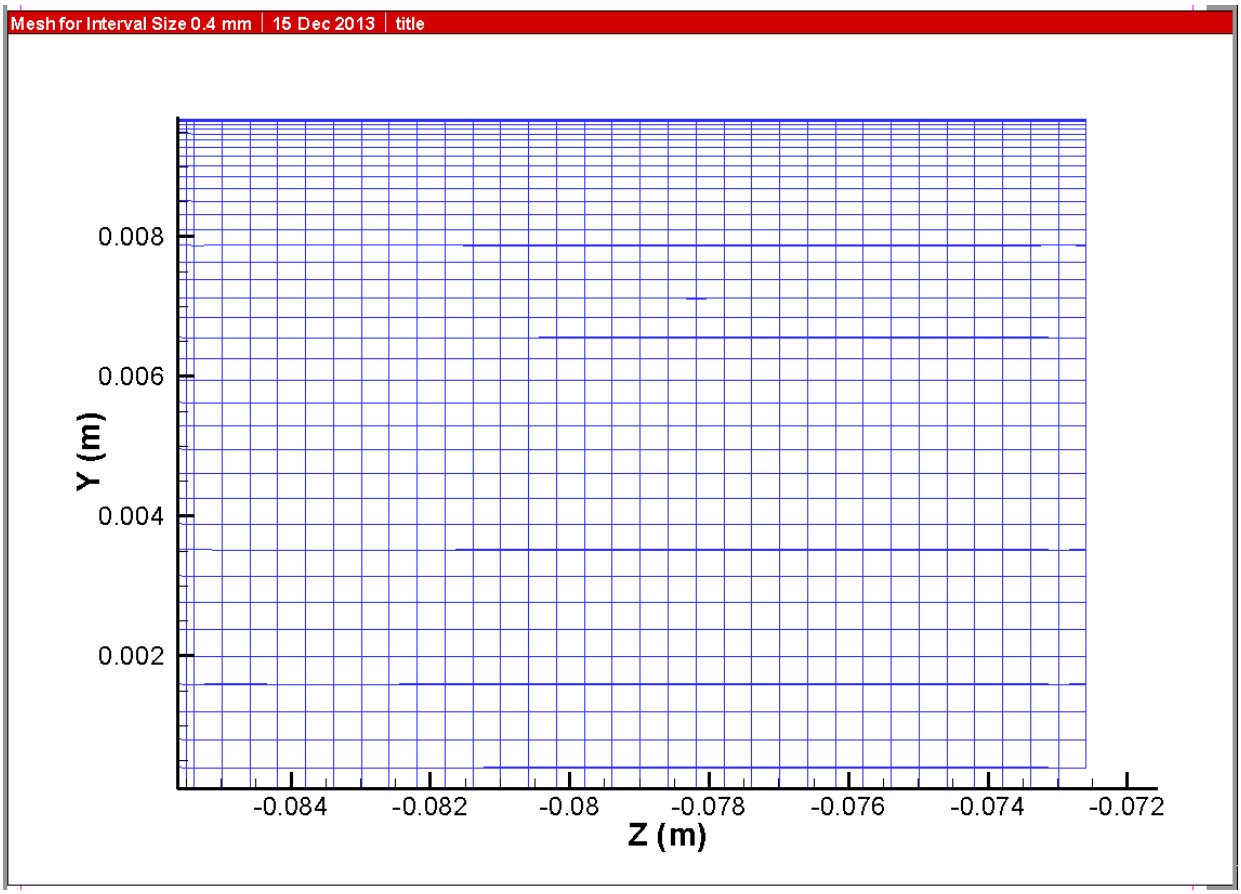

Figure 2.6 ¼ of the cross section of the mesh in the thin gap region shown for an interval size of 0.4 mm. The number of cells is 32. The number of cells when divided by the interval size 0.4 mm we get the value of 12.8mm which is approximately equal to 13mm which is half the length of the length of the thin gap region of 27 mm.

Figure 2.4, Figure 2.5, Figure 2.6 show how each cells length is decreased as the interval size goes on decreasing.

2.1.4 Mesh refinement

Simple Geometry

The described mesh refinement was used for the analysis of a simple concentric geometry and the Table 2.1 givens the details. The Taylor vortex detection results are shown in. Figure 2.7. Figure 2.8, Figure 2.9 show the solid model and geometry details of the simple concentric geometry considered for initial anaysis.

Table 2.1 Summary of the Mesh refinement for the simple geometry and detection of vortices

Element Size(mm)	Number of Boundary layers inside gap	Mesh #	Detected vortices
0.3	8	5	Yes
0.4	8	4	Yes
0.5	8	3	Yes
0.6	8	2	Yes
0.8	8	1	Yes

RPM	Axial Velocity Contour Plots
1000	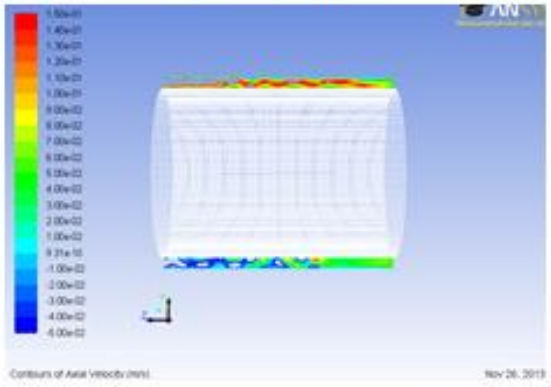
2000	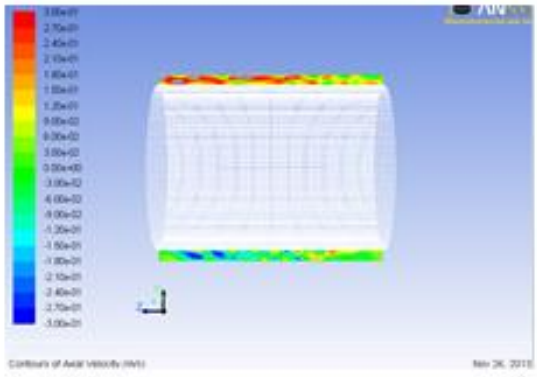
6000	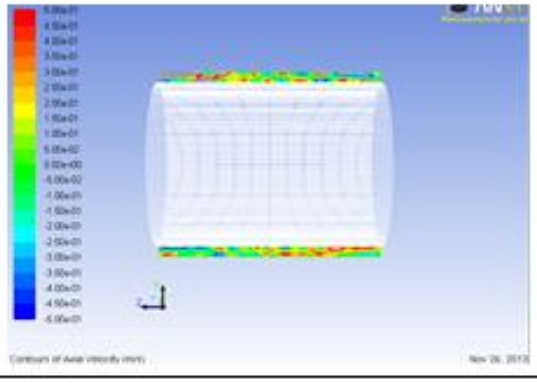

Figure 2.7Axial velocity plots showing Taylor vortices at higher rom for the simple geometry

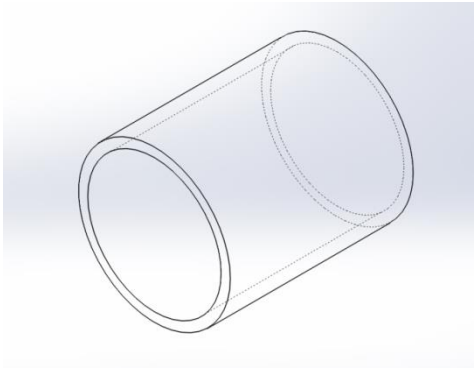

Figure 2.9 Solid model of simple geometry used

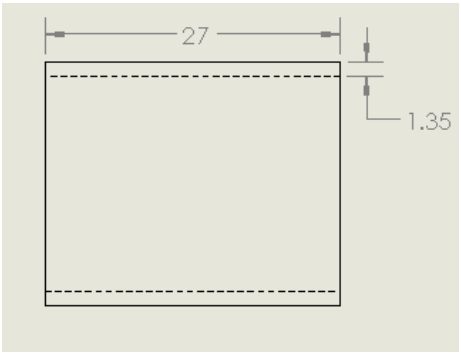

Figure 2.8 Technical details for simple geometry

The theoretical value of rpm at which the Taylor number of 1708 is exceeded is 287 pm for a gap size of 1.35 mm. The simulation code shows the formation of Taylor vortices at 245 rpm. There is 85% accuracy. The same mesh setting will be used for all the other geometries for analysis. A transect was created for plot x-y plots. Table 2.2 gives the details.

Table 2.2 Summary of the transect

Transect Summary	
x0=0	x1=0
y0= 22.22 mm	y1=0 mm
z0= 1.205 mm	z1= 1.205 mm

The strain rate and velocity distributions on transcet1 were shown in Figure 2.10 to Figure 2.12. Strain rate unit is inverse second [s^{-1}] while velocity is meter per second [m/s]. It was observed that the variation in the strain rate decreased from mesh D to mesh E. The mesh D was used as a case for testing the prediction of Taylor vortices. Also, the settings of mesh D were selected for flow analysis of Mag-lev shearing device designs.

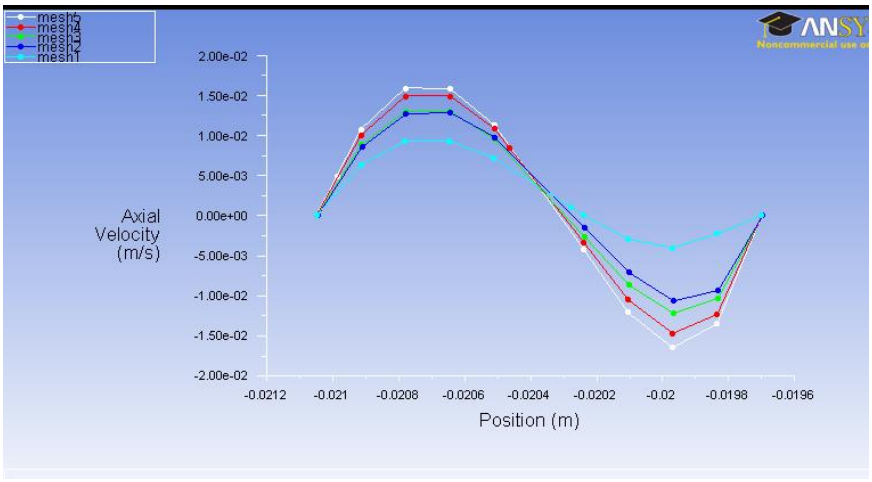

Figure 2.10 Axial Velocity[m/s] on Transect

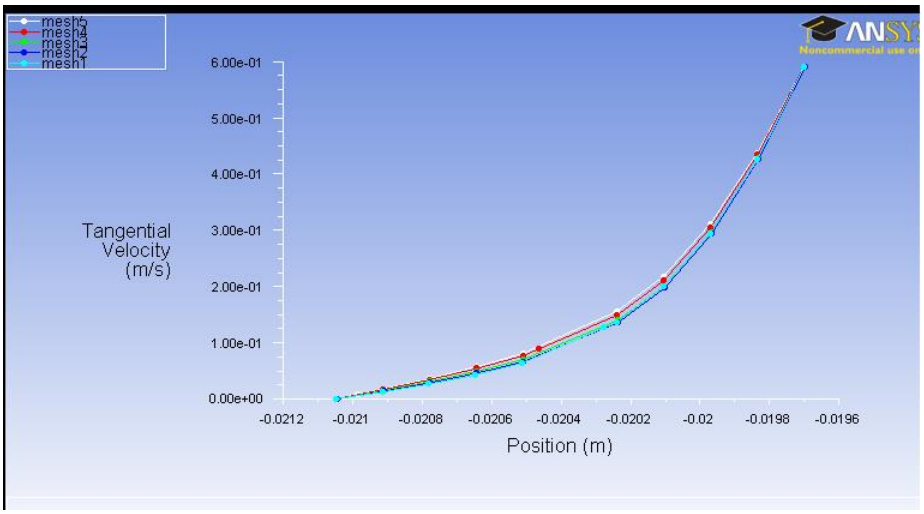

Figure 2.11 Tangential Velocity[m/s]

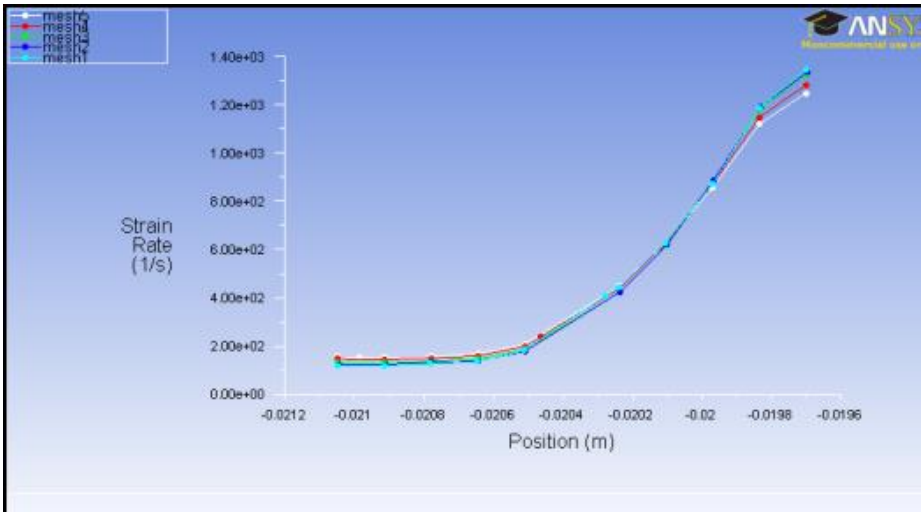

Figure 2.12 Strain rate [1/s] on Transect

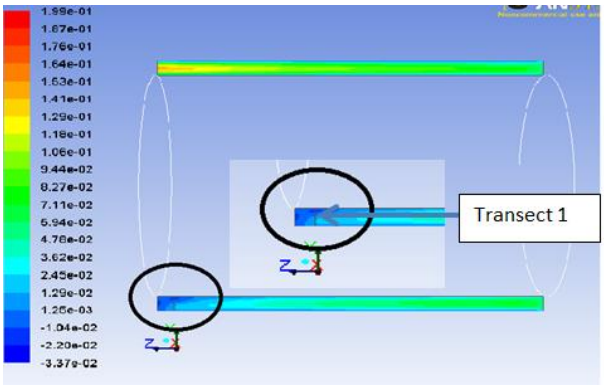

Figure 2.14 Axial velocity contour plot

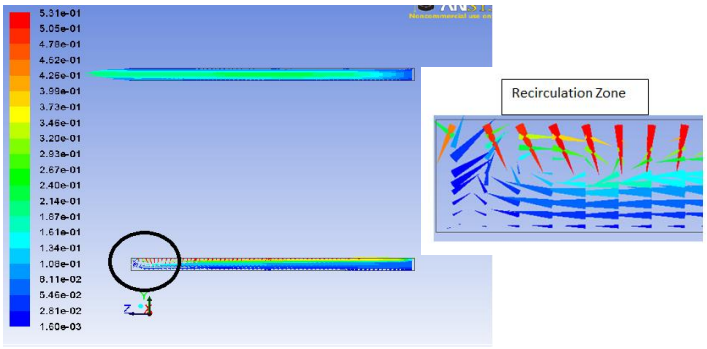

Figure 2.13 Axial velocity vector plot

Figure 2.13 and Figure 2.14 shows details of the axial velocity for the simple geometry. The vortex formation was detected at rpm of 245 pm. The actual Taylor vortex s formed at 287 rpm (theoretical) which is also shown in the zoomed section in Figure 2.14.

The theoretical value of critical Taylor number is 1709. Ideally the mesh should have detected the Taylor vortices at 287 rpm when the Taylor critical number of 1708 is exceeded. However the mesh settings can best detect Taylor number at 245 rpm which is a 14.63 % error. Table 2.3 shows that the vortices were first detected by mesh D first at a rotational speed of 245 rpm and when the Taylor number (1708) is exceeded at 287 rpm. Figure 2.15 shows the summary for x-y plot for three different rpm.

RPM	Axial Velocity Contour Plots	Axial Velocity Profile	Taylor Number
230		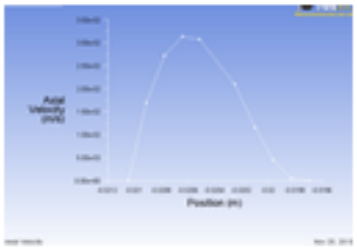	1098
245	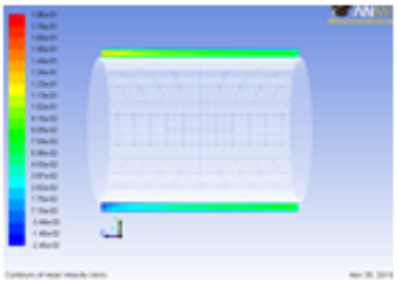	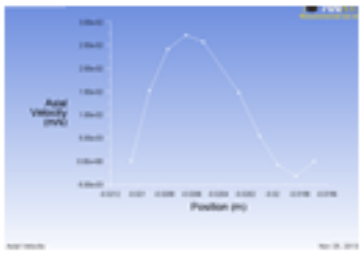	1246.147
287	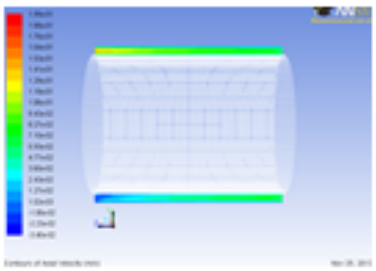	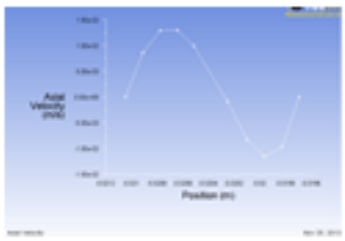	1709

Figure 2.15 Detection of Taylor vortices at 245 rpm by simualtion and the actual formation of vortices at 287 rpm.

Table 2.3 Simulation RPM at which the Taylor number is detected and at which it exceeds $Ta_{cr} = 1708$

Taylor number calculation(Wide Gap)			
N	230	245	287
Re rot	4.18E+01	1.01E+02	1.20E+02
Ta rot	1098	1246.147	1709.167038

2.1.5 Mag-lev- Design 4- Meshing

The wide gap upstream and downstream of the shear/thin gap for Mag Lev Shearing Device Design 1, was susceptible to Taylor vortices. The existence of the Taylor vortices was confirmed by the axial velocity contour plots and axial velocity vector plots, where we had positive and negative axial velocities visible indicating that the existence of recirculation zones, in the wide gap region. The blood particles released did not escape the outlet and stopped near the wide gap as will be shown in further Chapter ahead. In order to track the particles till the outlet, an intuitive attempt was made to redesign the upstream and the downstream region of the shear gap and the effect on the tracking of massless particles was observed. It was found that that with the design modification mass less particles could be tracked from the inlet to the outlet. The ensuring sections discuss the methods and the calculations performed to predict the blood damage HI (%) in the modified design.

The computational model consists of an impeller and an outside housing similar to the Mag-Lev shearing device. The smallest gap between the housing and the impeller is 0.125mm. A cross section of the device is shown in Figure 2.16

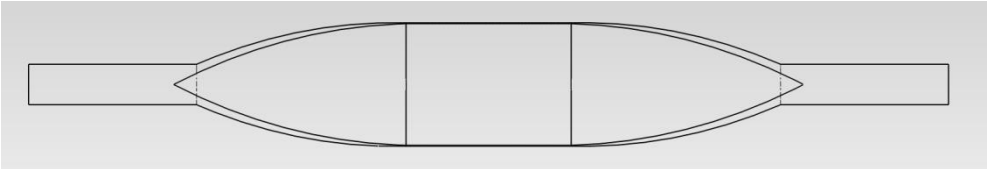

Figure 2.16 Cross section of the Design 3 showing the modified gap region.

Meshing:

Hexahedral cells were used for the inlet and the outlet, gap and curved gap region. The rest of the geometry was meshed with tetrahedral cells with uniform interval size (0.4). The overall size of the elements was 466702. Figure 2.17, Figure 2.18 shows the mesh structure for the gap.

Figure 2.17 Mesh structure gap thickness

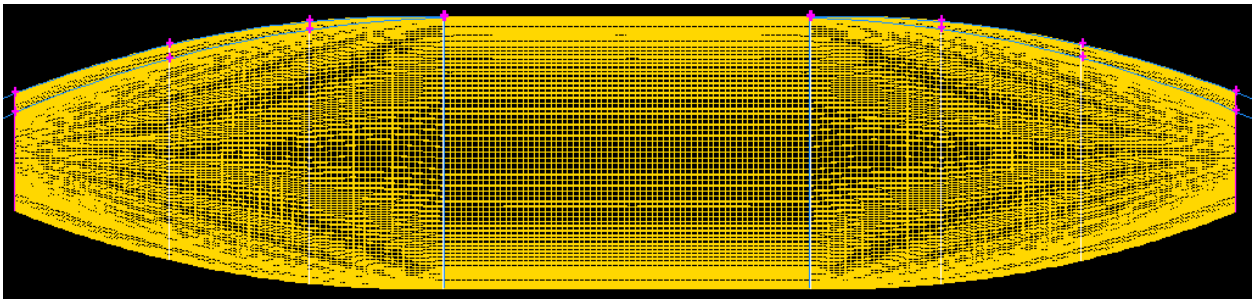

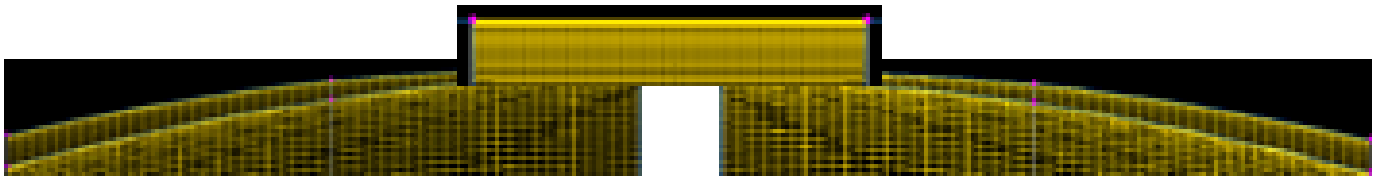

Figure 2.18 gap length with the pre and post gap region

For meshing the Mag-Lev shearing device was divided into 15 volumes .All the volumes except for volumes number 2 and 14 were meshed using the Hex/Cooper mesh. TGrid was used for volumes 2 and 14. The overall mesh can be seen in Figure 2.19, Figure 2.20 shows the details of the mesh used.

Table 2.4, summarizes the mesh type and the number of elements for each volume. Volume 2 and volume 14 were meshed with an interval size of 1 since any interval size lesser than this would result in critical error in the grid when the mesh was read in Fluent. The reason for the grid failure was not investigated in this work.

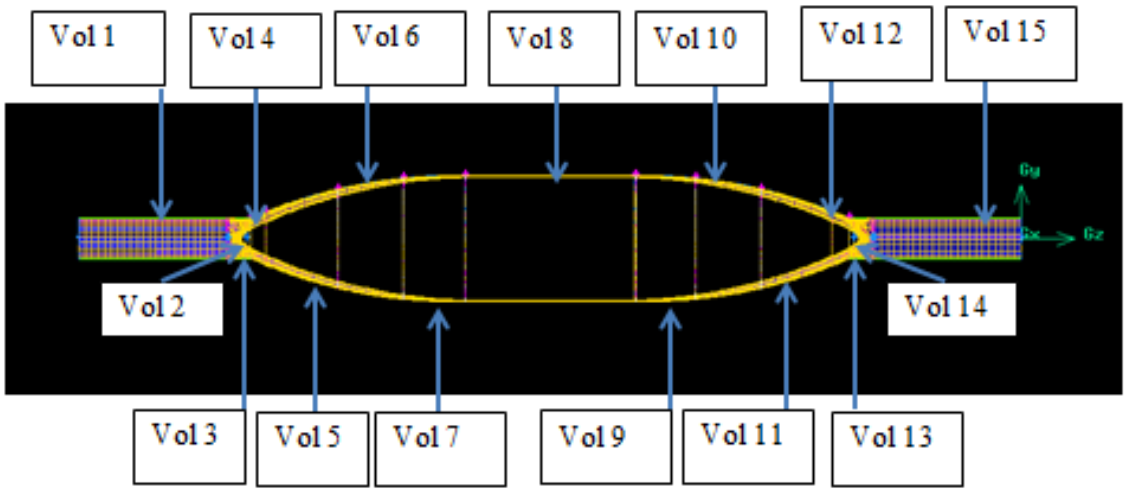

Figure 2.19 Over all view of Mesh 4(466,702 elements)

Figure 2.19 shows the decomposition of the geometry in sub volumes.

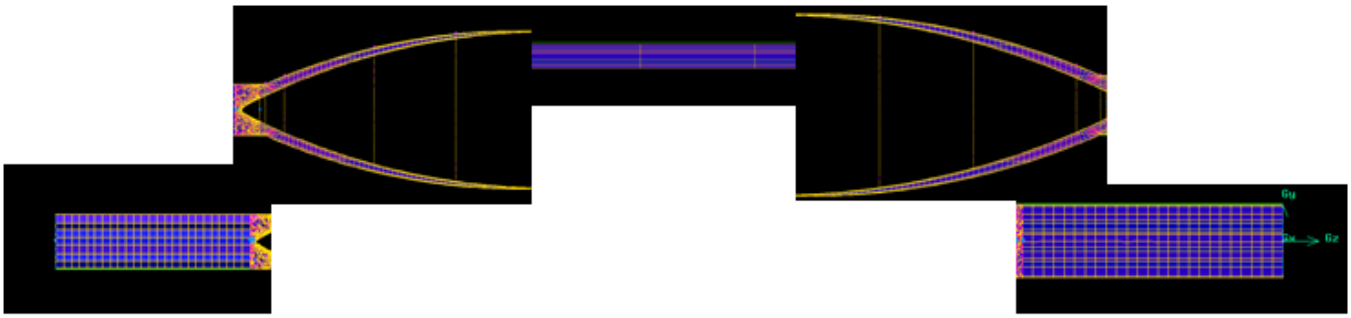

Figure 2.20 Details of Mesh 4

Table 2.4 The setting of Mesh 4 in Gambit

	Mesh Elements	Mesh Type	Interval Size	Number of elements
Volume 1	**Hex/Wedge**	**Cooper**	**0.4**	**1656**
Volume 2	**Tet/Hybrid**	**TGrid**	**1**	**344**
Volume 3	**Hex/Wedge**	**Cooper**	**0.4**	**54698**
Volume 4	**Hex/Wedge**	**Cooper**	**0.4**	**24624**
Volume 5	**Hex/Wedge**	**Cooper**	**0.4**	**39672**
Volume 6	**Hex/Wedge**	**Cooper**	**0.4**	**35568**
Volume 7	**Hex/Wedge**	**Cooper**	**0.4**	**31464**
Volume 8	**Hex/Wedge**	**Cooper**	**0.4**	**91656**
Volume 9	**Hex/Wedge**	**Cooper**	**0.4**	**32832**
Volume 10	**Hex/Wedge**	**Cooper**	**0.4**	**35568**
Volume 11	**Hex/Wedge**	**Cooper**	**0.4**	**39672**
Volume 12	**Hex/Wedge**	**Cooper**	**0.4**	**23256**
Volume 13	**Hex/Wedge**	**Cooper**	**0.4**	**54014**
Volume 14	**Tet/Hybrid**	**TGrid**	**1**	**332**
Volume 15	**Hex/Wedge**	**Cooper**	**0.4**	**1656**

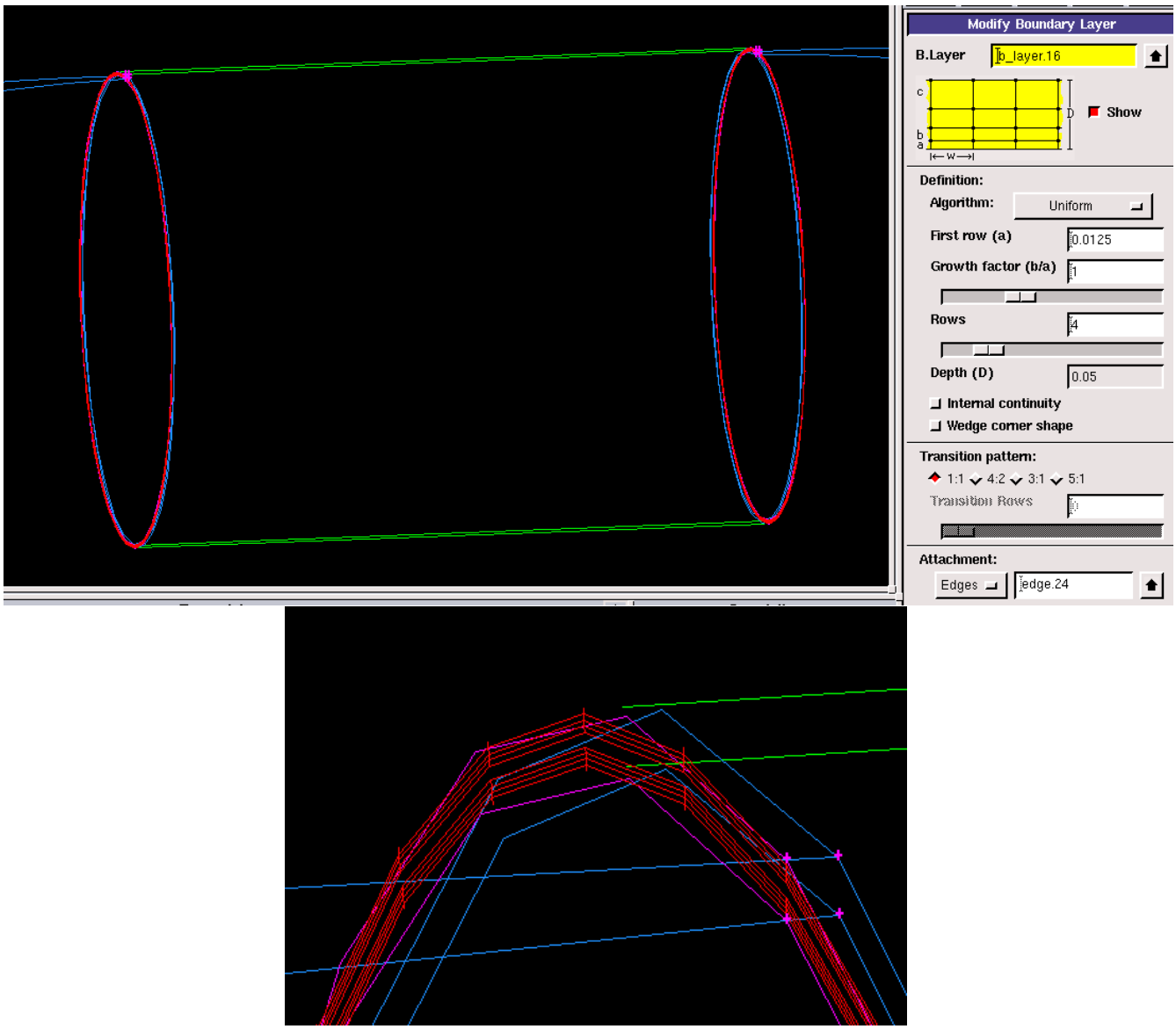

Figure 2.21 Boundary layer in the thin gap section

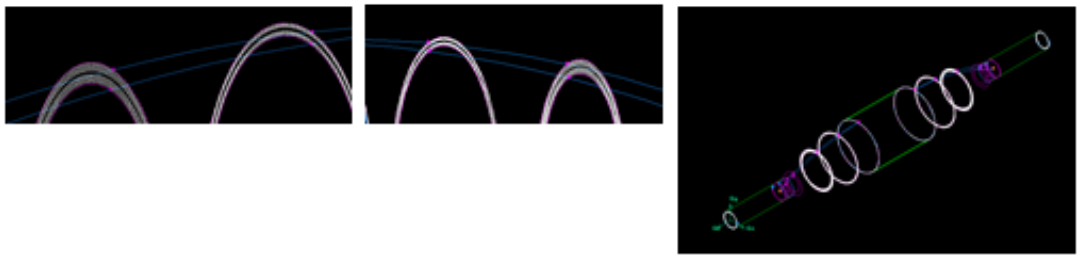

Figure 2.22 Boundary layer in the upstream and the downstream section of the shear gap. The overall boundary layers are shown in the adjacent figure.

In addition, swirling flows often involve steep gradients in the circumferential velocity and require a fine grid for accurate resolution. Rotating boundary layers may be very thin inside the pump model; therefore, sufficient resolution grid near a rotating wall is needed. In order to refine grid resolution near the rotating wall, boundary layer was created. Four rows of boundary layer of size 0.0125 with growth rate of 1 were added at the four edges of the thin gap, Figure 2.21Eight rows of boundary layer of size 0.1 with growth rate of 1 were added at the inlet and outlet boundary edges. Eight rows of boundary layer of size 0.05 and 0.1 with growth rate of 1 were added at the upstream and downstream regions from the shear gap. The overall Boundary layers can be seen in Figure 2.22.

2.1.6 Mag-lev - Design4- Fluent setup

The impeller of the shearing device is magnetically levitated which means the impeller is suspended inside the pump housing without touching walls. Thus the impeller was modeled as rotating at the prescribed rpm while the outer walls of the housing were modeled to be stationary. The uniform velocity that was found from flow rate was set at the inlet (blue) while constant pressure of 200kPa was set at the outlet (red) as shown Figure 2.23. Uniform velocity set at the inlet depending on the flow rate Table 2.5. The inlet radius is 3.175 mm and the area is 3.17e-5 m2.

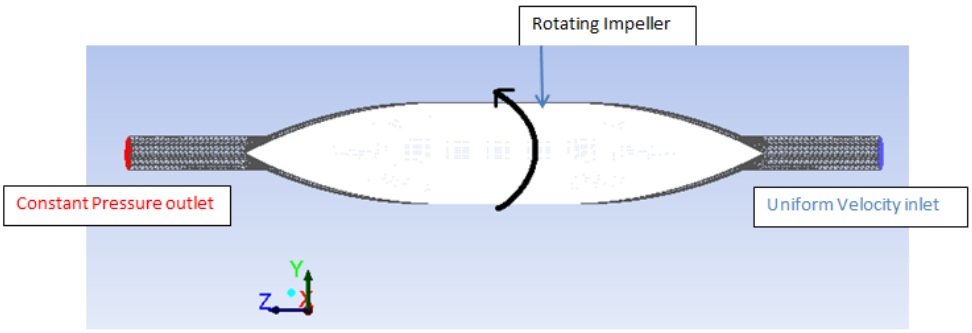

Figure 2.23 Fluent Model of the Modified Mag-Lev shearing Device

Table 2.5 Inlet velocity at Different flow rates

Flow Rate [ml/min]	Flow rate [m3/s]	Velocity [m/s]
50	8.33 E-07	2.63E-02
100	1.67E-06	5.26E-02
150	2.5 E-06	7.89E-02
200	3.33E-06	1.05E-01

The flow rates were kept the same as 50, 100, 150 and 200 ml/min as were used for the previous study. Depending on the flow rates and the inlet area uniform velocity was set at the inlet. Table 2.5, summarizes the data. The impeller walls were modeled as moving walls while all the walls of the housing were modeled to be stationary. Table 2.6 shows the wall conditions for the Mag-lev shearing device.

Table 2.6 Wall conditions for the Mag-lev shearing device

Wall name	**Cell Zone Condition**	**Wall motion**	**Reference Frame**	**Speed [rpm]**
Impeller wall	Moving Reference Frame	Moving wall	Relative to Adjacent Cell Zone	As Prescribed
Wall 1	Stationary	Stationary Wall	Relative to Adjacent Cell Zone	0
Wall 2	Stationary	Stationary Wall	Relative to Adjacent Cell Zone	0
Wall 3	Stationary	Stationary Wall	Relative to Adjacent Cell Zone	0

Fluid Material

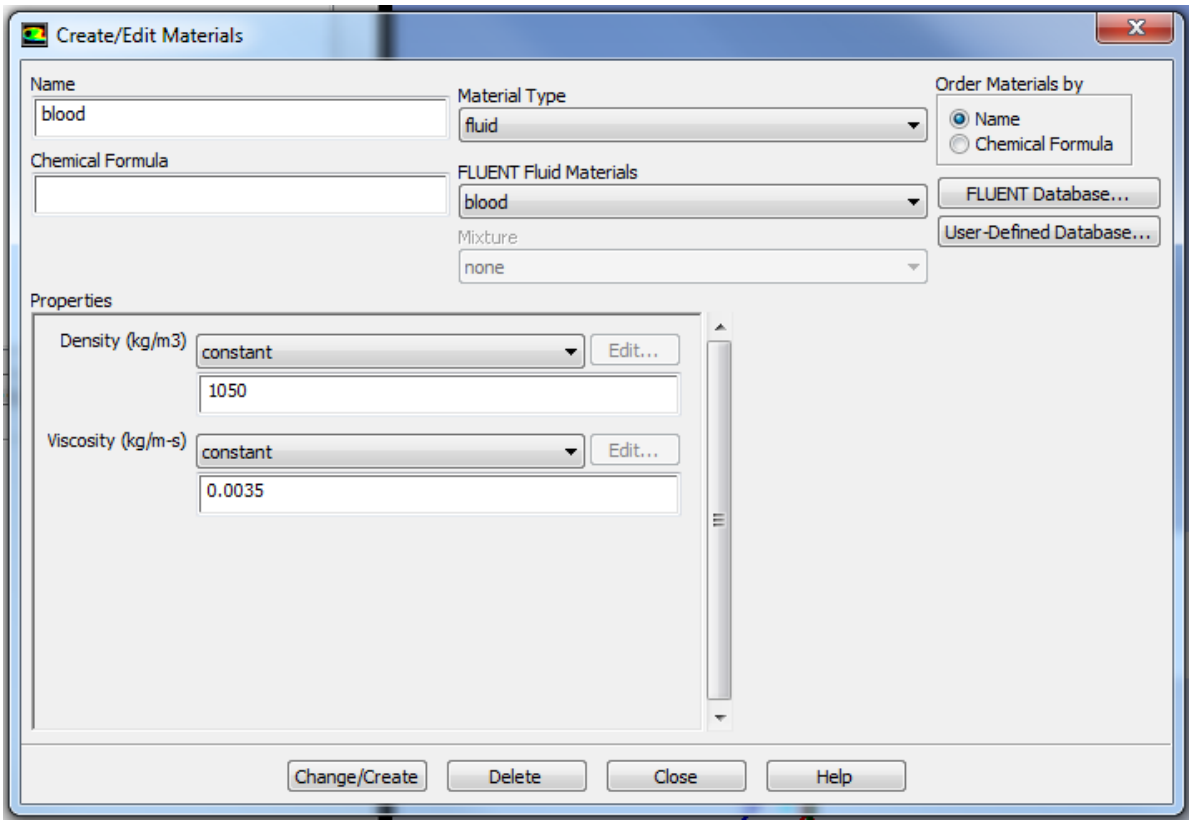

Figure 2.24 Defining Blood properties

Blood was treated as an incompressible Newtonian fluid with a viscosity of 0.0035 Pa-s and density 1050 kg/ m3. Figure 2.24 shows how to set up the blood particle data. For inert particle material, custom “blood-particle” was added with constant blood density of 1050 g/m3

2.2 Flow Calculations

The computational domain of the Mag-lev shearing device, design 4, is composed of the inner impeller the surrounding housing and the fluid modeled as blood. No slip boundary condition was specified at the walls. The inner impeller was specified a rotational speed and outer housing was at zero velocity. Uniform velocity inlet and a pressure outlet were specified and the distance between the inlet and the outlet was maintained so it did not affect the solution. The Reynolds number (Re) at the inlet was 100.203 and 3.94, in the gap so laminar conditions were simulated.

2.3 Hemolysis calculations

Eulerian hemolysis model was defined as a custom field function. After the flow solution was obtained, the damage source term *I* was calculated using the custom field function. The average blood damage was then determined using the flow rate.

2.3.1 Method 1: Eulerian approach

The Eulerian approach determines hemolysis by using a single damage index parameter independent of exposure time

Calculations:

Step 1 – Solution of velocity and pressure

Step 2 – Calculation of average blood damage

Three damage source terms, *I*, were defined with Giersiepen, Heuser and Taskin power law constants:

1. Source term with constants from Giersiepen model

$$I_{GIERSIEPEN} = (3.62 \times 10^{-5})^{1/0.785} \tau^{2.416/0.785}$$

2. Source term with constants from Heuser model

$$I_{HEUSER} = (1.8 \times 10^{-6})^{1/0.765}$$

3. Source term with constants from Taskin model

$$I_{TASKIN} = (1.23 \times 10^{-5})^{1/0.6606} \tau^{1.9918/0.6606}$$

These terms are defined as Custom Field Functions in Fluent and were solved as a post-processing procedure after the flow field solution converged. These functions are shown in Table 2.7

Table 2.7 Setting up of Custom Filed Functions

Fluent Custom Defined Functions	Equations
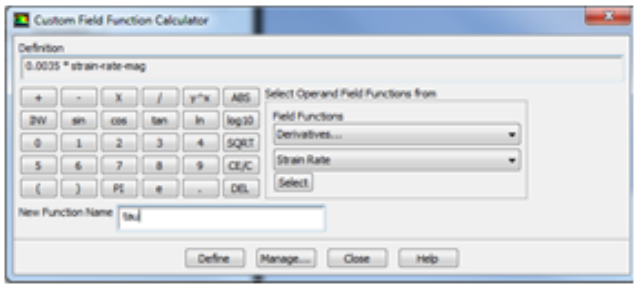	$\tau_{total} = 3.5 \times 10^{-3} \times \varepsilon_{total}$
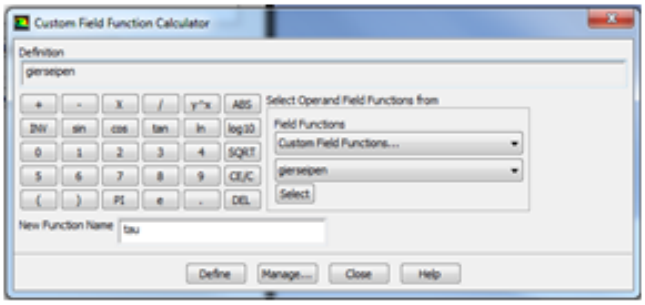	$\sigma = \left(3.62 \times 10^{-5}\right)^{1/0.785} \tau^{2.416/0.785}$
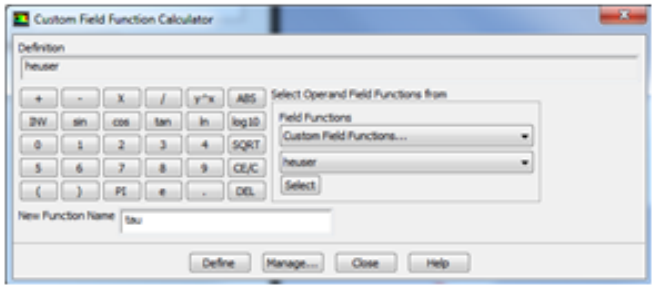	$\sigma = \left(1.8 \times 10^{-6}\right)^{1/0.765} \tau^{1.991/0.765}$
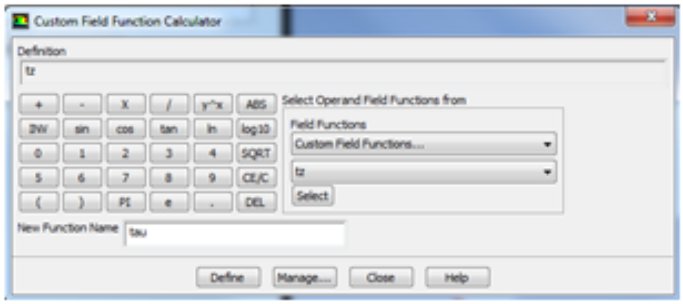	$\sigma = \left(1.23 \times 10^{-5}\right)^{1/0.6606} \tau^{1.9918/0.6606}$

2.3.2 Method 2: Lagrangian Approach

The Lagrangian approach has the ability to calculate the shear stress history on the RBC, which enables the modeling of the prior damage. The power law model shown in (1) below, is used for the calculation of the hemolysis index (HI %)

$$HI\ (\%) = \frac{\Delta Hb}{Hb} \times 100 = \ Ct^{\alpha}\tau^{\beta} \qquad (1)$$

The total hemolysis along a path line from the inlet to the outlet is calculated by integrating the (1),

$$HI = \int_{inlet}^{outlet} C.dt^{\alpha}.\tau^{\beta} = \sum_{inlet}^{outlet} C.dt^{\alpha}.\tau^{\beta} \qquad (2)$$

For the Lagrangian models, path lines were obtained in the post processing after the flow solution was calculated. Parameters for calculating the path lines were chosen so as to get as many path lines to reach the exit as possible. There were between 10 to 500 path lines tracked for the Mag-lev shearing device, design 4. The HI calculations used Matlab (Matlab R2011a, The Math Works Inc. Natick, MA). All the computations were carried out on a PC workstation with Intel(R) Core(TM) 2 Quad CPU 2.40 GHz and 8.00 GB RAM with Windows 7 64-Bit operating system.

Calculations

Step 1 – Solution of velocity and pressure

Step 2 – Massless particles are released to acquire pathline flow field information.

Step 3 – Calculation of damage along pathline using Matlab code

The Power Law Equation constants used for hemolysis calculations are summarized in Table 2.8

Table 2.8 Power Law Equation Constants and their Covering Ranges

Range					
Model	Shear Stress(Pa)	Exposure Time (s)	C	α	β
GW	<255	<700	3.62E−05	0.785	2.416
HO	<700	<700	1.80E-06	0.765	1.991
TZ	50-322	<1500	1.23E-05	0.6606	1.9918

GW, Giersiepen *et al.* constants; HO, Heuser *et al,* constants; TZ, Zhang *et al.* constants;
C α β constants of the power law equation

Results

The following equations were used for calculating the rotational Reynolds number and the Taylor number[21]

Equation 2.1 Rotational Taylor's number

$$Ta_{rot} = Re_{rot}^2 \left(\frac{1}{\eta} - 1\right)$$

Equation 2.2 Rotational Reynolds number

$$Re_{rot} = \frac{U_{rot}}{\nu}$$

Equation 2.3 Gap distance

$$d = R_2 - R_1$$

$R_2 - Outer\ radius$

$R_1 - Inner\ radius$

Equation 2.4 Radius ratio

$$\eta = \frac{R_1}{R_2}$$

Using the above mentioned equations the Taylor number for the wide gap region was calculated analytically.

2.4 Basis of Identification of Taylor vortices

1. Presence of positive and negative axial velocities in axial velocity contour plot in the transverse section
2. A non-parabolic axial velocity profile.
3. Axial velocity vector plot.

2.5 Massless Particle Tracking

2.5.1 To set up the massless particles

The discrete phase model in the Models section is turned on in Fluent. This is followed by clicking on injections. A new injection is created by clicking create. The surface option is selected in Injection Type and inlet is selected from the release from surfaces option. The massless option is turned on in Particle type. The OK button is hit. Figure 2.25 summarizes the process

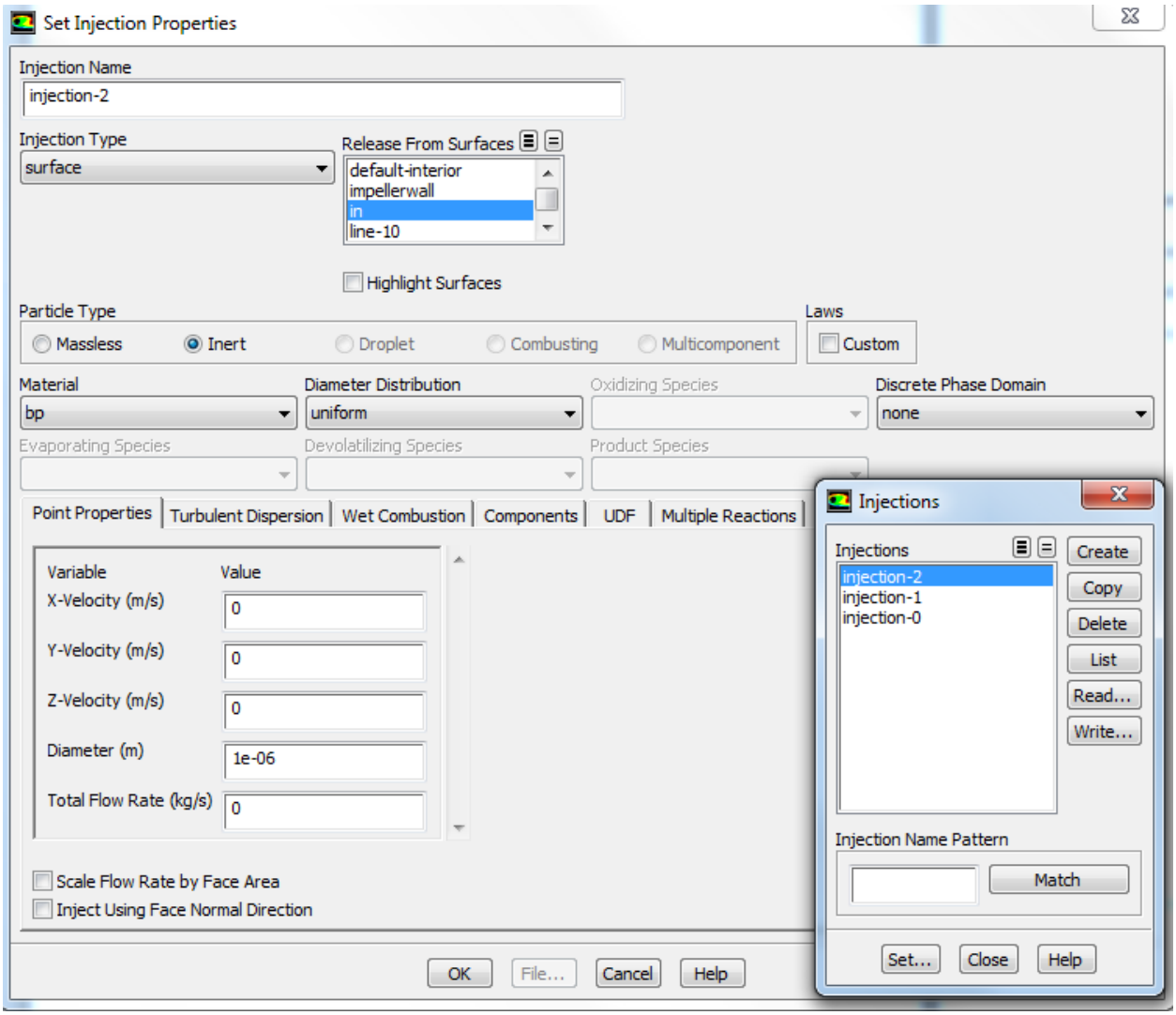

Figure 2.25 Injection 2 is modeled as a mass less particles to be released from inlet.

2.5.2 To release the particles

The particle tracked option is highlighted in the Graphics and Animation console. The Injection created in selected and the particles are released by clicking on Display. The Color by option gives you an option to color the particles according to the required variables. Figure 2.26 shows the Particle Tracks console.

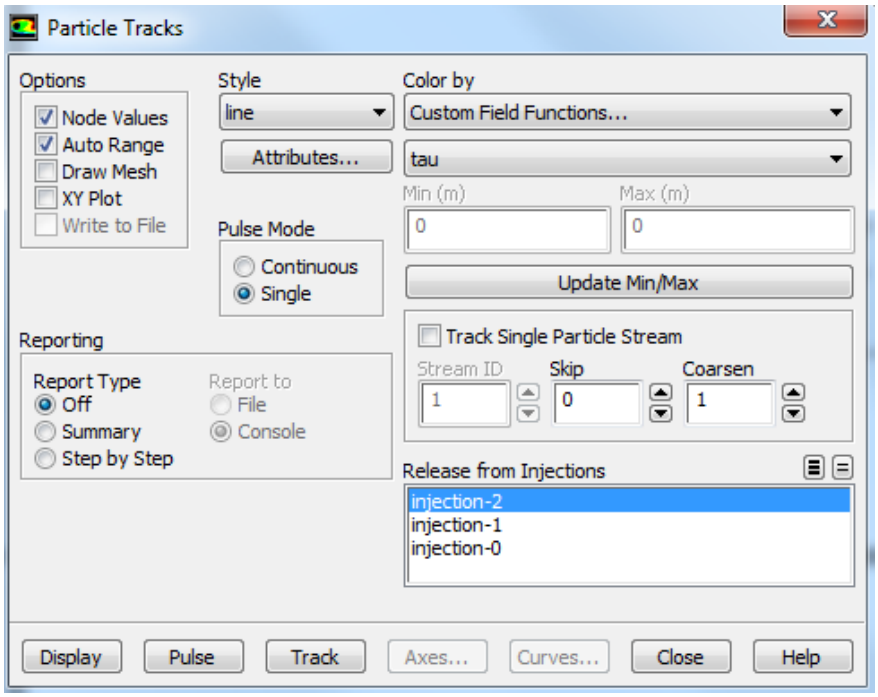

Figure 2.26 Injection 2 is selected which will release massless particles from the inlet. The particles will be colored accordingh to the sheasr stress experiences by each particle

Chapter 3

Flow Analysis

3.1 Design 1- Original design of Maglev shearing device

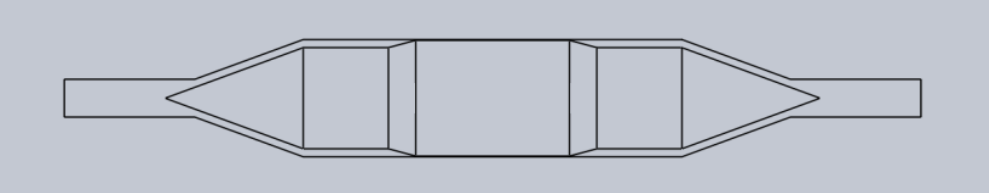

Figure 3.1.1 Design1 of Maglev shearing device

Design 1 of the Mag-Lev sharing device is shown in the Figure 3.1.1. Following steps were taken to analyze the design in Fluent.

Step1- Acquire the velocity and pressure solution.

Step2- Determine whether Taylor vortices exist

Step3- Determine if path lines escape through the outlet.

To find the grid independent solution four different meshes were tested. These were then tested by creating a transverse section in the wide gap region. The transect summary is given in the Table 3.1.1

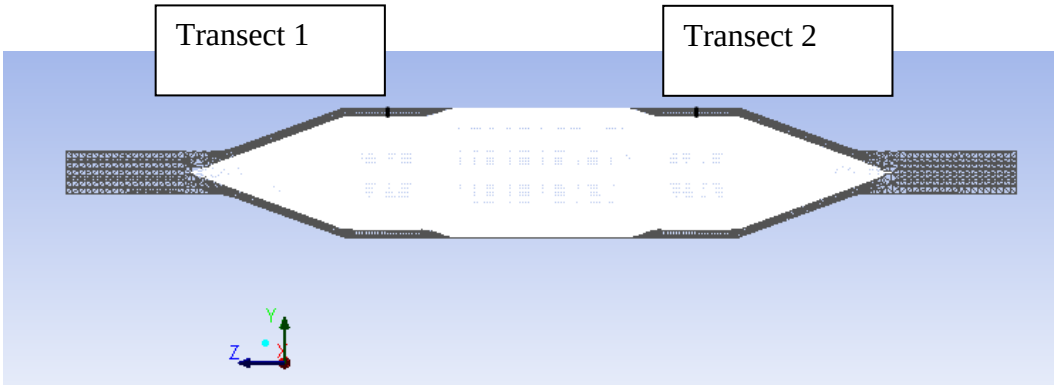

Figure 3.1.2 Position of transects

Table 3.1.1 Transect Summary in Wide gap region

Transect 1 Summary	
x0=0	x1=0
y0= 80 mm	y1=98.5 mm
z0= 4.57 mm	z1= 4.57mm

Transect 2	
x0=0	x1=0
y0= 8 mm	y1=9.85 mm
z0= 97.6 mm	z1= 97.6mm

Figure 3.1.3,Figure 3.1.6shows the axial velocity , Figure 3.1.4, Figure 3.1.7 shows tangential velocity and Figure 3.1.5, Figure 3.1.8 show strain rate plots on the transect in the wide gap region

Transect 1

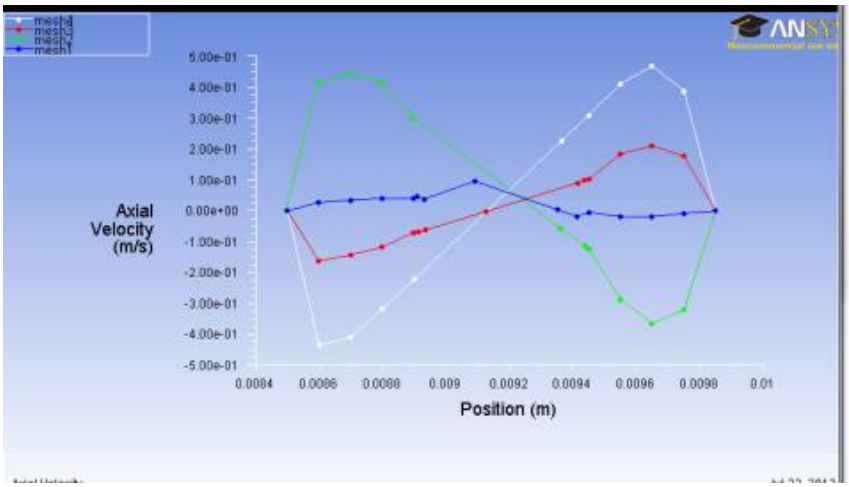

Figure 3.1.3 Axial velocity(m/s)

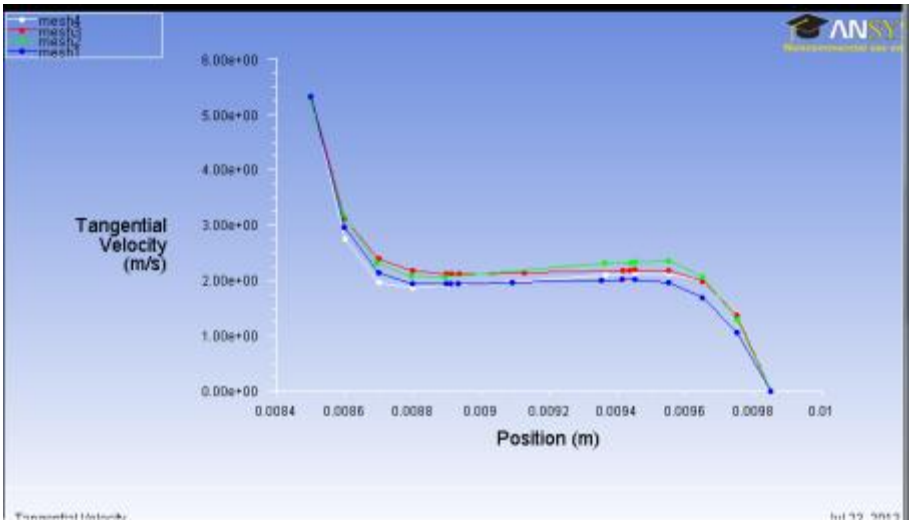

Figure 3.1.4 Tangential velocity(m/s)

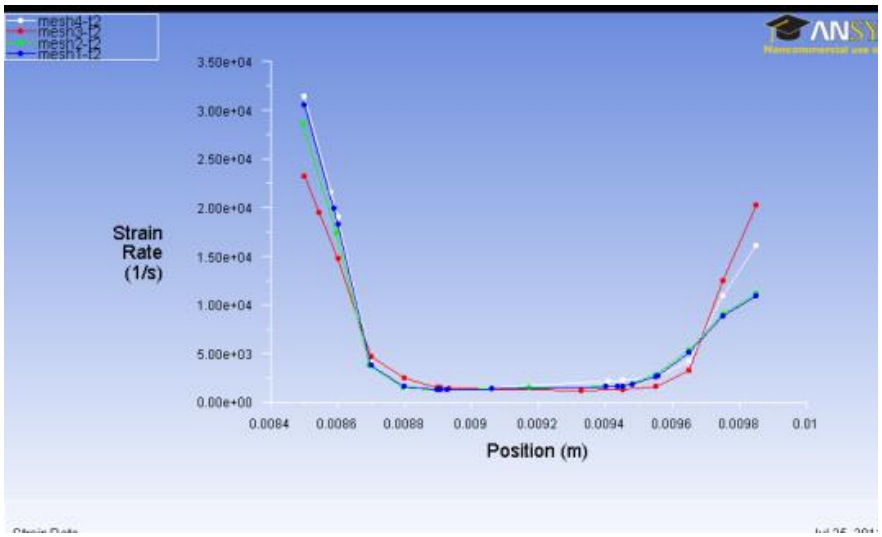

Figure 3.1.5 Starin rate (1/s)

Transect 2

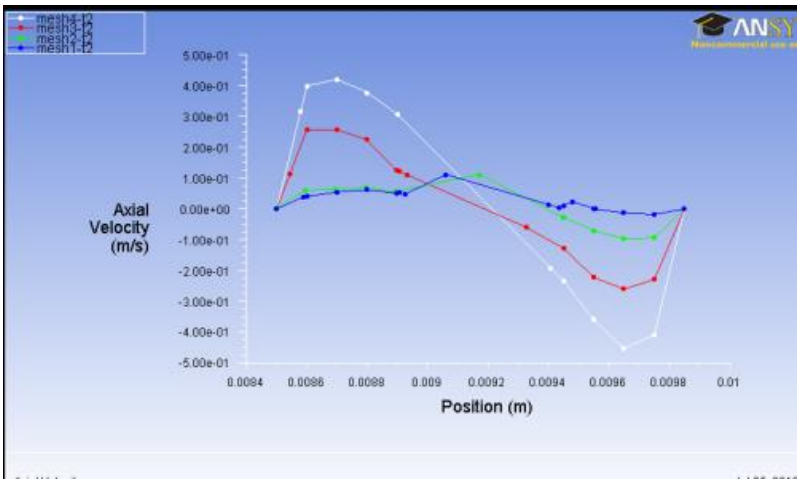

Figure 3.1.6 Axial Velocity(m/s)

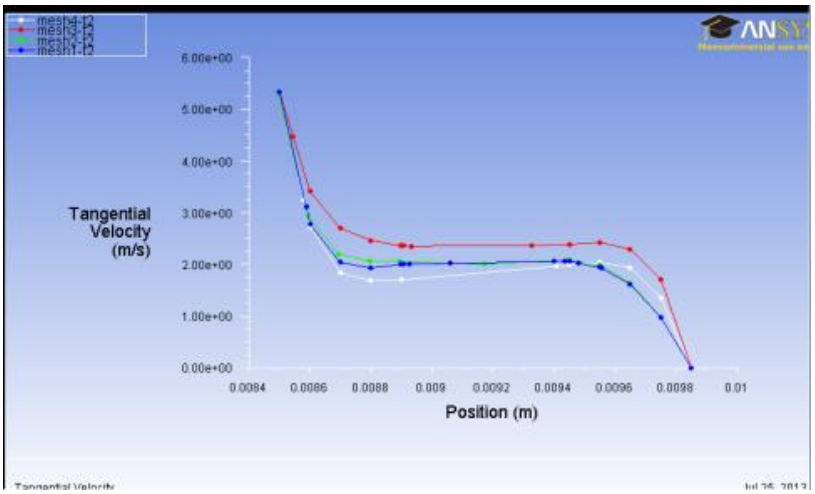

Figure 3.1.7 Tangentail Velocity (m/s)

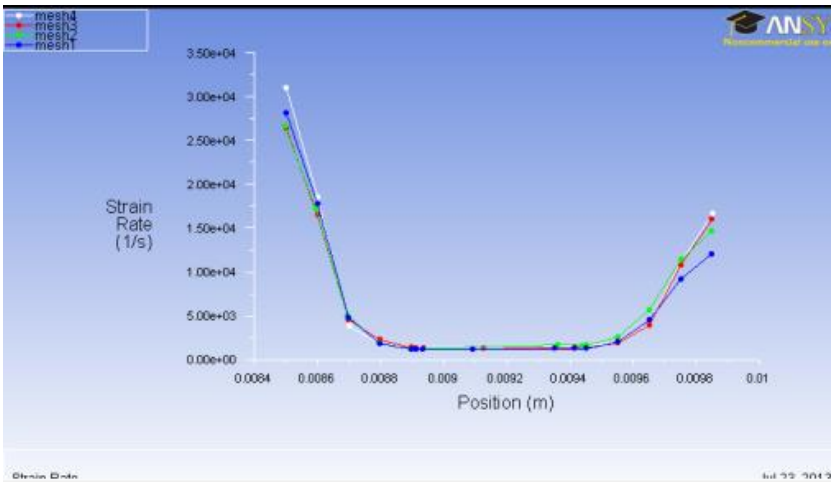

Figure 3.1.8 Strain rate (1/s)

The axial velocity profiles did not show any trend hence the tangential velocity profiles and strain rate profiles were considered for mesh independence. It was observed that the difference were minimal between meshes 2, 3, 4. Mesh 3 was selected for final analysis, since it has an interval size of 0.4 which in the simple geometry setting had predicted the existence of Taylor vortices and also because it has the highest orthogonal quality and lowest aspect ratio amongst all the meshes analyzed, which will be helpful for the pathlines to escape successfully through the outlet. This will be explained in detail later in, orthogonality and successful pathline tracking.

To determine the existence of Taylor vortices, the axial velocity was plotted in cross-sectional plane in mag-lev shearing device model Figure 3.1.9, displays the overall contour plot of axial velocity. In the Figure 3.1.10, negative and positive axial velocities can be seen. This indicates that the velocities in the wider gap region were circulating and there could be Taylor vortices.

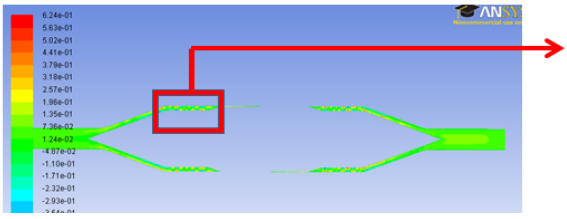

Figure 3.1.9 Contour of Axial velocity [m/s]

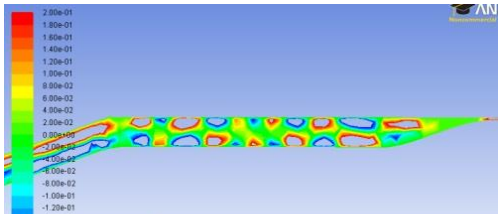

Figure 3.1.10 Detailed view of axial velocity [m/s]

The existence of Taylor vortices is also validated by the numerical solution. The axial velocity profile on a transect in the wide gap region is plotted. The axial velocity profile was sinusoidal, Figure 3.1.12. The tangential velocity profile is nonlinear Figure 3.1.13. Due to much smaller axial velocity, the total velocity magnitude distribution looks similar to the tangential velocity profile Figure 3.1.14. Figure 3.1.11, shows the vector plot in the wide gap region. The recirculation zones can be well seen in the figure.

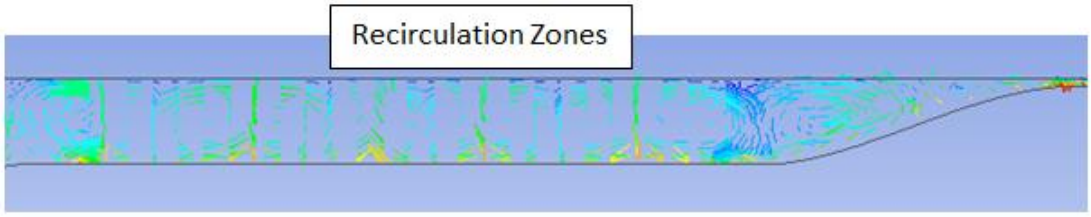

Figure 3.1.11 Recirculation zones in the wide gap region

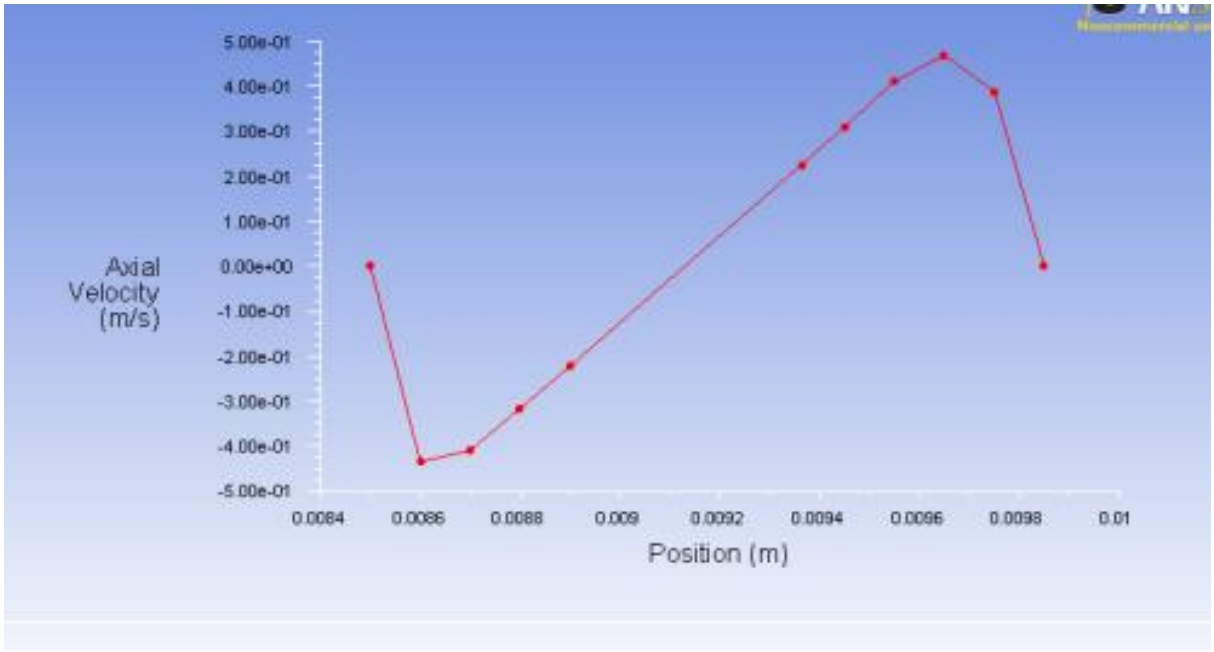

Figure 3.1.12 Axial velocity (wider gap)

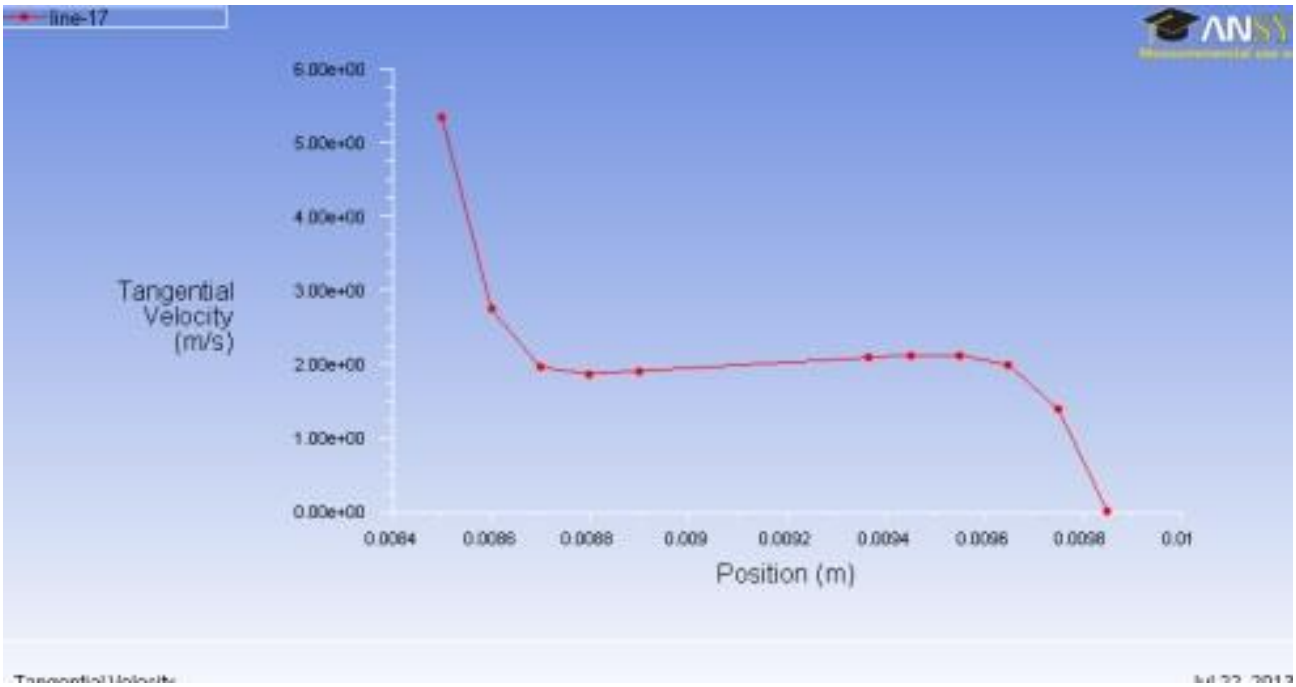

Figure 3.1.13 Tangential velocity (wider gap)

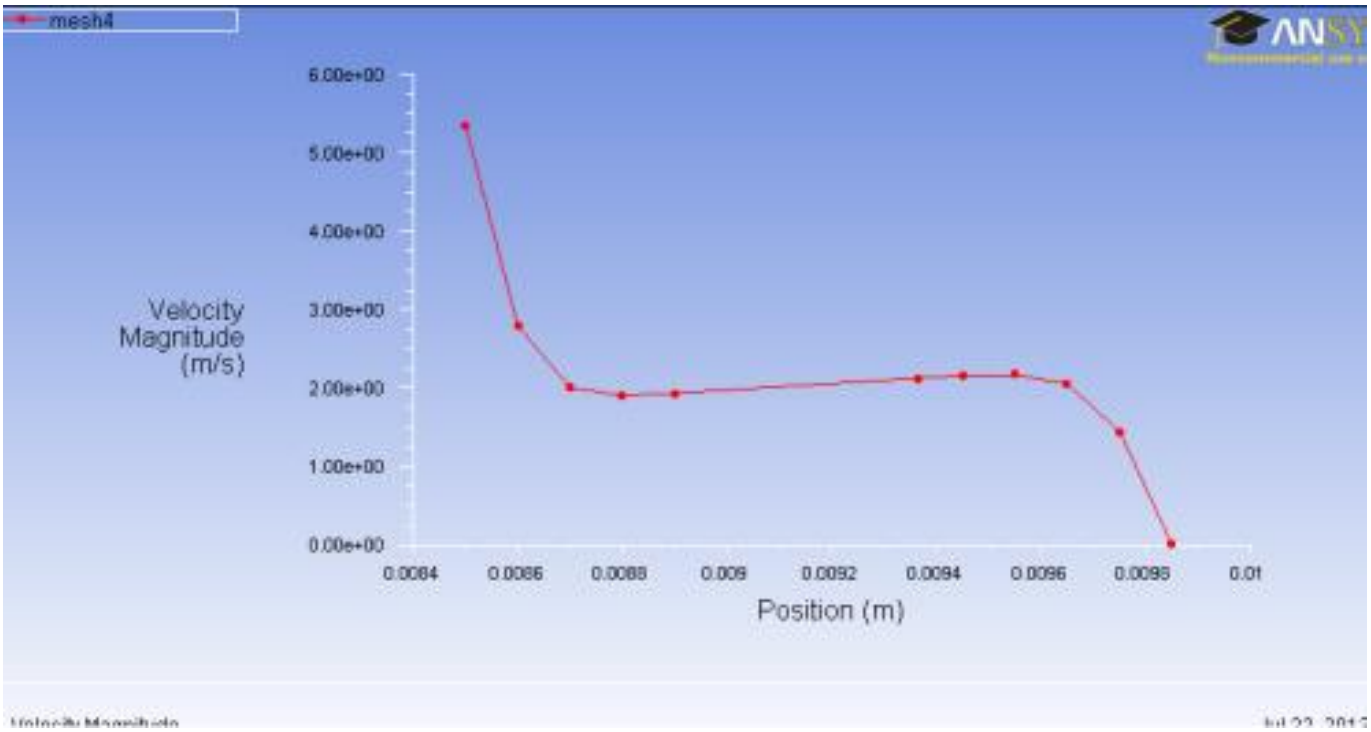

Figure 3.1.14 Total velocity (wider gap

Figure 3.1.15hows the incomplete path lines that were tracked for design 1. This can be compared to Figure 3.1.10 which shows the existence of Taylor vortices.

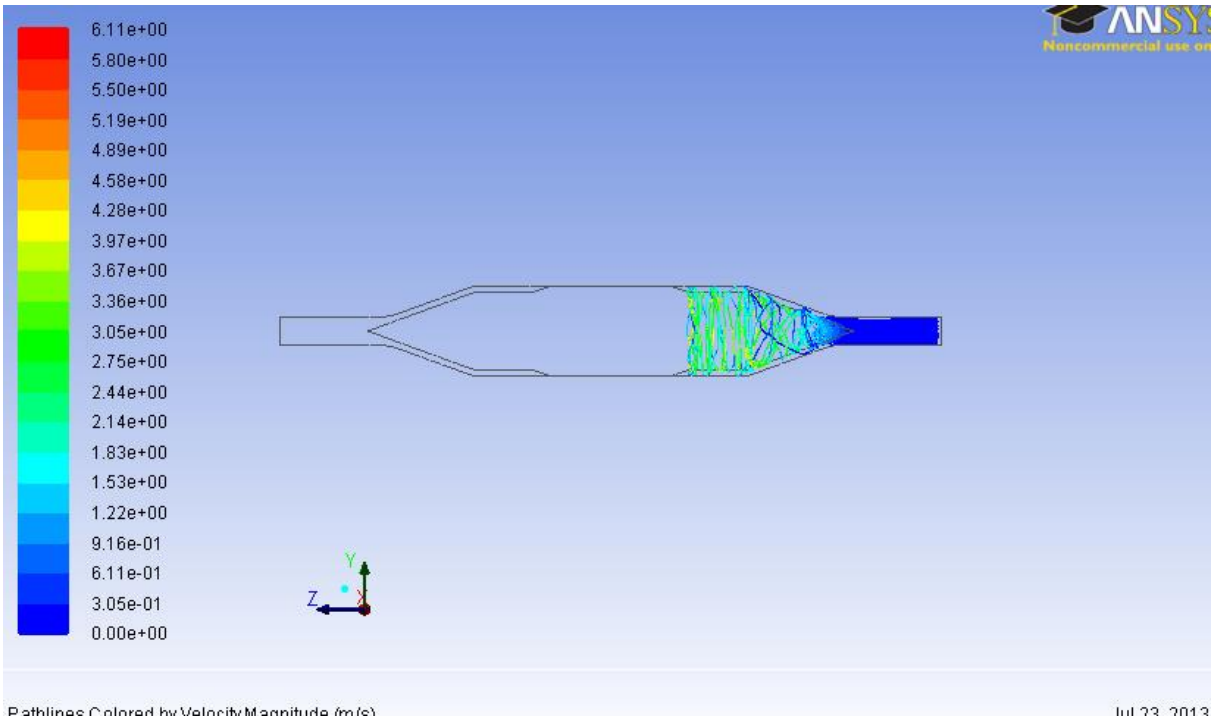

Figure 3.1.15 path lines tracked for Design 1 at 0.1lpm at 6000 rpm

3.2 Design 2- Uniform Gap Design

The Figure 3.2.1 below shows the design for a uniform gap blood shearing device. A gap size of 0.125 mm is maintained throughout the device length.

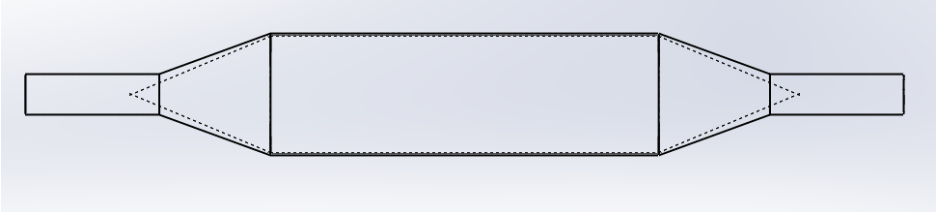

Figure 3.2.1 Uniform gap blood shearing device.

Four different meshes were created for grid independence. A transect was created as shown in the Figure 3.2.2 and axial velocity, tangential velocity and strain profile were evaluated. The results did not differ significantly. Thus, the mesh case in which maximum path lines escaped through the outlet was selected for further analysis. The mesh with interval size of 0.4 was found to have maximum path lines escaping through the outlet. Figure 3.2.3, Figure 3.2.4 below shows axial velocity profile and the axial velocity contour plot for the design 2.

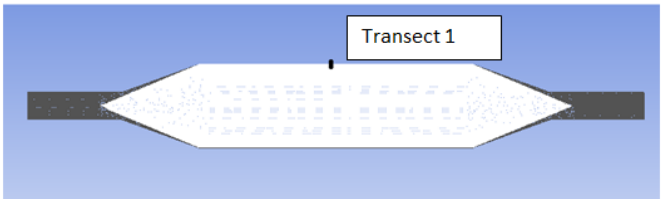

Figure 3.2.2 Section on transverse plane

Table 3.2.1 Transect details

Transect 1	
x0=0	x1=0
y0= 8 mm	y1=9.85 mm
z0= 60 mm	z1= 60mm

Table 3.2.1 gives the details of the transect created.

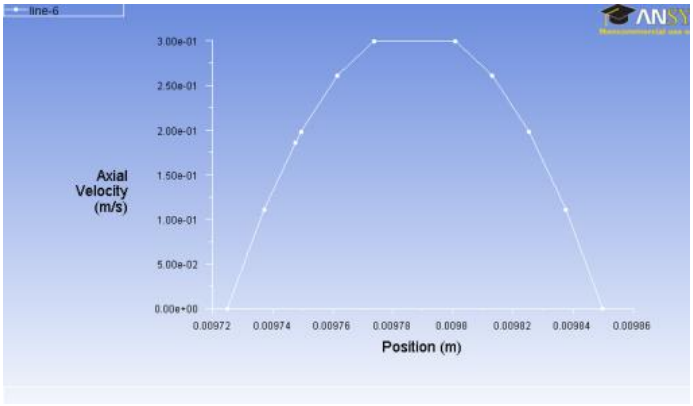

Figure 3.2.3 Axial velocity profile in the thin gap region

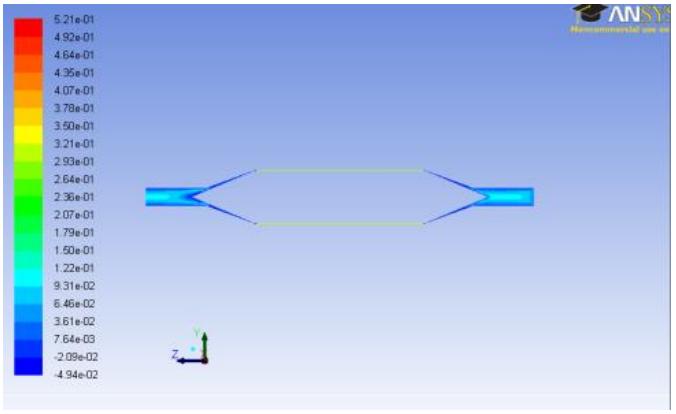

Figure 3.2.4 Axial Velocity Contour plot

The mesh with an interval size of 0.4 was selected for further analysis. The highest rpm at which at least 1 path line successfully escaped the outlet was 4000 rpm. Hemolysis was evaluated at 3000 rpm where 262 path lines escaped through the outlet out the 462 tracked, a (50%) success rate. At 6000 rpm no path lines escaped the outlet.

It is important to note that at 6000 rpm **no vortices** or recirculation zones were detected in the flow path, however in spite of this **no pathlines** escaped through the outlet. This might be due to the mesh inaccuracies. The vector plot of design 3 at 6000 rpm was shown in Figure 3.2.5. It can be seen that no vortices or recirculation zones were seen at the inlet or the uniform gap region.

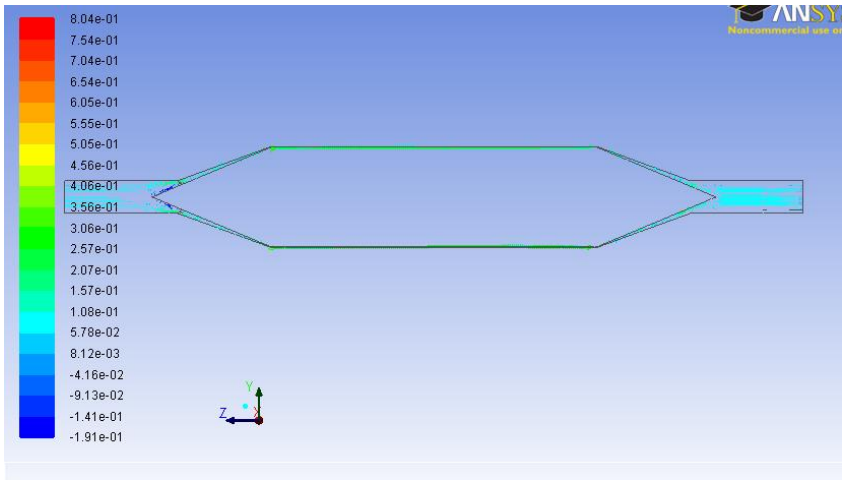

Figure 3.2.5 Vector plot of Axial velocity in transverse section for uniform gap design, Design 3

The highest rpm at which the pathlines successfully escaped the outlet was at 3000 rpm. The Figure 3.2.6 shows the contour plot of shear stress at 3000 rpm at 0.1 lpm.

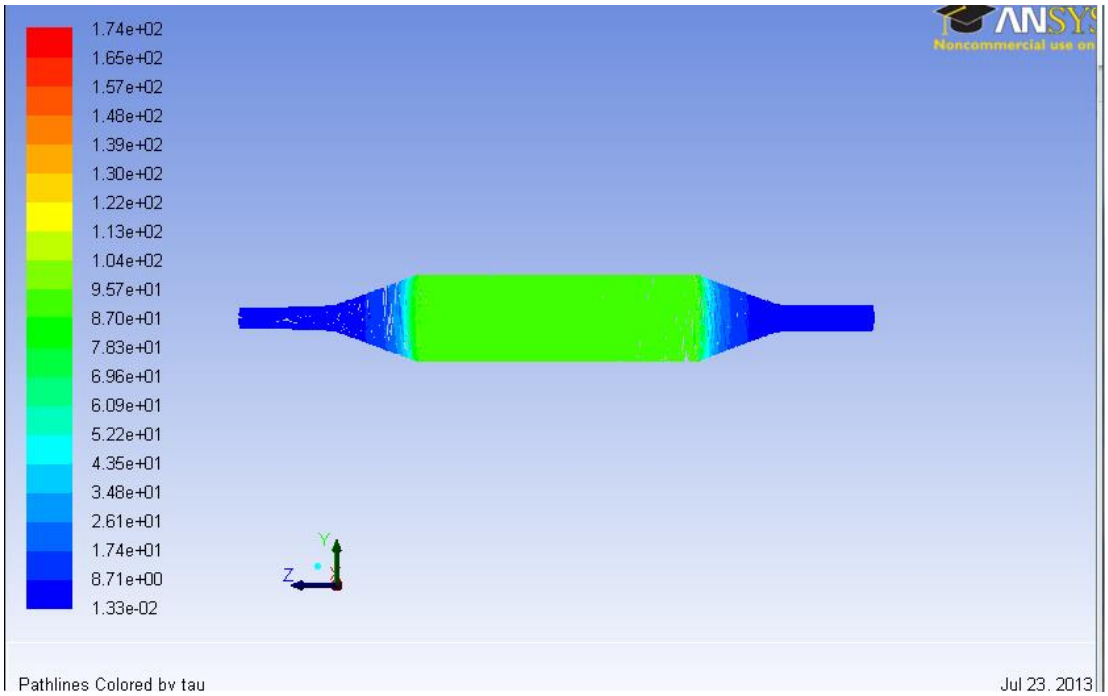

Figure 3.2.6 Contour plot of shear stress at 3000 rpm.

The Table 3.2.2 below summarizes the Shear stress damage and exposure time, simulation and analytical.

Table 3.2.2 Shear stress and exposure time for the uniform gap blood shearing device

	Shear stress-τ (Pa)	**Exposure time-*t*exp (s)**
Simulation	87	0.2
Analytical	85.54	0.295

Figure 3.2.7shows the scalar shear stress along the path length and Figure 3.2.8, shows the shear stress *vs.* the residence time for the particles though the uniform gap design

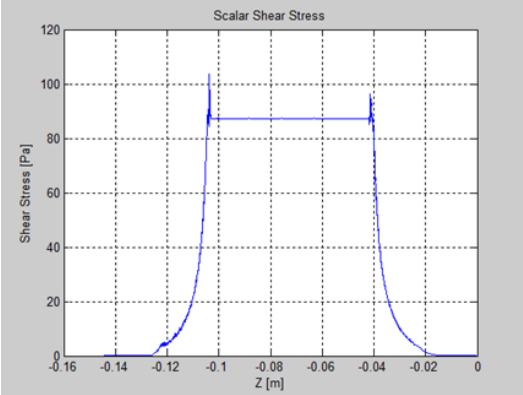

Figure 3.2.7 Shear stress vs Z

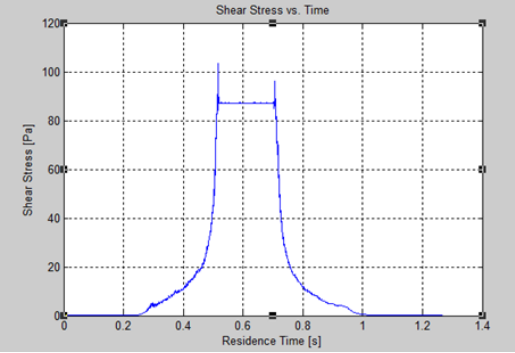

Figure 3.2.8 Shear stress vs Residence time

Figure 3.2.9shows the blood damage distribution along the length of the Design 2.

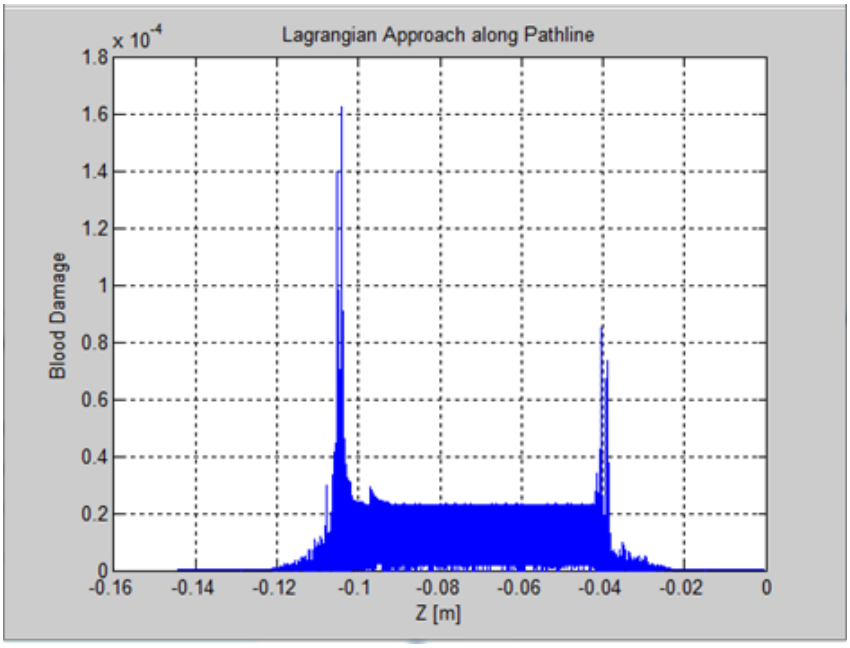

Figure 3.2.9Blood damage along the z axis for design 2.

3.3 Design 3- Linearly increasing gap

Flow analysis of Design 3-Linear increasing gap design

Figure 3.3.1 shows the cross sectional model of design 3 of Mag-lev shearing device. The linearly increasing gap upstream and downstream the shear gap can be seen.

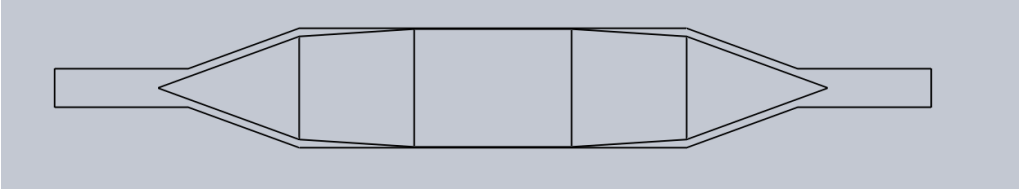

Figure 3.3.1 Design 3 of Mag-Lev sharing device.

Figure 3.3.2 shows the position of the transect used for mesh independence study Table 3.3.1 summarizes the position of the transects.

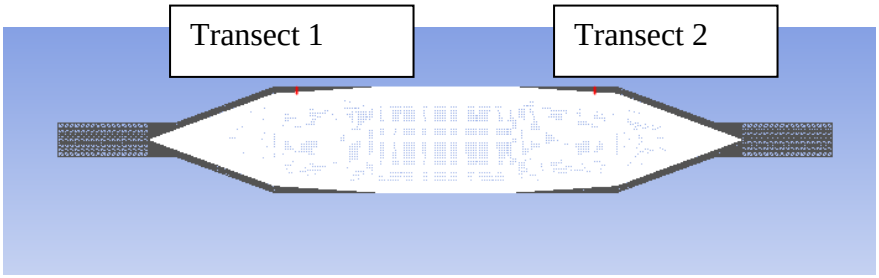

Figure 3.3.2 Position of transects on the transverse plane

Table 3.3.1 Summary of the transects used for mesh independence.

Transect 1		**Transect 2**	
x0=0	x1=0	x0=0	x1=0
y0= 7 mm	y1=9.85 mm	y0= 7 mm	y1=9.85 mm
z0= 102 mm	z1= 102 mm	z0= 42.35 mm	z1= 42.35mm

Figure 3.3.3,Figure 3.3.6 show the axil velocity, Figure 3.3.4, Figure 3.3.7show the tangential velocity, Figure 3.3.5, Figure 3.3.8 strain rate on the transects used for mesh independence study.

Transect 1

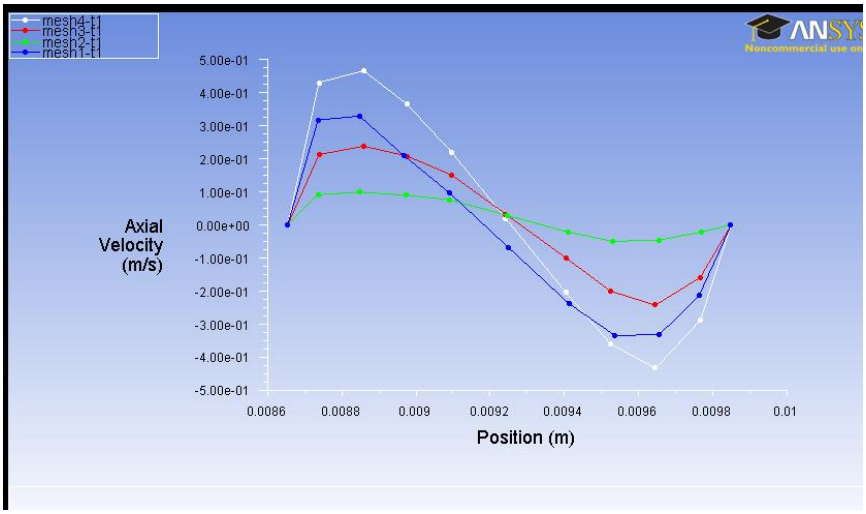

Figure 3.3.3 Axial velocity plot (m/s)

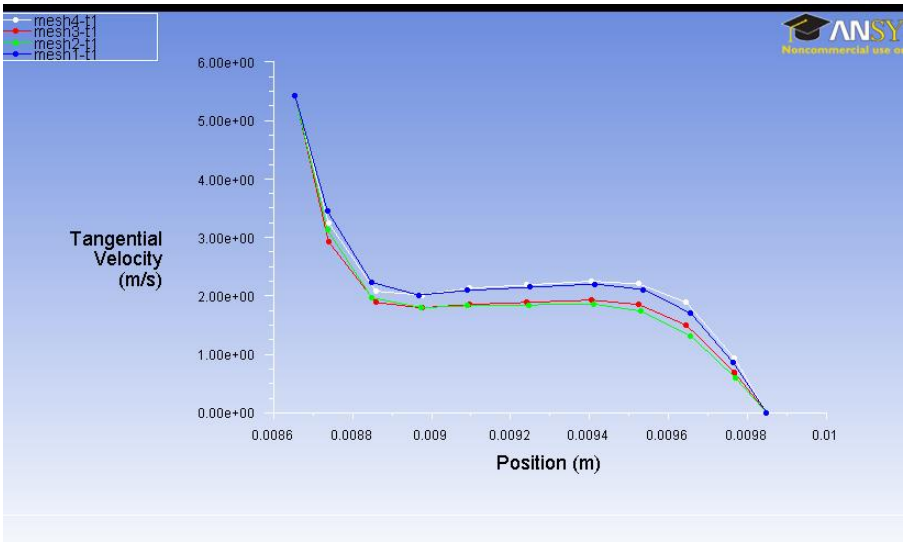

Figure 3.3.4 Tangentail velocity (m/s)

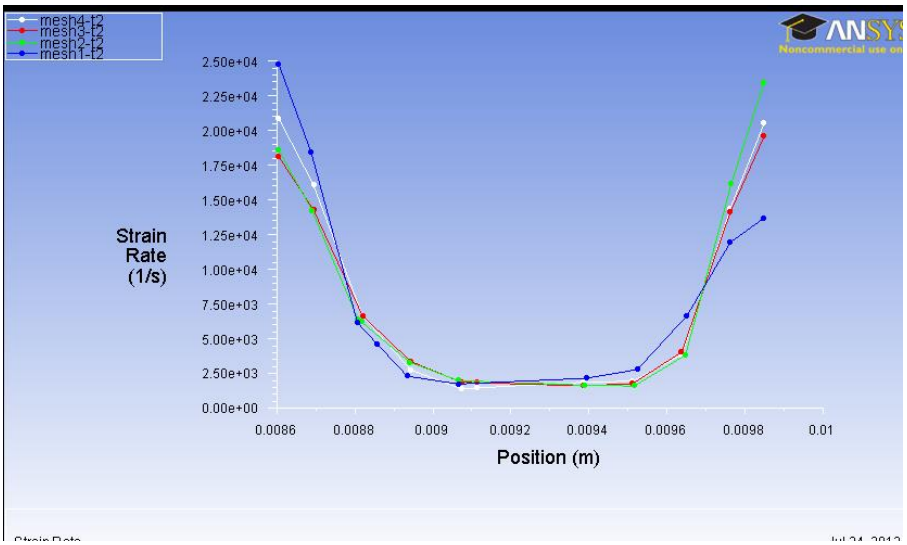

Figure 3.3.5 Strain rate (1/s)

Transect 2

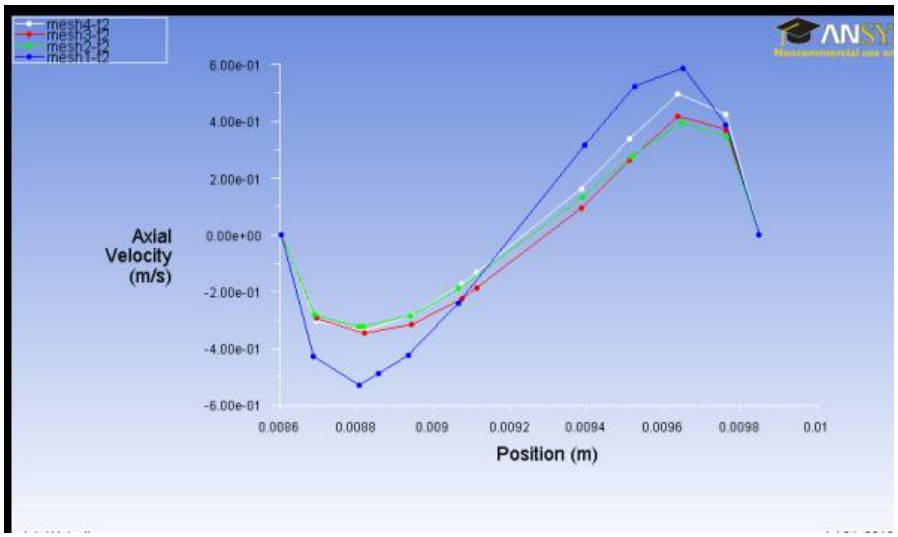

Figure 3.3.6 Axial velocity plot(m/s)

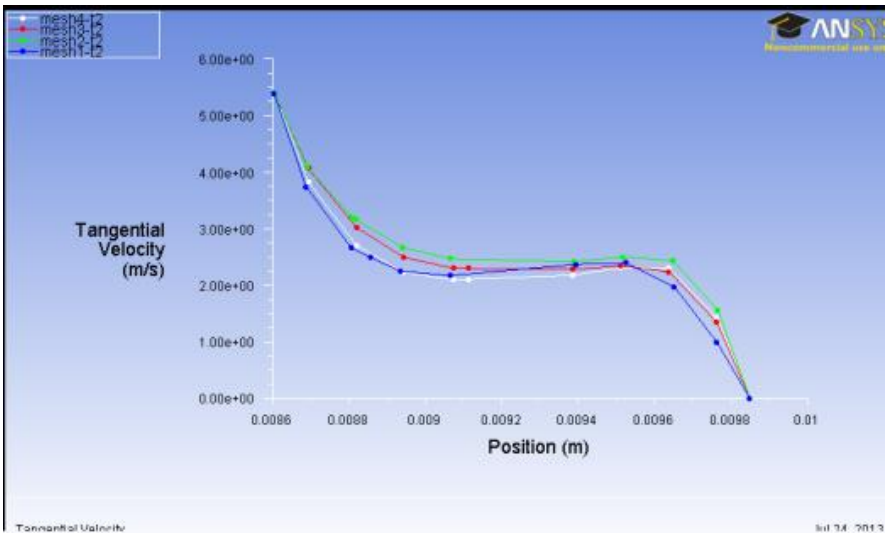

Figure 3.3.7 Tangential velocity (m/s)

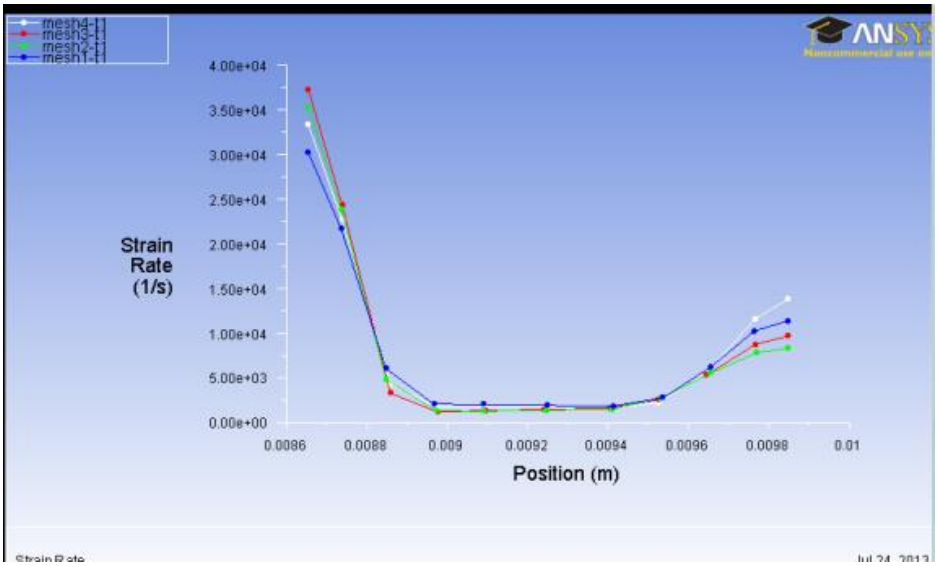

Figure 3.3.8 Strain rate (1/s)

A similar approach as used for design 1 was used for design 3.It was observed that differences decreased from mesh 2 to mesh 3. So mesh 3 was selected for further analysis as a finer interval size was used for this mesh.

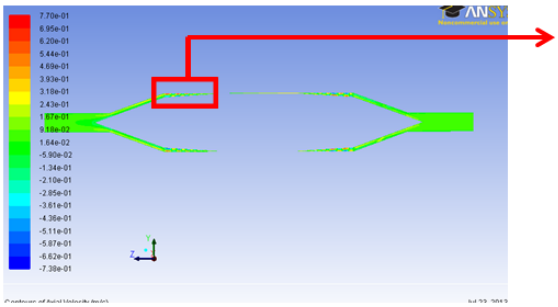

Figure 3.3.9 Contour of Axial velocity [m/s]

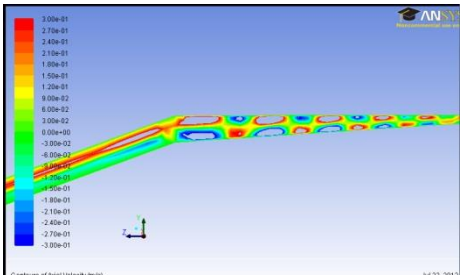

Figure 3.3.10 Detailed view of axial velocity [m/s]

Similar to Design 1 the Taylor vortices were detected at the downstream and upstream of the shear gap region at 8000 rpm as seen in Figure 3.3.9, Figure 3.3.10. Figure 3.3.11 shows the recirculation zones.

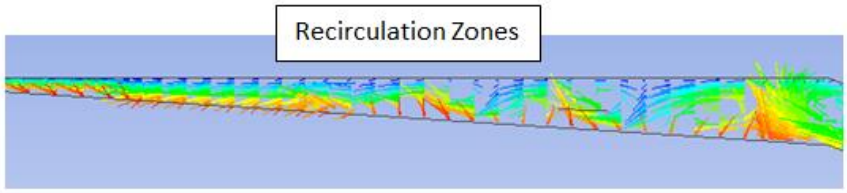

Figure 3.3.11 Recirculation Zones upstream the shear gao region for Design 2

Velocity and Strain plots for the linearly increasing gap region. Figure 3.3.12shows the axial velocity which is not parabolic while Figure 3.3.13 shows the tangential velocity and Figure 3.3.14 shows the total velocity.

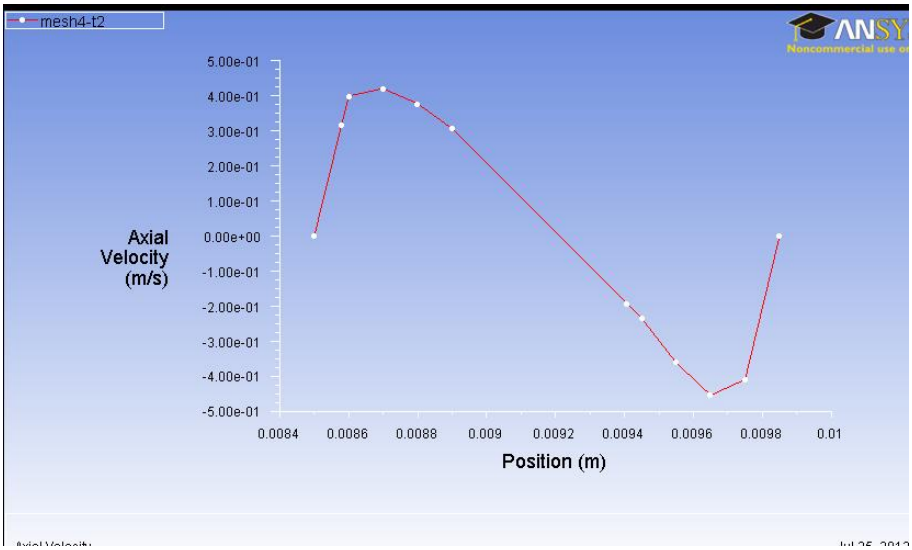

Figure 3.3.12 Axial velocity (wider gap)

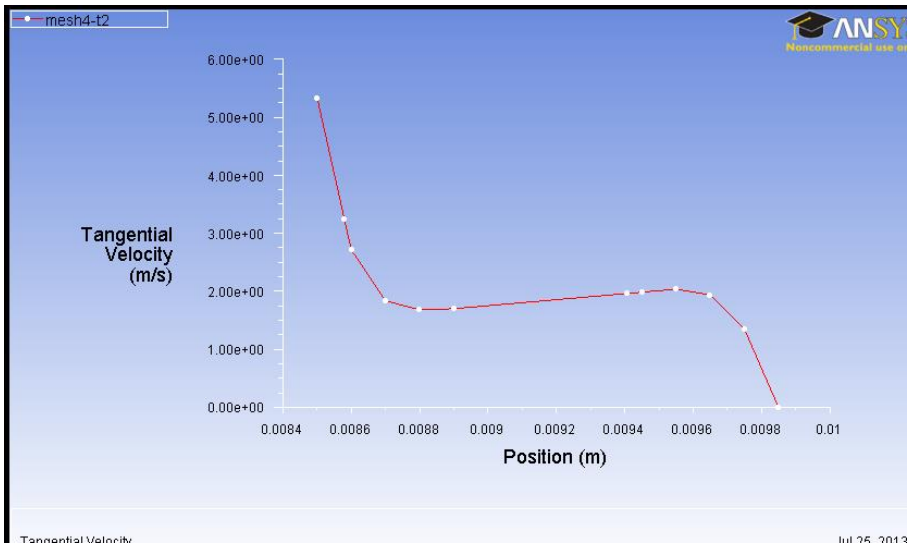

Figure 3.3.13 Tangential velocity (wider gap)

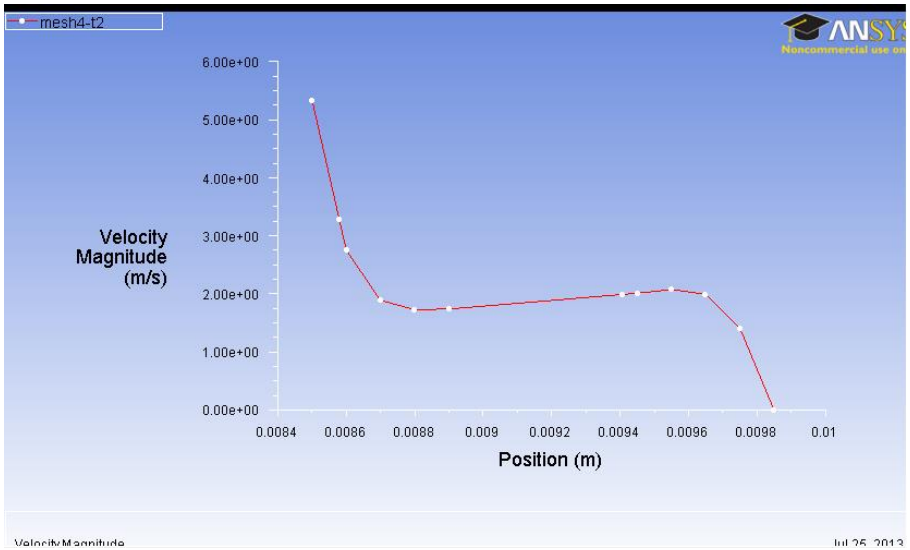

Figure 3.3.14 Total velocity (wider gap)

Due to much smaller axial velocity, the total velocity magnitude distribution looks similar to the tangential velocity profile.

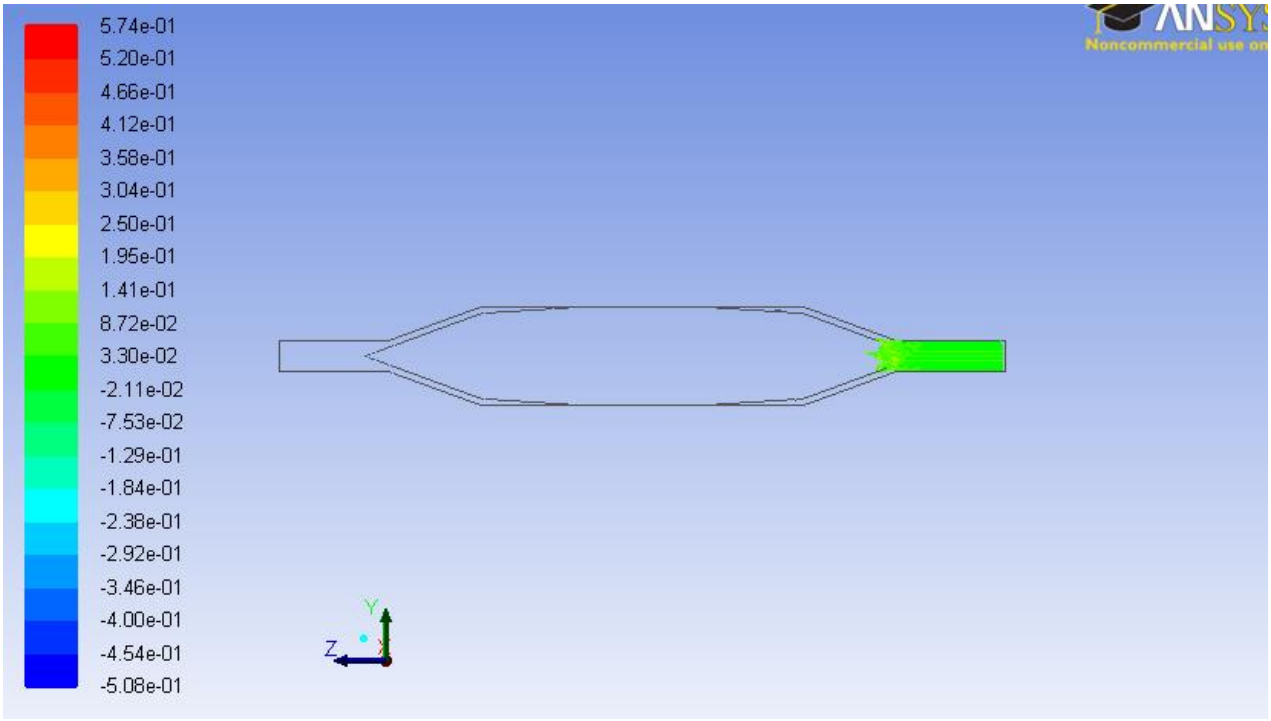

Figure 3.3.15 Path lines tracked for Design 2 at 0.1lpm at 6000 rpm

Figure 3.3.15, shows the pat lines tracked for design 3.It can be seen that the path lines do not make it beyond the tip of the impeller at the inlet side. It is important to note that the vortices appear to be in the linear gap region upstream and downstream after the shear gap. The mesh fineness can be the reason for the particles getting stuck.

3.4 Design 4- Curved Gap design

The wide gap upstream and downstream of the shear/thin gap for Mag Lev Shearing Device 1, design 1, was susceptible to Taylor vortices. This resulted in the particles being trapped in the wide gap. In order to track the particles till the outlet, an intuitive attempt was made to redesign the upstream and the downstream region of the shear gap and the effect on the tracking of particles was observed. It was found that that with the design modification particles could be tracked from the inlet to the outlet. The ensuring sections discuss the methods and the calculations performed to predict the blood damage HI (%) in the modified design

The computational model consists of an impeller and an outside housing similar to the Mag-Lev shearing device. The smallest gap between the housing and the impeller is 0.125mm. A cross section of the device is shown in Figure 3.4.1. Table 3.4.1 shows the details of mesh refinement.

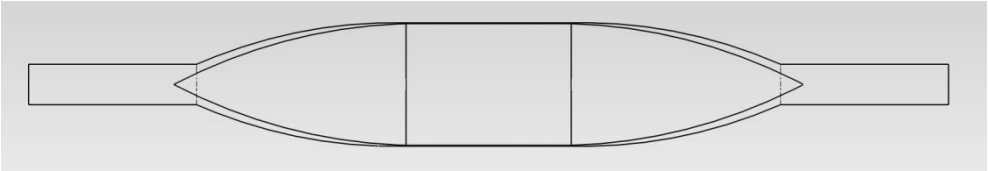

Figure 3.4.1 Cross section of the design 4 showing the modified gap region

Table 3.4.1 Details of the mesh used for grid independence

Mesh	Size (Million cells)	Interval size
1	4.8	Mixed (0.3 & 0.4)
2	4.6	0.4
3	2.18	0.5
4	1.98	0.6

For the Mixed interval size tested, an interval size of 0.3 was used for meshing in the region upstream and downstream of the shear gap i.e. Volume 6 and Volume 8.

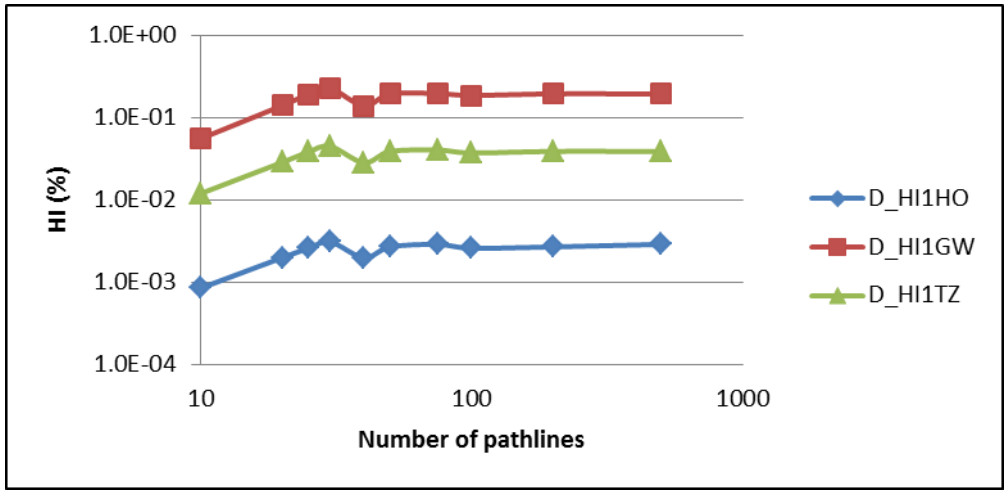

Figure 3.4.2 Variation in the HI(%) estimation according to the path lines

The variation in the HI (%) prediction was tested for increasing path lines, which is shown in Figure 3.4.2. Particles were modeled as massless particles and were released from inlet. This was done at a constant speed of 500 rpm. Beyond 50 particles there was no significant change in the hemolysis prediction. Hence for the final simulation 72 particles were released from the inlet. Also when particles are modeled as massless particles, Fluent automatically releases 72 particles from the surface selected for release. The step size settings were determined such that maximum particles escaped the outlet of the device

3.4.1 Grid Independent solution

In Figure 3.4.3, the grids on transverse plane and impeller walls can be seen. In order to find grid independent solution, two sections on transverse plane were used. The results on these sections were then compared for all different mesh cases.. Transect 2 and 3 locations are summarized in Table 3.4.2

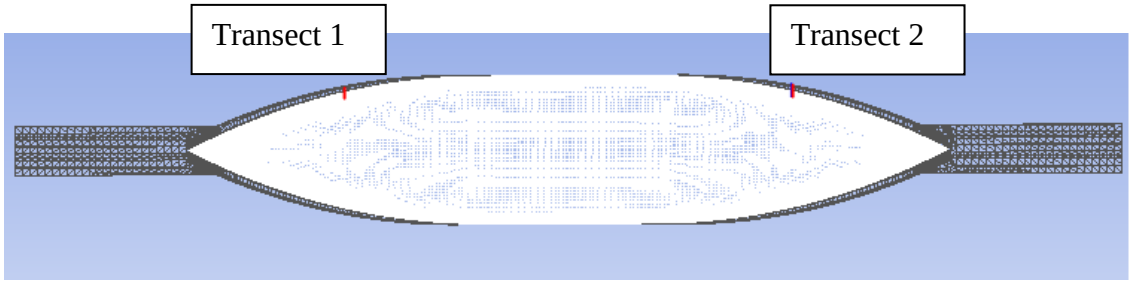

Figure 3.4.3 Sections on Transverse plane

Table 3.4.2 Summary of Transect Dimensions

Transect 1		Transect 2	
x0=0	x1=0	x0=0	x1=0
y0= 7.7 mm	y1=9.5 mm	y0= 7.7 mm	y1=9.5 mm
z0= 47.35 mm	z1= 47.35mm	z0= 98.35 mm	z1= 98.35mm

Figure 3.4.5, Figure 3.4.4 shows that the axial velocity difference on Transect 2and 1 for different meshes are decreasing as the mesh refined. This was done at a test case of 500 rpm.

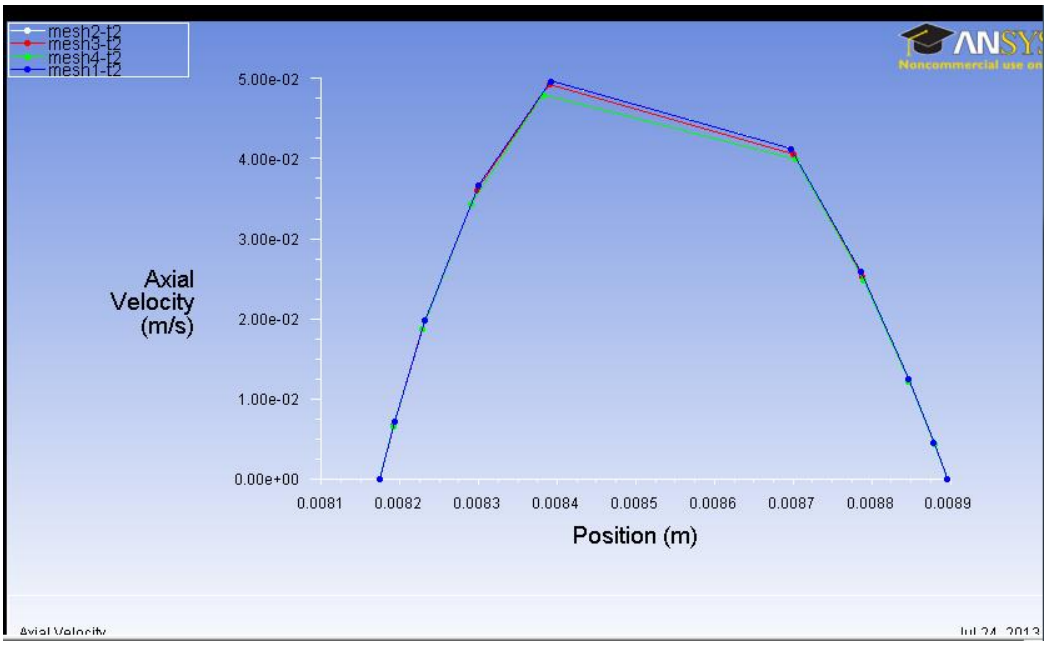

Figure 3.4.4 Axial velocity [m/s] on Transect 1

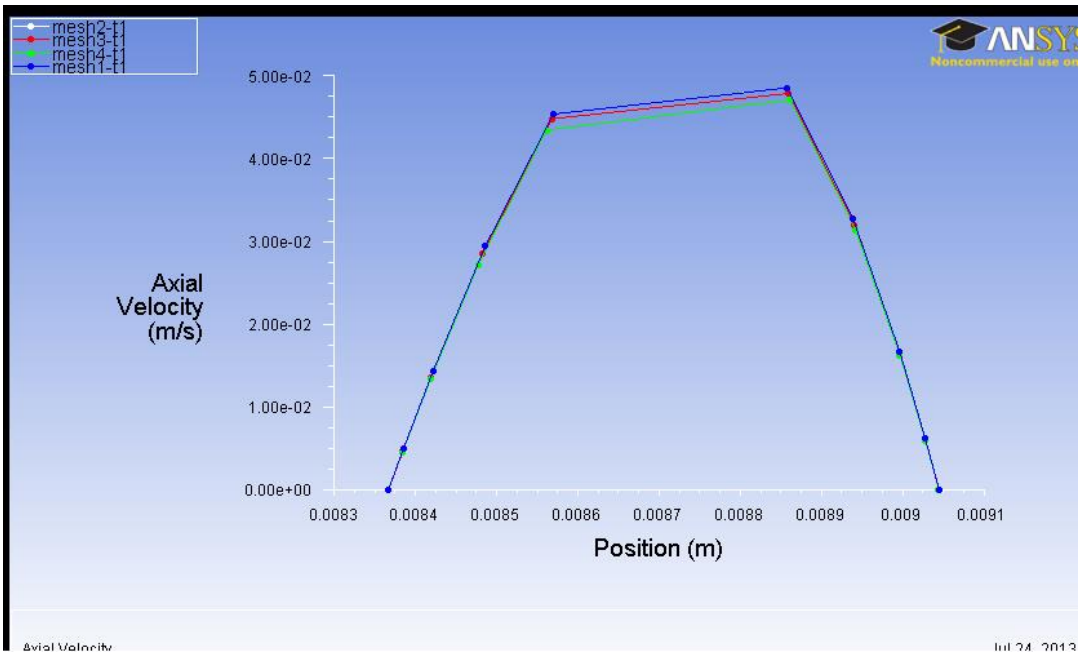

Figure 3.4.5 Axial velocity [m/s] on Transect 2

Figure 3.4.6, Figure 3.4.7 shows that the strain rate difference on Transect 2 and 3 for different meshes are decreasing as the mesh refined. It was concluded that the changes from Mesh1 to Mesh2 is very little. Therefore, Mesh2 was chosen as a grid independent mesh and used to acquire solution

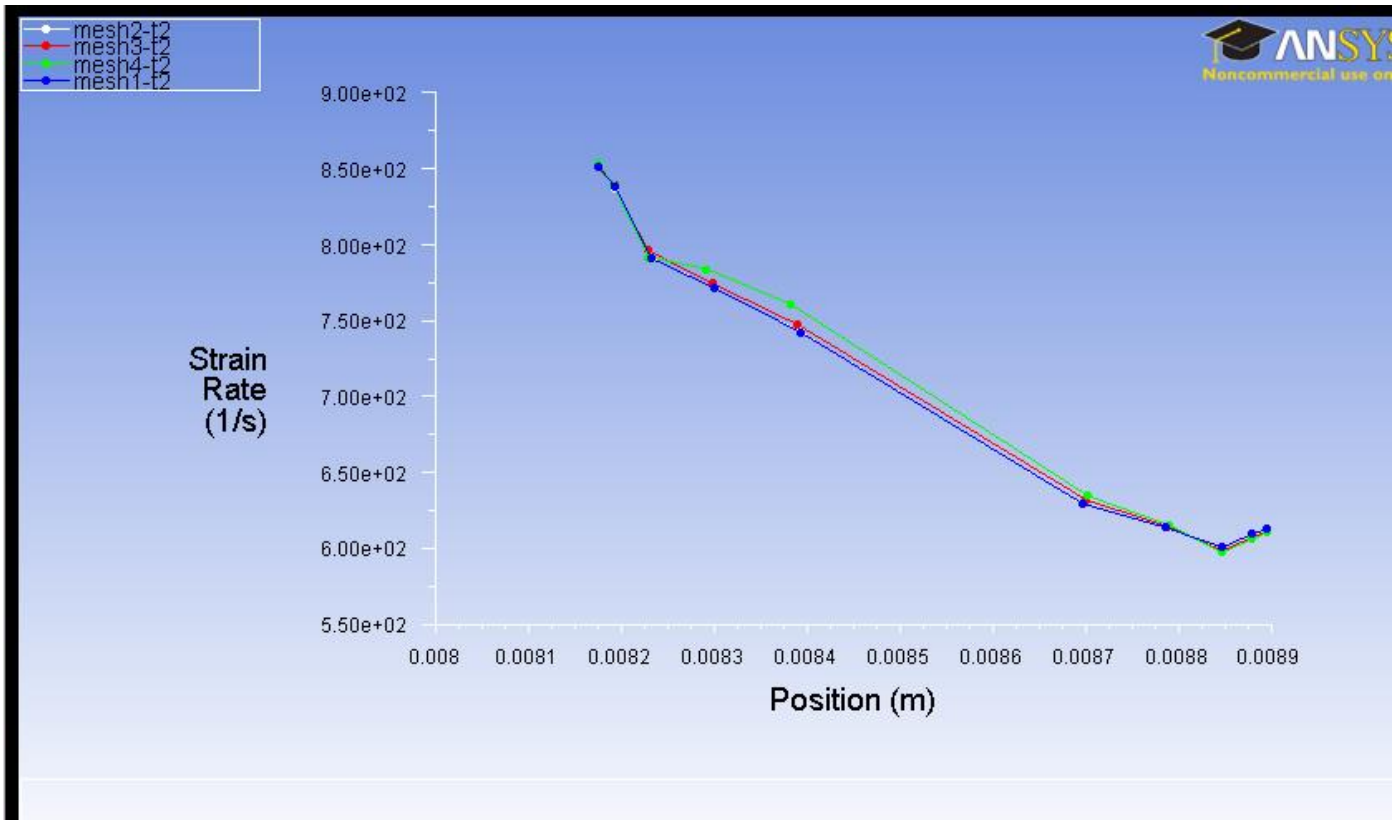

Figure 3.4.6 Strain Rate [s-1] on Transect 1

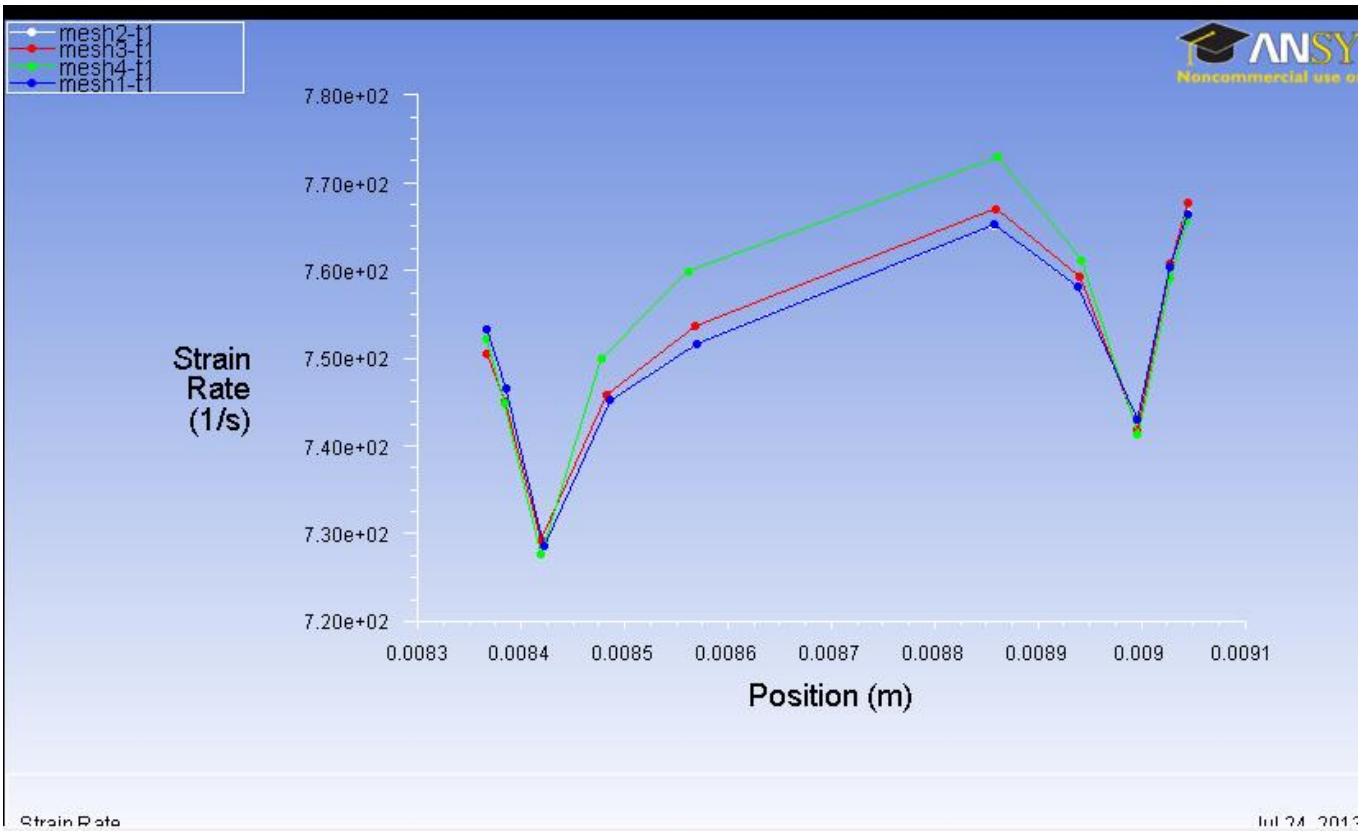

Figure 3.4.7 Strain Rate [s-1] on Transect 2

The tangential velocity had very negligible difference for the increasing mesh refinement Mass flow rate from the inlet and outlet were checked validity of Mesh 2 as shown in Figure 3.4.8

Mass Flow Rate	(kg/s)
in	0.0017204611
out	-0.0017199636
Net	4.9757068e-07

Figure 3.4.8 the mass flow difference between inlet and outlet was found to be 4.97e-6 kg/s which is an acceptable difference

It is assumed that there is a Couette flow condition inside the thin gap region (gap=0.125mm). This assumption was validated in the numerical simulation. The axial velocity profile was parabolic shown in Figure 3.4.9 at 8000 rpm. This speed is considered since hemolysis will be calculated at this speed. This speed is also selected in order to make comparison with experimental data which was taken from [32] as a reference. The tangential velocity profile was linear Figure 3.4.10. Due to much smaller axial velocity, the total velocity magnitude distribution looks similar to the tangential velocity profile Figure 3.4.11

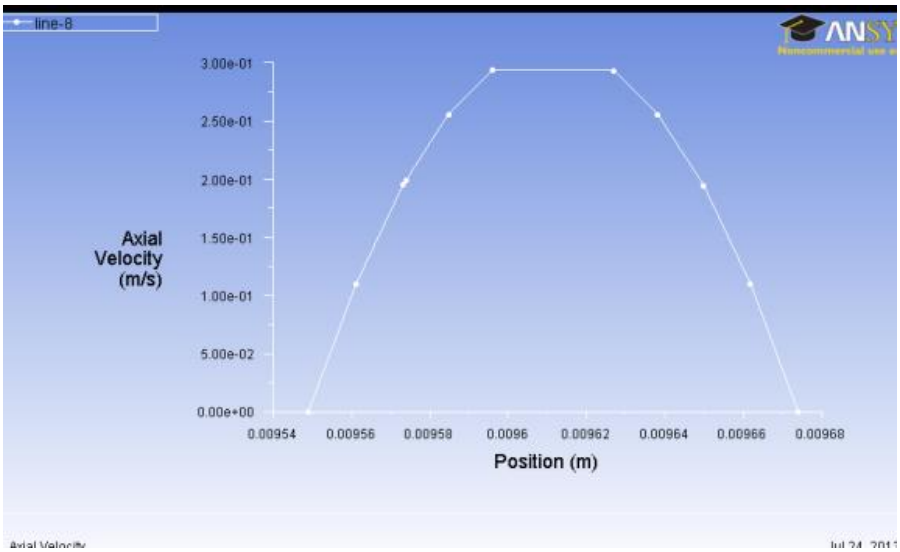

Figure 3.4.9 Axial velocity (thin gap)

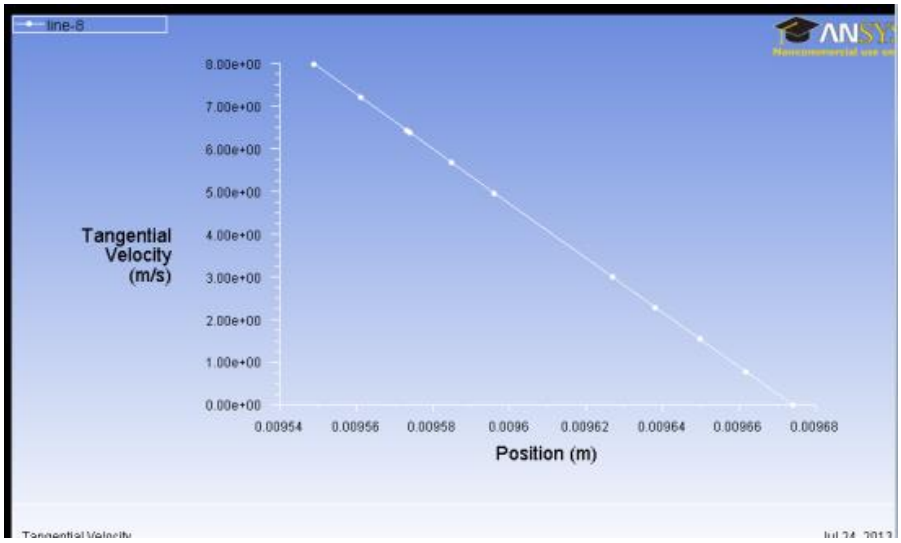

Figure 3.4.10 Tangential velocity (thin gap)

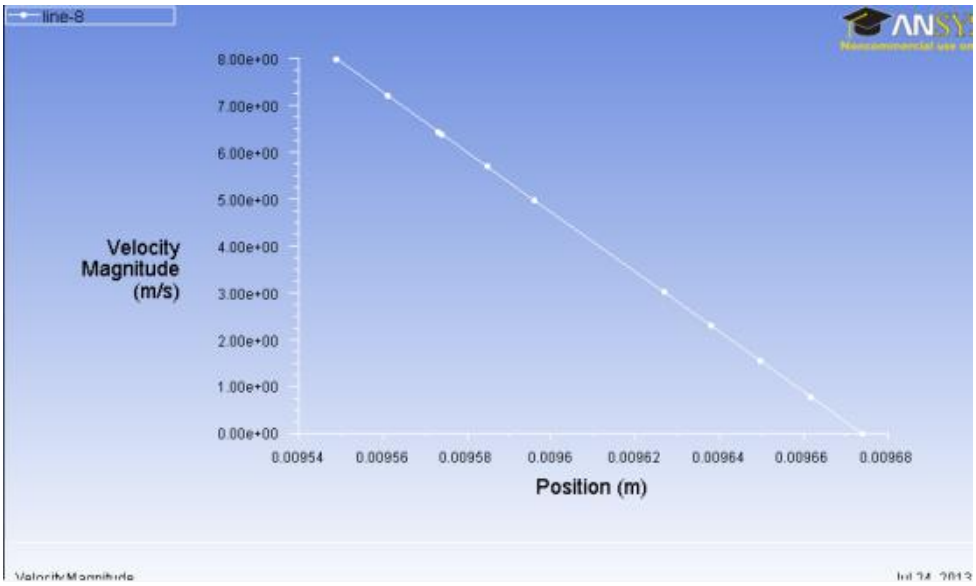

Figure 3.4.11 Total velocity (thin gap)

The axial velocity profile in the gap region up and downstream the shear gap was sinusoidal at 8000 rpm Figure 3.4.12, due to possible Taylor vortices in this region. The tangential velocity profile is nonlinear Figure 3.4.13. The gap is 1.06 mm wide. Due to much smaller axial velocity, the total velocity magnitude distribution looks similar to the tangential velocity profile Figure 3.4.14

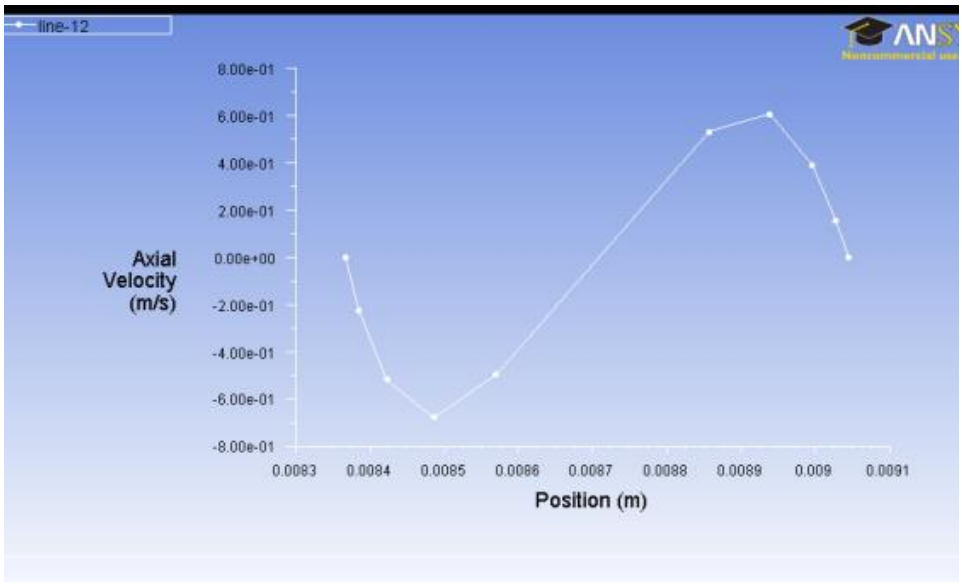

Figure 3.4.12 Axial velocity (wider gap)

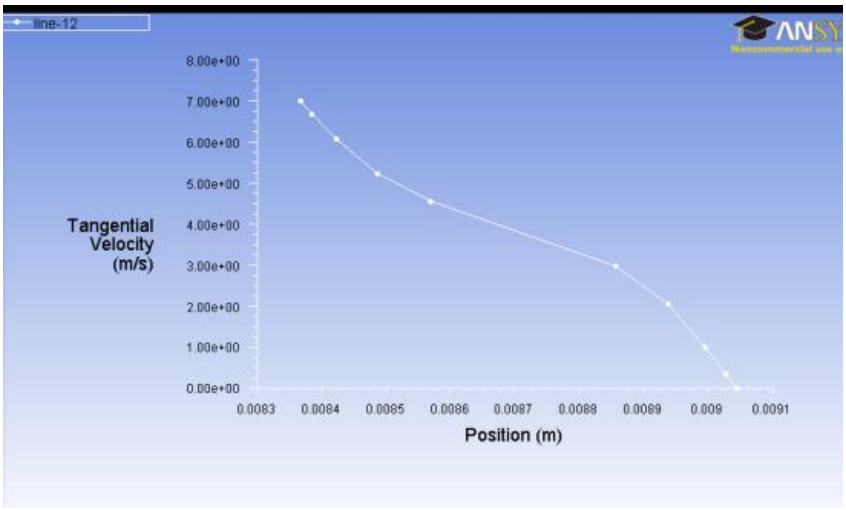

Figure 3.4.13 Tangential velocity (wider gap)

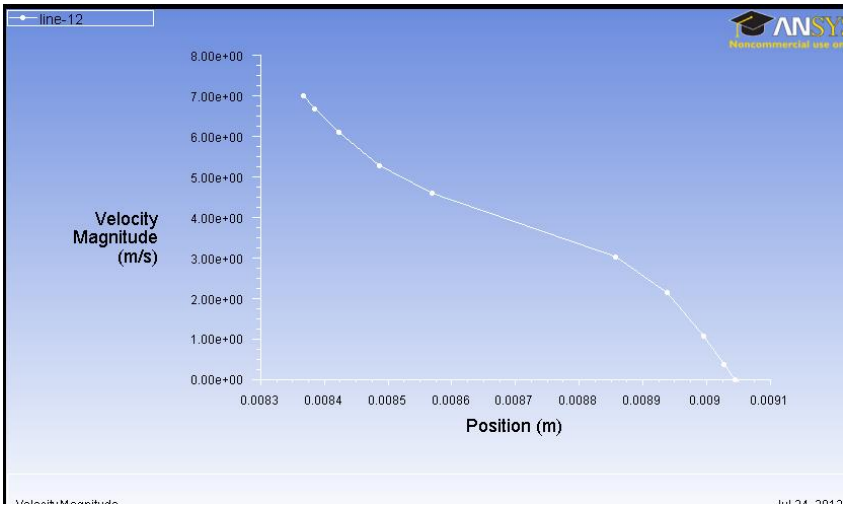

Figure 3.4.14 Total velocity (wider gap)

Though the velocity profile in the upstream and downstream region of the shear gap was sinusoidal indicating a non Couette flow, path lines successfully escaped through the outlet of the device. This can be attributed to the orthogonal quality and aspect ratio of the mesh considered.

3.4.2 Note on Orthogonal Quality and Aspect Ratio w.r.t the pathlines tracked

It was observed that more pathlines escape through the outlet for a mesh with higher orthogonality and lesser aspect ratio. Orthogonality and aspect ratio are used by Fluent to indicate the mesh quality. The orthogonal quality ranges from 0 to 1 with values closer to zero corresponding to low quality. For the mesh considered here the orthogonal quality was the highest and the aspect ratio was the lowest of all the design's tested. A detail analysis of the orthogonal quality and aspect ratio for each design and its effect on path line tracking is explained in later. Figure 3.4.15 shows the orthogonal quality and the aspect ratio for the mesh used in design 4 analyses.

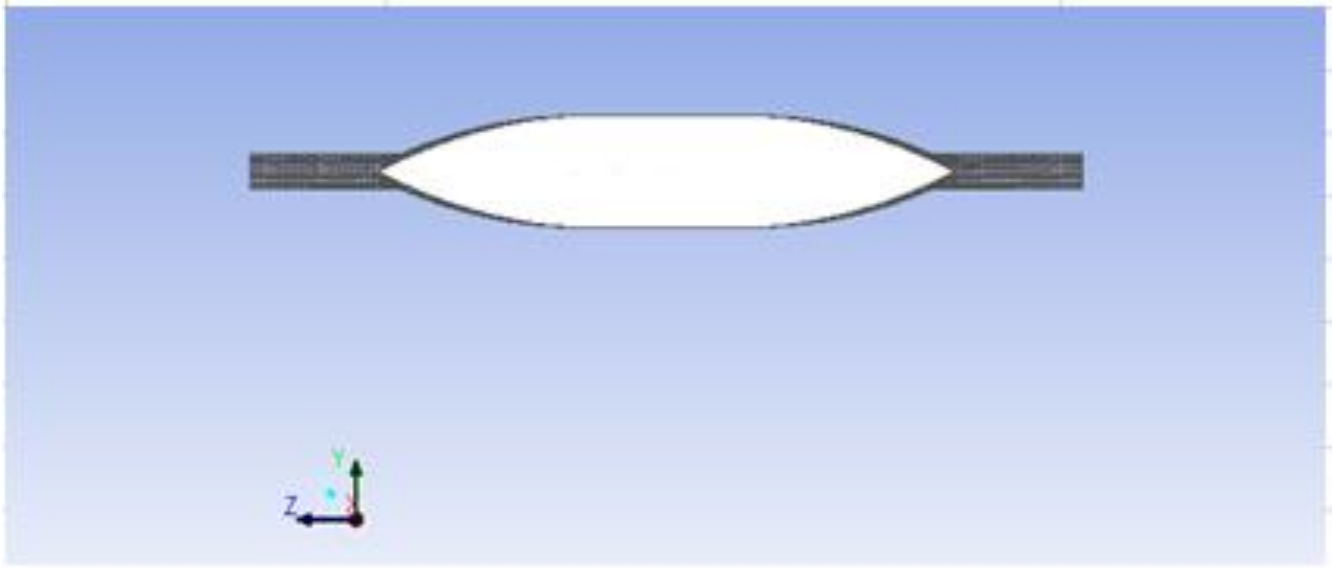


```
Mesh Quality:
 Orthogonal Quality ranges from 0 to 1, where values close to 0 correspond to low quality.
Minimum Orthogonal Quality =  4.11819e-01
Maximum Aspect Ratio =  5.82028e+01
```

Figure 3.4.15 Mesh Quality expressed in orthogonality and Aspect ratio

3.4.3 Axial Velocity and Pressure plots for design 4

Figure 3.4.16 shows the **existence of a single elongated Taylor vortex up and downstream the shear gap.** However the elongated vortex did not increase exposure time for the particles that successfully escaped through the outlet. The vortices do not increase the exposure time and this can be deduced from the exposure time calculated analytically and from simulation.

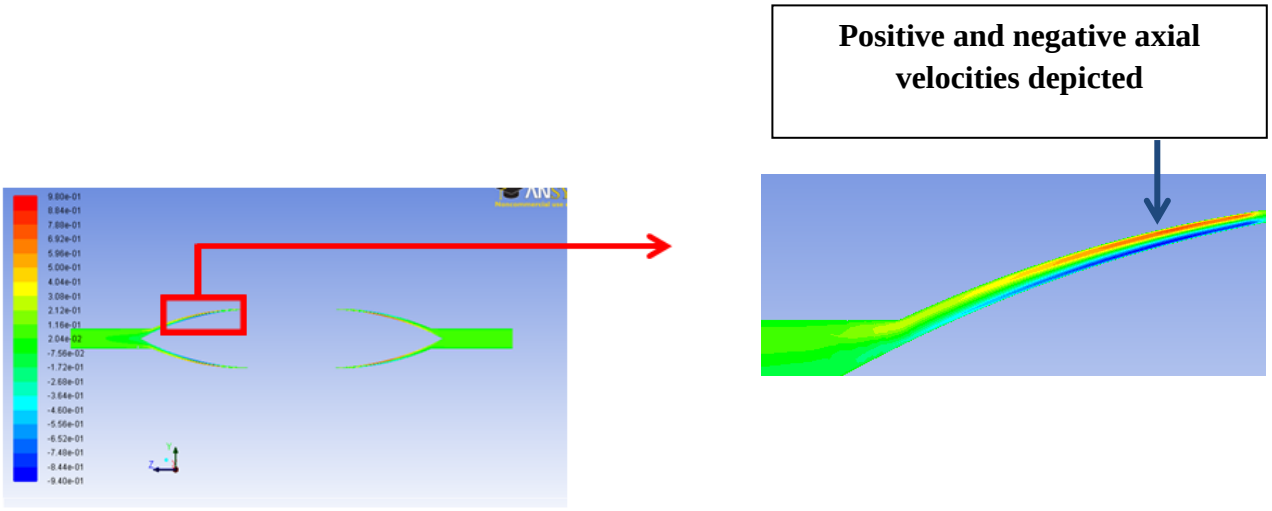

Figure 3.4.16 Axial velocity contour plot at 8000rpm.

Varying pressure gradients were observed in the **wide** gap of design 4, Figure 3.4.18. The axial velocity plot shown besides the pressure plot, Figure 3.4.17, for Design 1 at 8000 rpm shows the presence of positive and negative axial velocities in the wide gap. The pressure variation in the **thin** gap/shear gap for the Design 1 however has uniform pressure distribution

and uniform axial velocity. **The positive and negative axial velocities in the wide gap, could then, be attributed to the pressure gradients in the wide gap**. A modified design of the gap upstream and downstream shown in Figure 3.4.20, Figure 3.4.19shows the pressure plots and axial velocity plots at 8000 rpm and 100 ml/min.

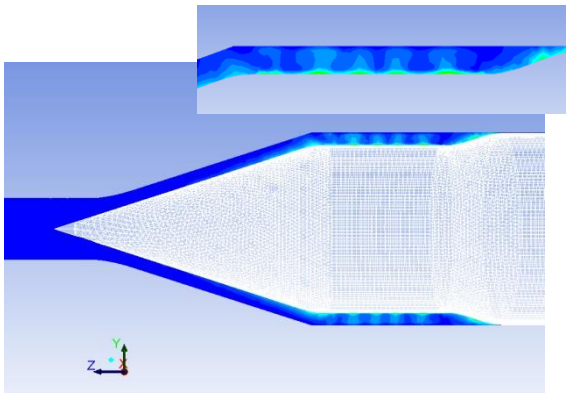

Figure 3.4.18 Pressure contour plot Design 1

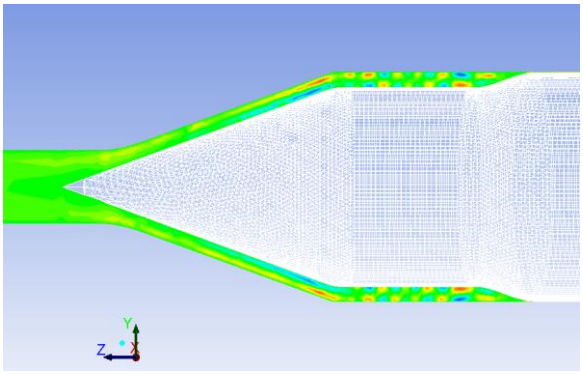

Figure 3.4.17 Axial velocity contour plot Design 1

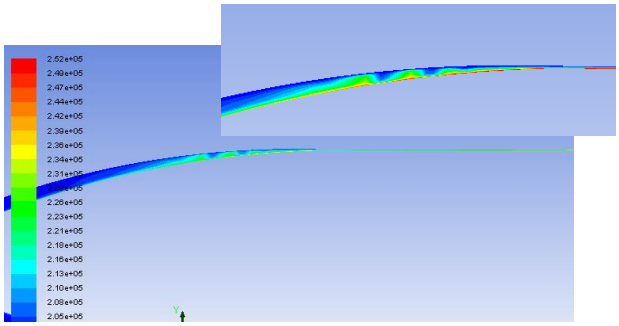

Figure 3.4.20 Pressure contour plot Design 4

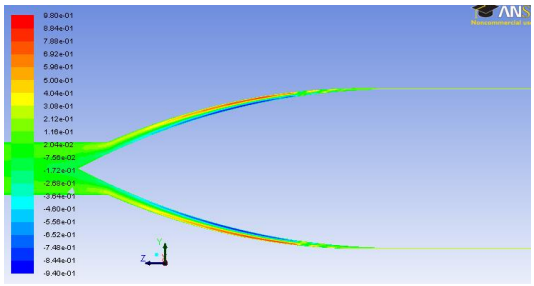

Figure 3.4.19 Axial velocity contour plot Design 4

By modifying the upstream and the downstream region of the shear gap as shown in Figure 3.4.20 as compared to the gap shape upstream and downstream of the shear gap for design 1, as shown in the Figure 3.4.18, the pressure gradients can be reduced and a smooth pressure transition can be achieved. The pressure gradients decrease with decreasing axial velocity and vice versa. The axial velocity contour plot shown beside the Design 3 shows one elongated vortex Figure 3.4.19 as compared to a number of vortices for Design 1, Figure 3.4.17. The flow in the thin gap region is a Poiseulle flow and no vortices are generated here. Hence the time spent by particles in this thin gap region should not be affected. However, a single elongated Taylor vortex forms upstream and downstream the thin gap region. To verify if the particles get trapped in these vortices and if it affects the residence time of the particles, shear stress *vs.* residence time and shear stress *vs.* axial position plots for a single particle were plotted at 8000 rpm and 100 ml/min and 200 ml/min as shown in Figure 3.4.21. The particle was traced from the inlet to the outlet. There are no plateaus in Figure 3.4.21 and Figure 3.4.23, indicating particle being trapped in the vortex upstream and downstream the shear gap region. The small plateau as indicated in the Figure 3.4.21, Figure 3.4.23 is the shear gap region in which the particle is subjected to a high shear stress. On the same lines the discussion can be extended to multiple particles that escape the outlet, 48/72 particles in 100ml/min flow rate case and 55/72 in 200ml/min flow rate case. This analysis of the other particle's escaping through the outlet is not carried out here. It can be assumed that the other particles will not be trapped in the elongated vortex upstream and downstream the shear gap region like the single particle tested here. The

spikes in the shear stress plots are a result of the high shear stress spots and will be discussed in the next section of shear stress field. The plots of damage distribution along the path lines Figure 3.4.26, Figure 3.4.25 show the damage distribution over the length of the device. It can be seen that these elongated vortices do not affect the blood damage distribution.

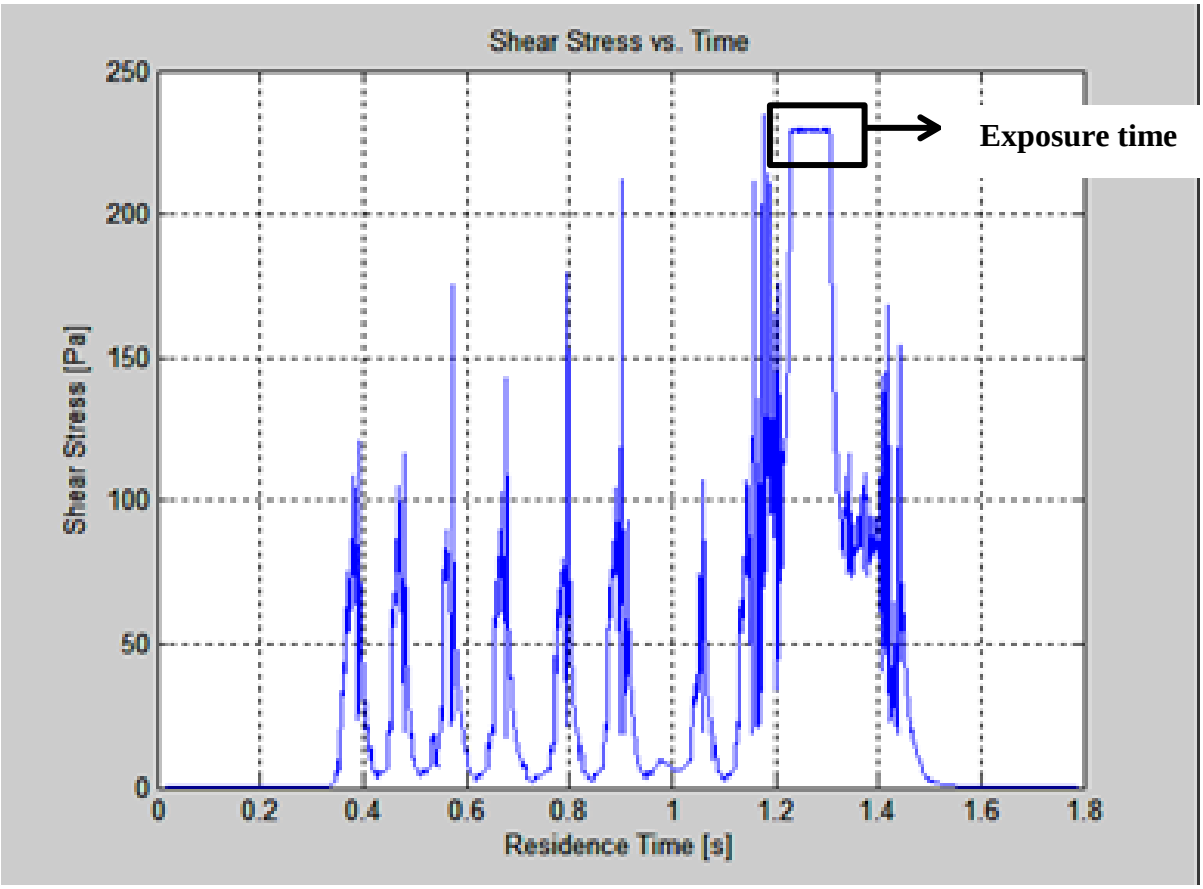

Figure 3.4.21 Shear stress *vs.* Residence time at 100 ml/min

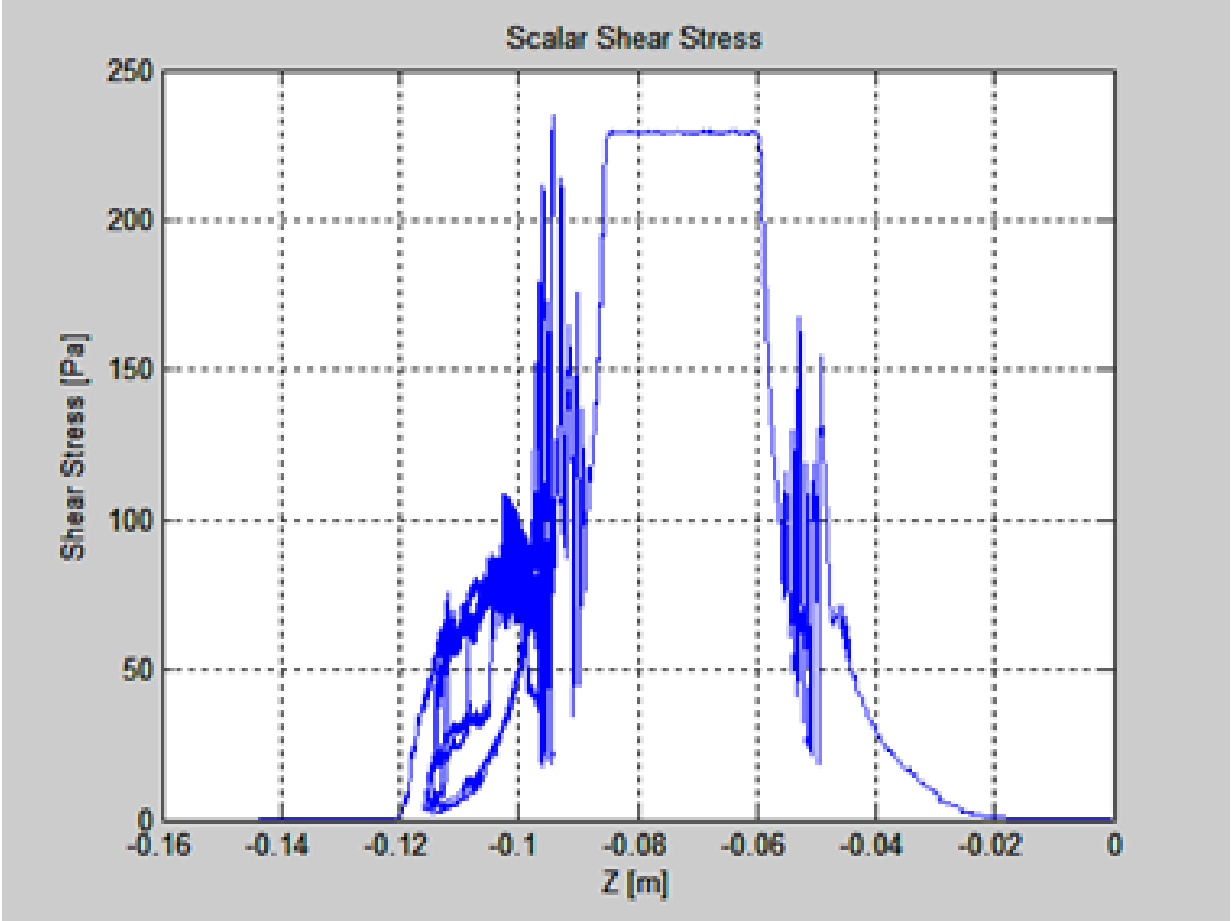

Figure 3.4.22 Shear stress *vs.* Axial position at 200 ml/min

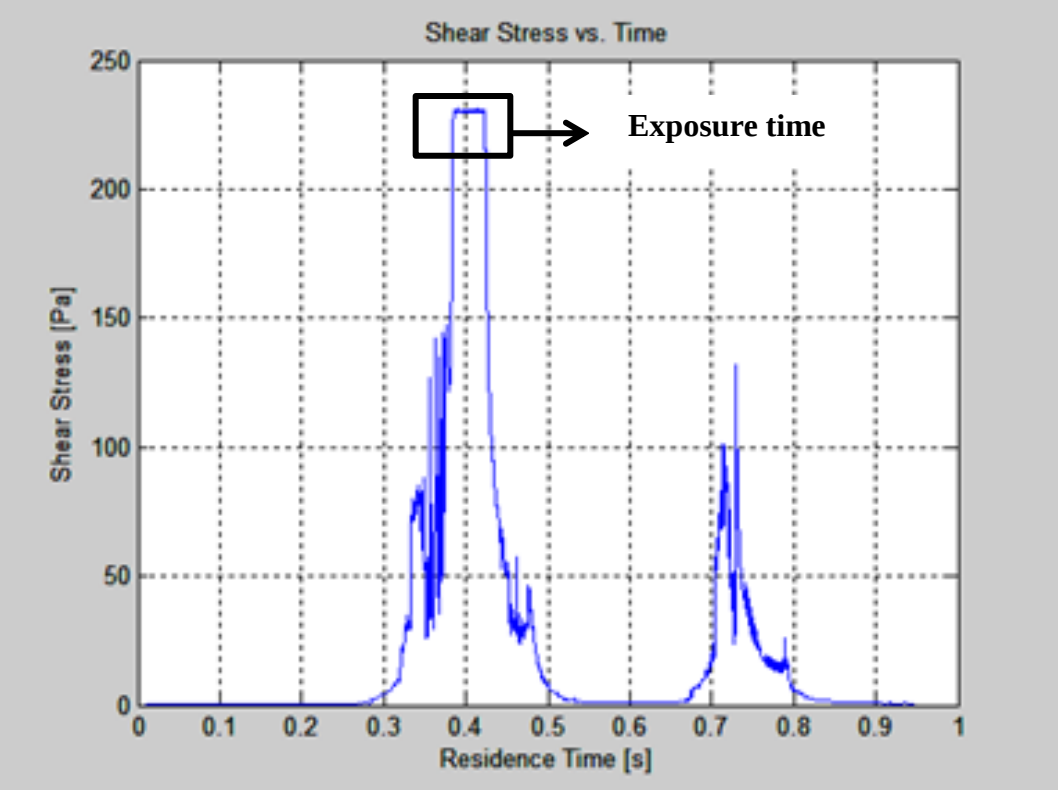

Figure 3.4.23 Shear stress *vs* Residence time at 200 ml/min

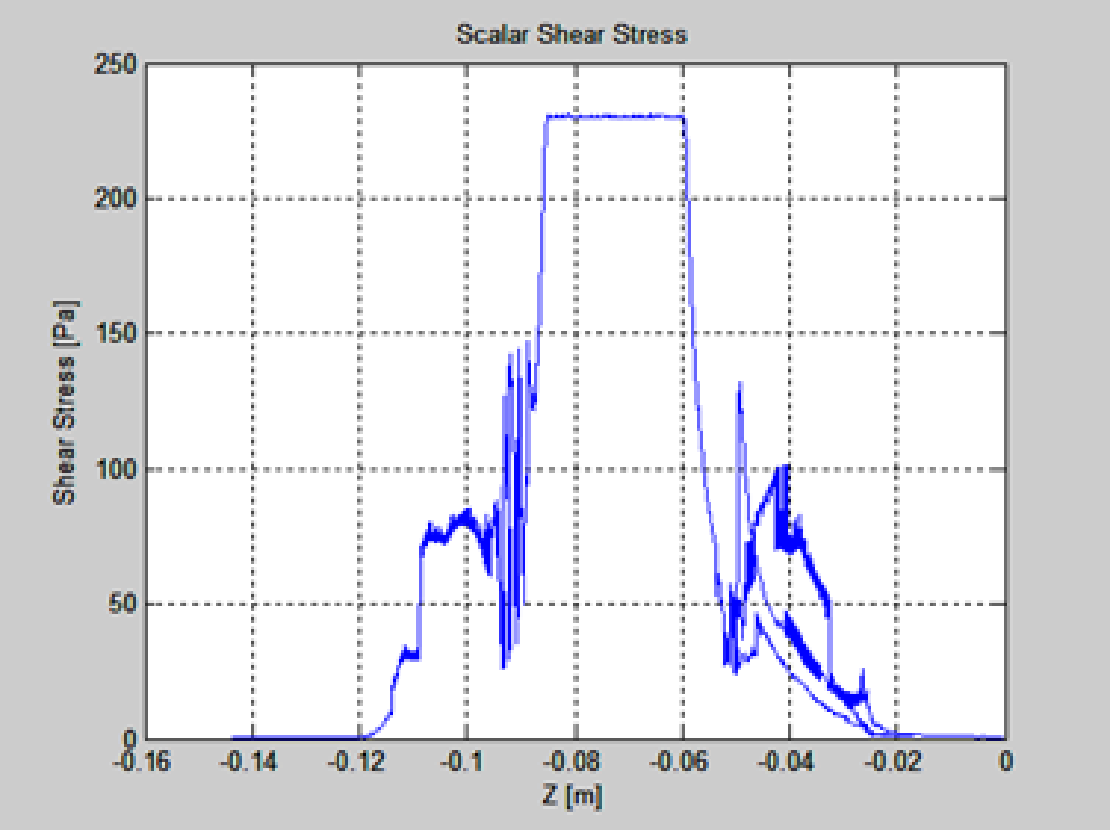

Figure 3.4.24 Shear stress *vs* Axial position at 200 ml/min

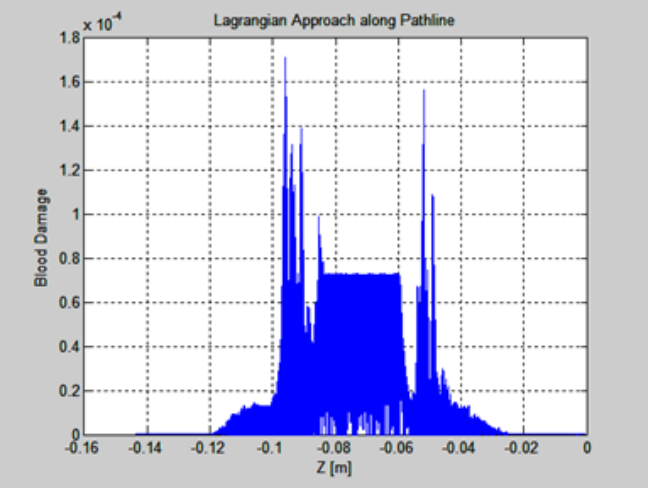

Figure 3.4.25 HI(%) distribution at 100 ml/min at 8000rpm

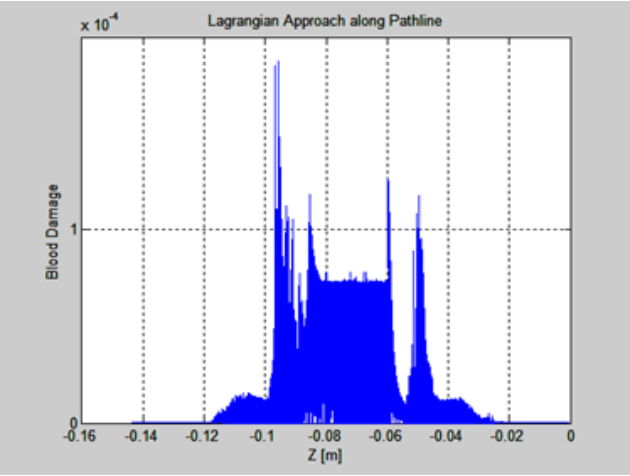

Figure 3.4.26 HI(%) distribution at 200ml/min at 8000rpm

3.4.4 Shear stress field

The uniformity of the shear stress field in the gap region of the design 4 was assessed by examining shear stress contour plots along the path lines. The CFD- predicted mean scalar shear stress in the gap region is 230 Pa, as the flow rate is increased from 50ml/min to 200 ml/min.

Shear stress along the path lines are shown in Figure 3.4.27A. The shear stress is higher in the gap region than upstream or downstream; however there are spikes in the shear stress plots upstream and downstream regions because of the presence of high shear spots. Small regions of high shear stress were found upstream and downstream of the shear gap. The Figure 3.4.27 D shows small regions of high shear stress upstream of the gap at 100 ml/min and 8000 rpm condition. The shear stress in these spots was higher (up to 292 Pa). However as their volumes are localized and extremely small, their effect on the total blood damage can be considered to be small. At 100 ml/min the particle spent 1.3 msec within these high shear spots compared to 58 msec in the gap.

A.

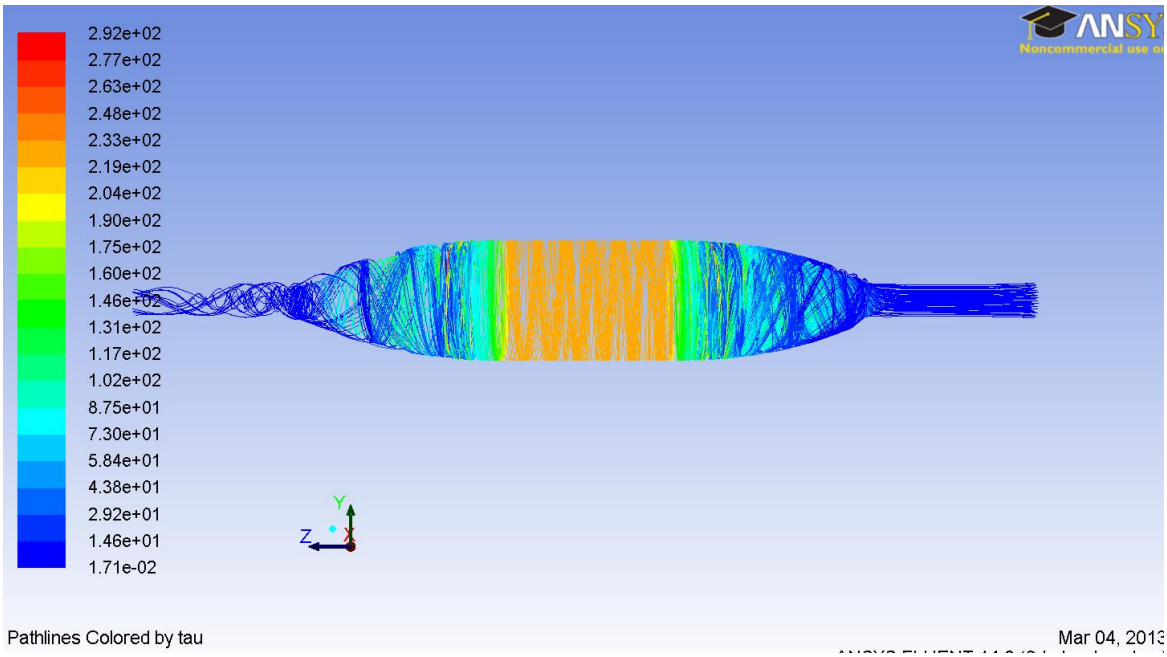
2.92e+02
2.77e+02
2.63e+02
2.48e+02
2.33e+02
2.19e+02
2.04e+02
1.90e+02
1.75e+02
1.60e+02
1.46e+02
1.31e+02
1.17e+02
1.02e+02
8.75e+01
7.30e+01
5.84e+01
4.38e+01
2.92e+01
1.46e+01
1.71e-02
Y
Z
X
Pathlines Colored by tau
Mar 04, 2013

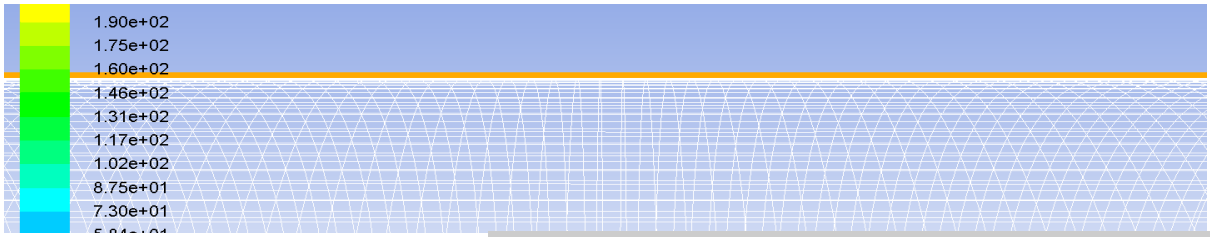
1.90e+02
1.75e+02
1.60e+02
1.46e+02
1.31e+02
1.17e+02
1.02e+02
8.75e+01
7.30e+01

B.

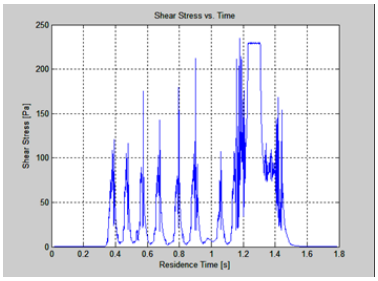
Shear Stress vs. Time
Shear Stress [Pa]
Residence Time [s]

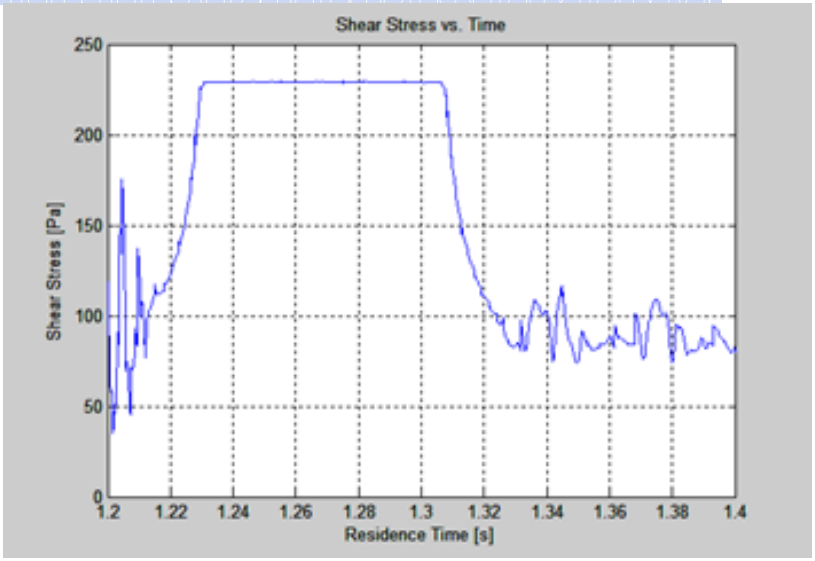
Shear Stress vs. Time
250
200
150
100
50
0
Shear Stress [Pa]
1.2
1.22
1.24
1.26
1.28
1.3
1.32
1.34
1.36
1.38
1.4
Residence Time [s]

C.

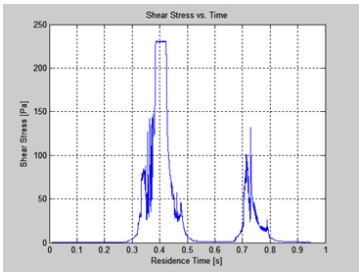

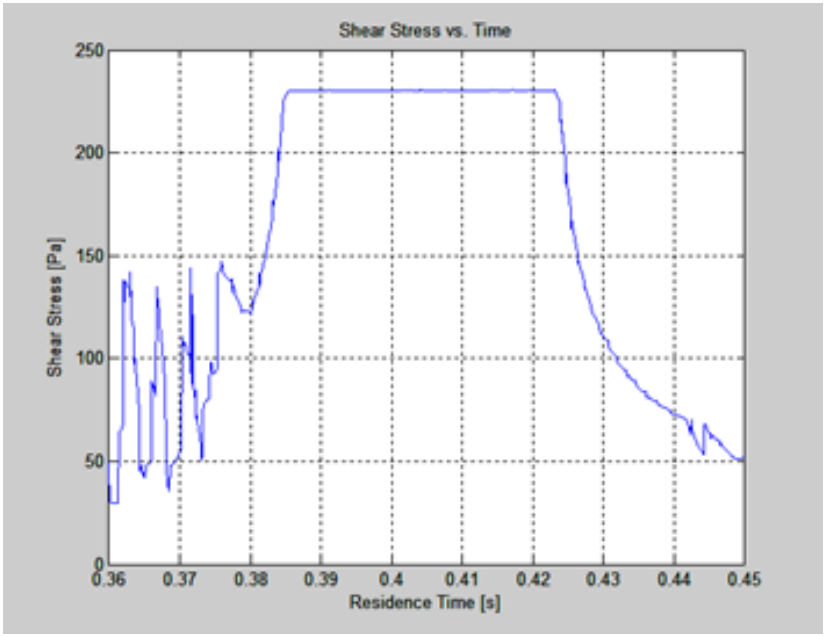

D.

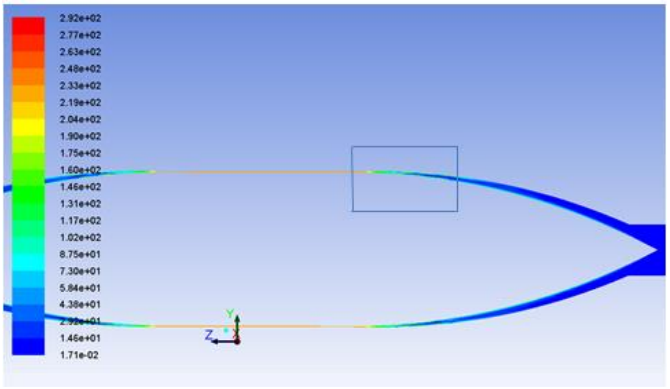

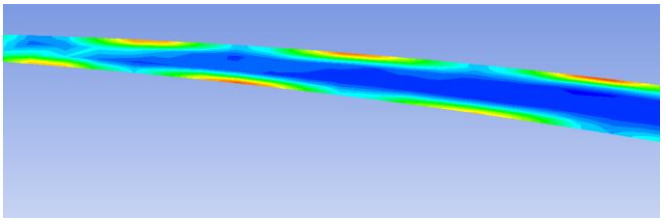

Figure 3.4.27 (A)Illustrative path lines in the Curved gap colored by scalar shear stress and enlargement showing scalar shear stress contour in the gap region for rotational speed of 8000 rpm and flow rate of 100 ml/min ,with a maximum scalar shear of 230 Pa in the gap region (B) Shear stress *versus* residence time plot for a single particle at rotational speed of 8000 rpm and flow rate 100 m l/min and (C) 200 m l/min. The gap exposure times at these conditions are 0.08 sec and 0.04 sec respectively for 100 ml/min and 200 ml/min. Note that the path line plots on the left demonstrate

residence time for entire flow time and the plots on the left show a portion of the entire residence time during which shear stress is the highest. 48 particles were traced out of 72 (66.66%) at 100 m l/min and 55 out of 72 at 200 ml/min (76.38%). The figure (D) shows small regions of high shear stress upstream of the gap at 100 m l/min and 8000 rpm condition.

The difference in the analytical and simulation, shear stress and exposure time is summarized in the below Table 3.4.3

Table 3.4.3 Analytical and Numerical results for shear stress and exposure time at 8000 rpm and 100 ml/min and 200 ml/min

	Shear Stress-τ (Pa)	Exposure time - t_exp(s) 100ml/min	Exposure time - t_exp(s) 200ml/min
Simulation	229-230	0.08	0.048
Analytical	240	0.11	0.058

3.4.5 Incomplete Particles _Graphical Analysis

An attempt to show the final location of the particles not tracked in through the device was done. The graphs below show the x, y, z position of a single incomplete particle as compared to a particle that escapes the outlet. For the case considered here 55 particles escaped out of 72 traced for 200 ml/min at 8000 rpm. All the particles that did not escape successfully seemed to be trapped at the outer wall. The Tec-plot figures show in detail the particles trapped on the outer walls.

Table 3.4.4 gives the x, y and z positions for all the particles trapped for a sample case of 8000 rpm and 20 ml/min test case. Out of the 17 particles that did not escape the outlet only six of them were plotted in the graphical analysis and Tec-plot. It is seen from the Tec-plot graphs that all the particles are trapped on the outer wall or the housing wall.

Trapped particle X, Y, Z Positions using Tec-plot

Particle #	x	y	z
5	-0.00317	0.008292	-0.04631
13	-0.00806	0.004768	-0.05041
18	0.00898	0.00363	-0.08847
17	-0.00176	0.002627	-0.02539
23	-0.00603	0.006681	-0.0976
29	0.000809	-0.00966	-0.08762
30	-0.00376	-0.00854	-0.09474
43	-0.00059	-0.00312	-0.02538
46	-0.0058	0.006954	-0.09722
47	-0.00024	0.003121	-0.02295
54	0.0066694	-0.00681	-0.06945
55	0.002692	0.001675	-0.02528
56	-0.00245	-0.00367	-0.11518
62	0.004996	-0.00597	-0.04448
66	-0.00351	0.009028	-0.08607
68	-0.0043	-0.00119	-0.1152
69	-0.00425	0.008688	-0.08512

Table 3.4.4 x, y and z positions of all the trapped particles

3.4.6 Graphic Analysis procedure and details.

The particles x, y and z position is exported from Fluent with the X axis data being the path length. Once this data is stored in a .txt file extension it is then read in an excel sheet. . Of all the trapped particles only the first six particles were used for plotting graphs in excel. First, graphs of two particles one escaping the outlet and one not escaping were plotted with respect to their x, y and z positions vs. path length. After that the rest of the first six particles were plotted. In this case for the excel sheet could only read the first 46 particles. The rest of the particles were then exported separately to the excel sheet. The z position of the particle vs. the path length is the best way to find out if the particle escapes the outlet or not. This is done by plotting the z position of the particle along the x axis and the path length on the y axis. As seen in Figure 3.4.28 the particles are released from the inlet which is at z = -0.144 mm. The particle 1 exits the outlet which is at z= 0 mm. The particle 5 however is trapped in between and odes not reach the outlet at z=0 mm. The particle 5 gets trapped between 0.8 m and 1.0 m on the path length.

The x and y positions graphs also show how the trapped particle position varies with respect to the path length as shown in Figure 3.4.29, Figure 3.4.30.

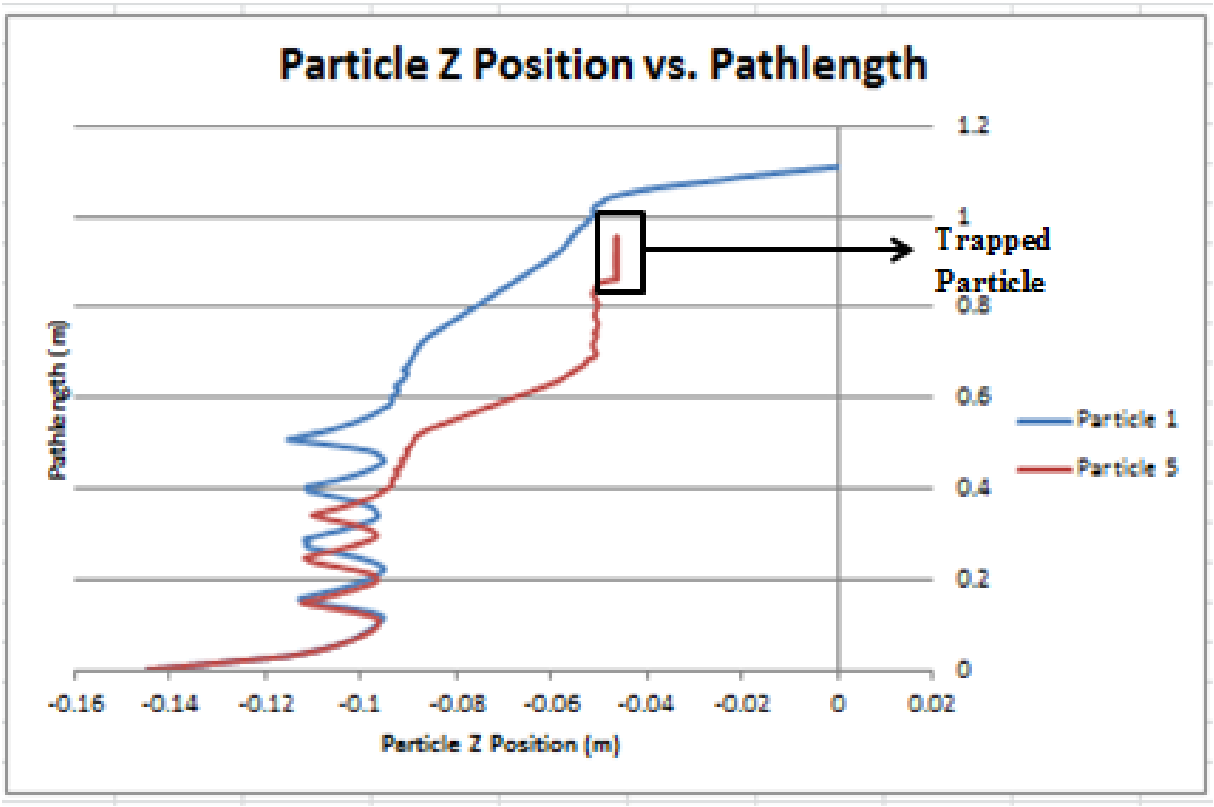

Figure 3.4.28 Z Graphical position of particle 5 which is trapped as compared to a particle 1 that escapes the outlet. It is seen that particle 1reaches the zero position on the Y axis or path length denoting that the particle has escaped

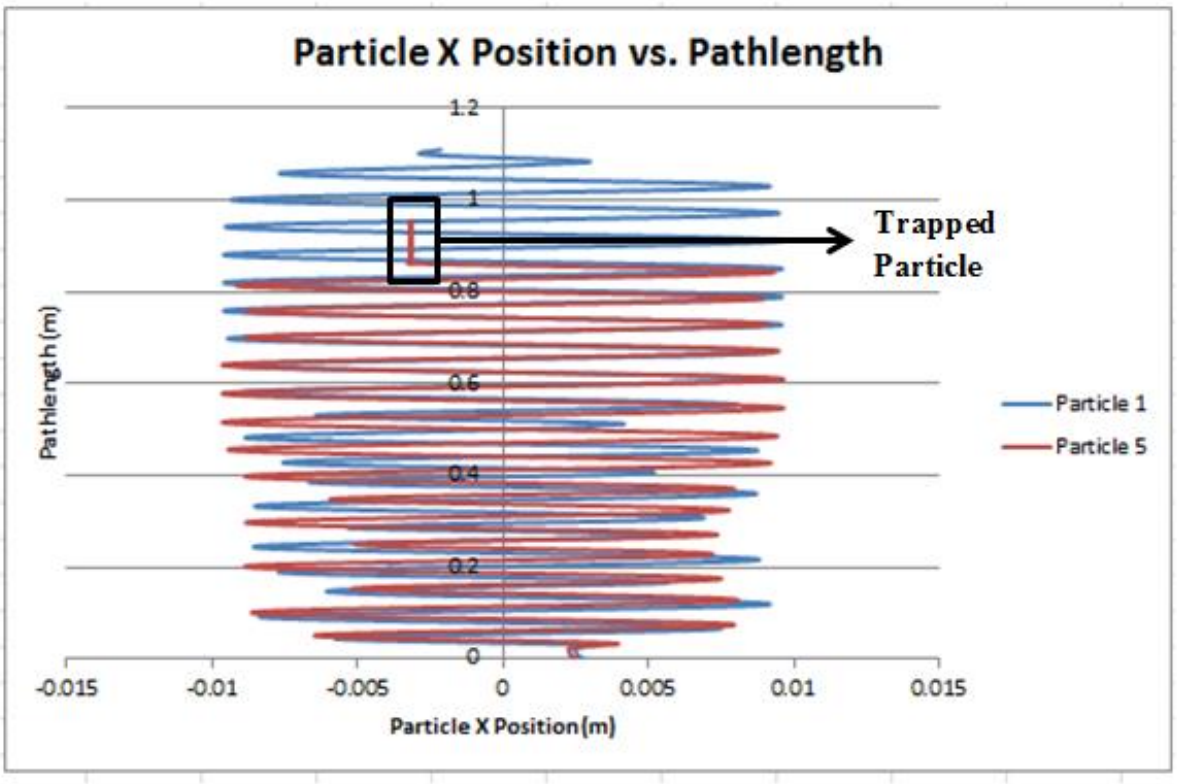

Figure 3.4.29 Graphical X position of particle 5 which is trapped as compared to particle 1 that escapes the outlet. Particle 5 can be seen trapped between 0.8m and 1.0 m on the path length as denoted by a constant line

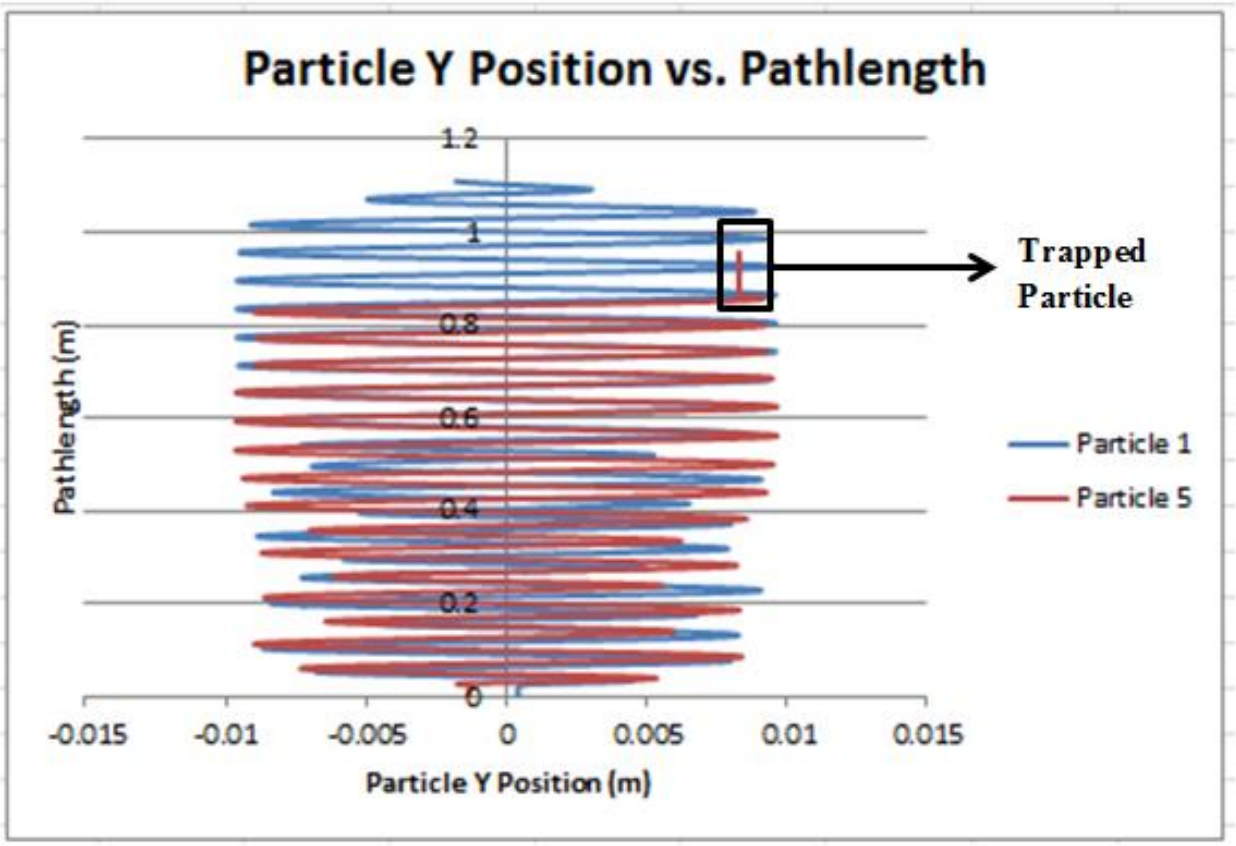

Figure 3.4.30 Graphical Y position of particle 5 which is trapped as compared to particle 1 that escapes the outlet. Particle 5 can be seen trapped between 0.8m and 1.0 m on the path length

Figure 3.4.31, Figure 3.4.32, Figure 3.4.33 show the graphs for particle position vs. the path length for multiple particles.

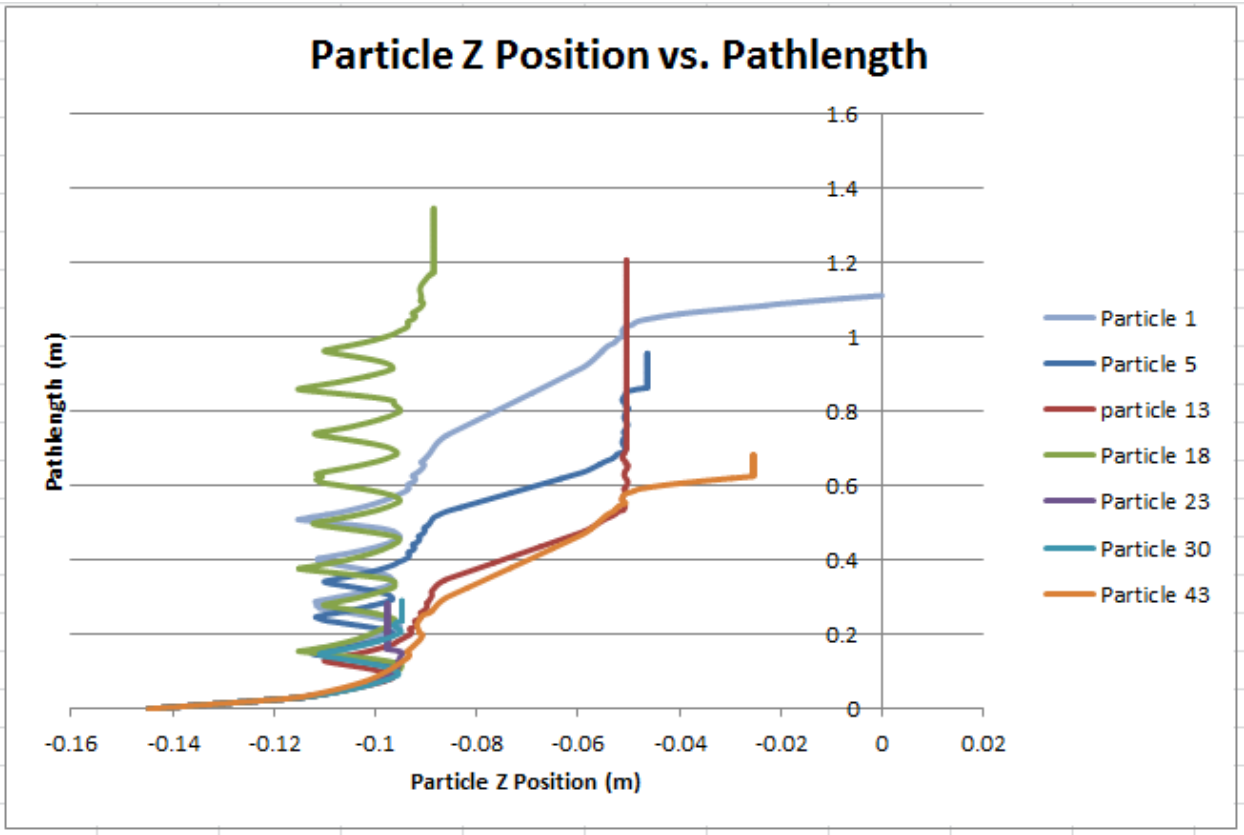

Figure 3.4.31 Z Position of the first 6 particles not escaping the outlet as compared to the particle 1 that escapes the outlet.

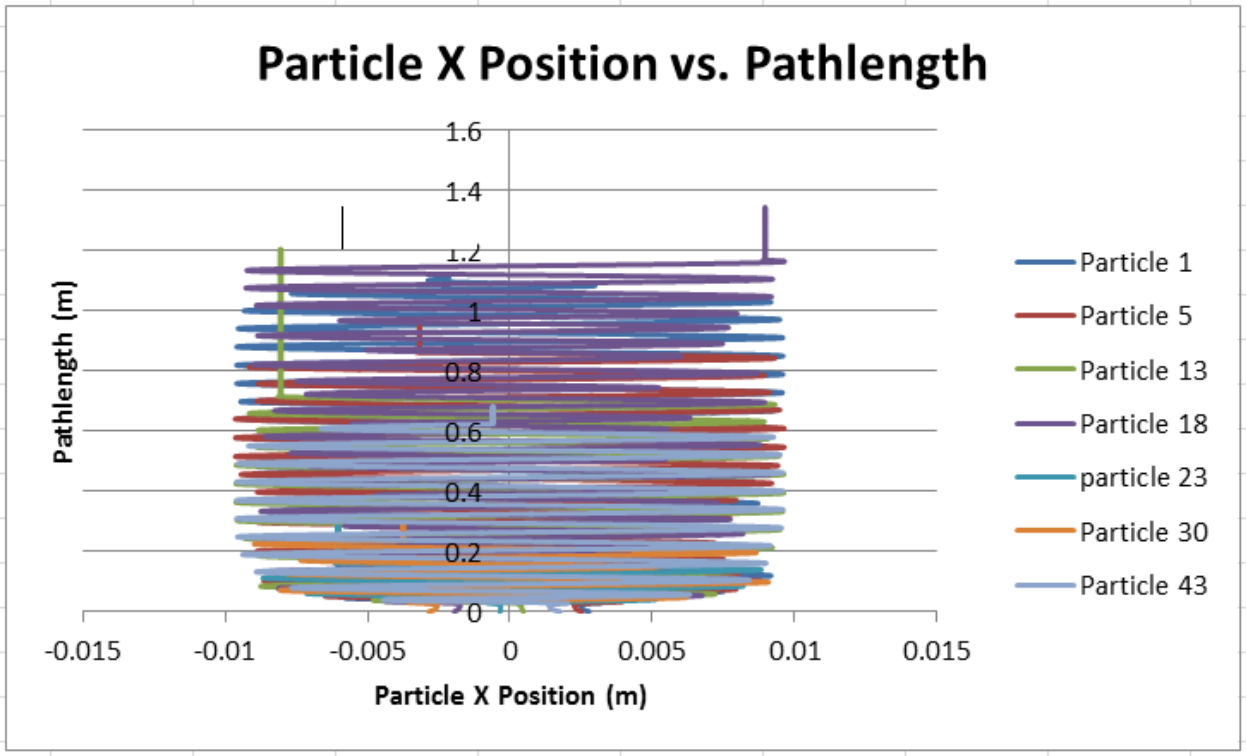

Figure 3.4.32 X Position of the first 6 particles not escaping the outlet as compared to the particle 1 that escapes the outlet.

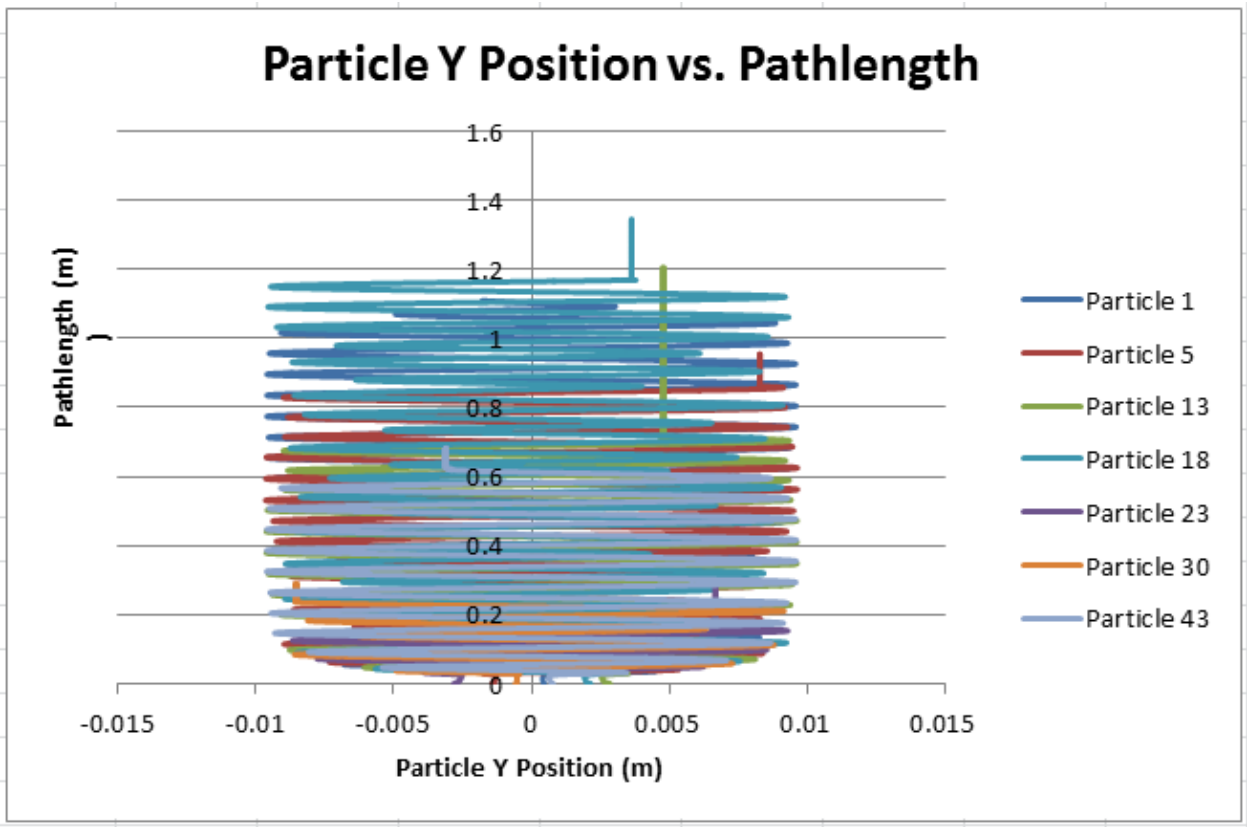

Figure 3.4.33 YPosition of first 6 particles not escaping the outlet as compared to the particle 1 that escapes the outlet.

3.4.7 Tec Plot Graphs for trapped particles

Figure 3.4.34 shows all the particles trapped for a test case of 8000 rpm and 200 ml/min the x, y, z positions for which have been mentioned in Table 3.4.4.

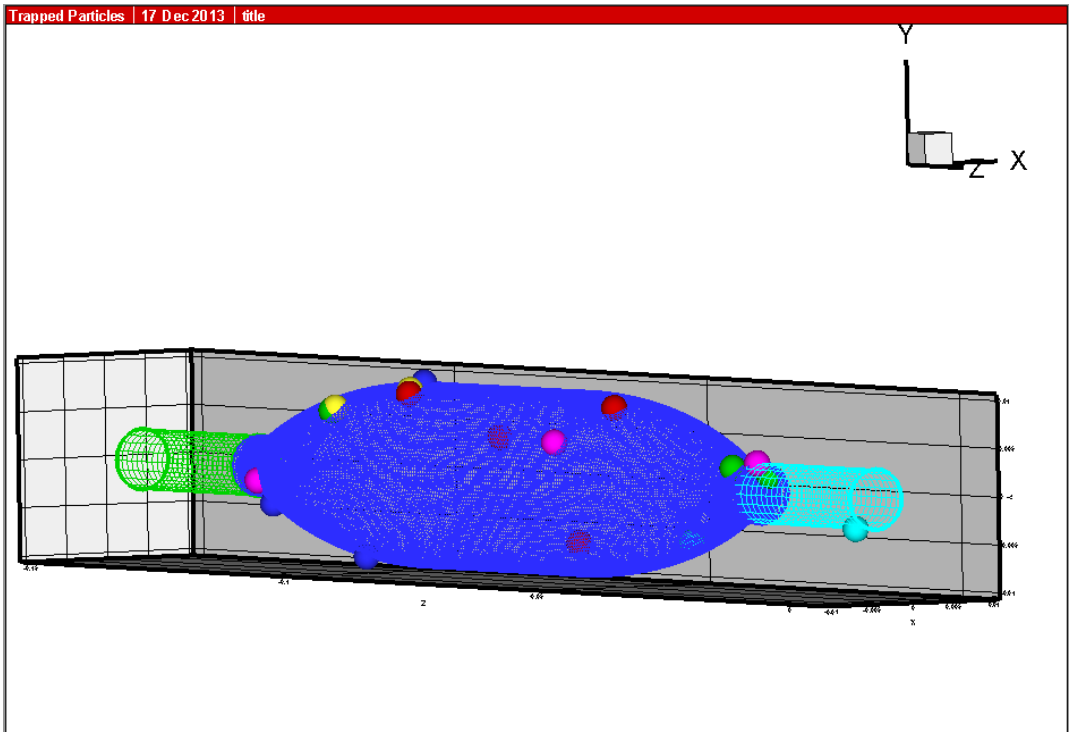

Figure 3.4.34 All the 17 particles trapped on the outside wall

Figure 3.4.35 to Figure 3.4.40 show the plots for only 6 particles out of the total 17 trapped particle. It can be seen that all the particles are trapped on the outer wall of the Mag-lev shearing device.

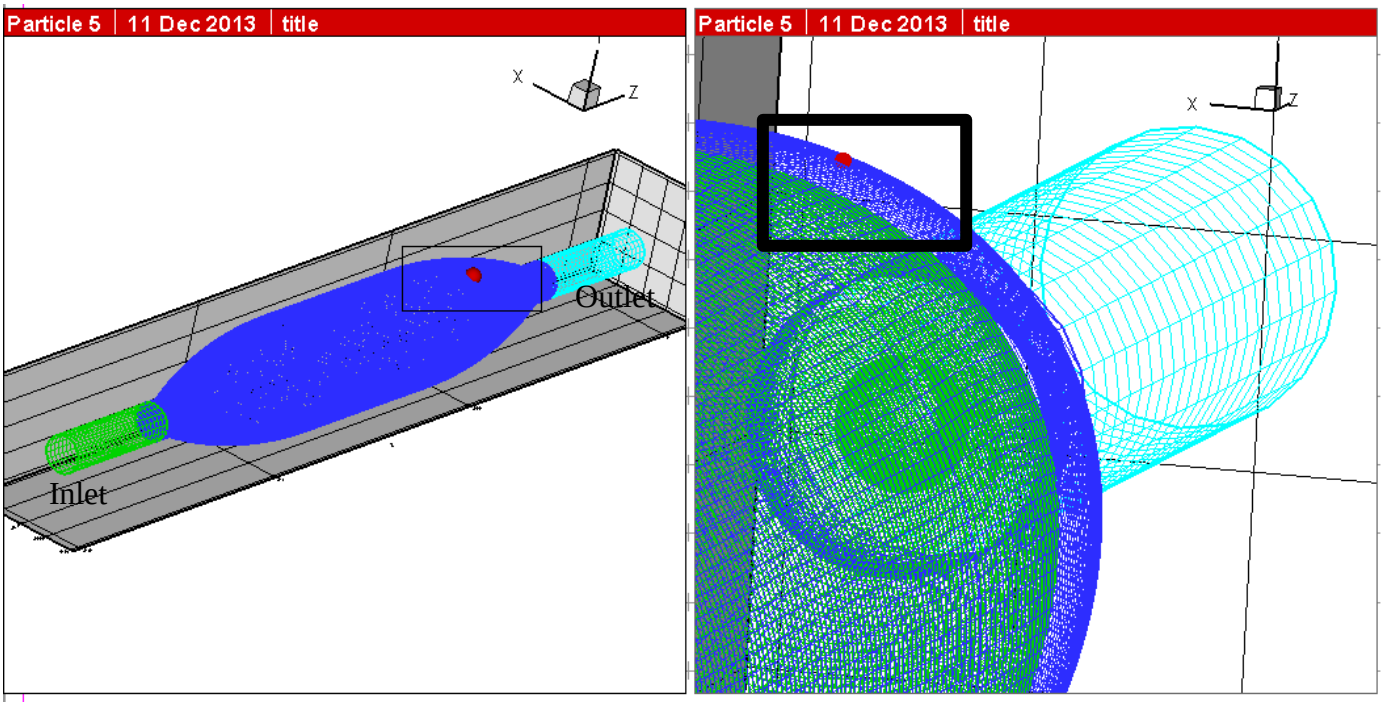

Figure 3.4.35 Particle 5 trapped near the outer wall.

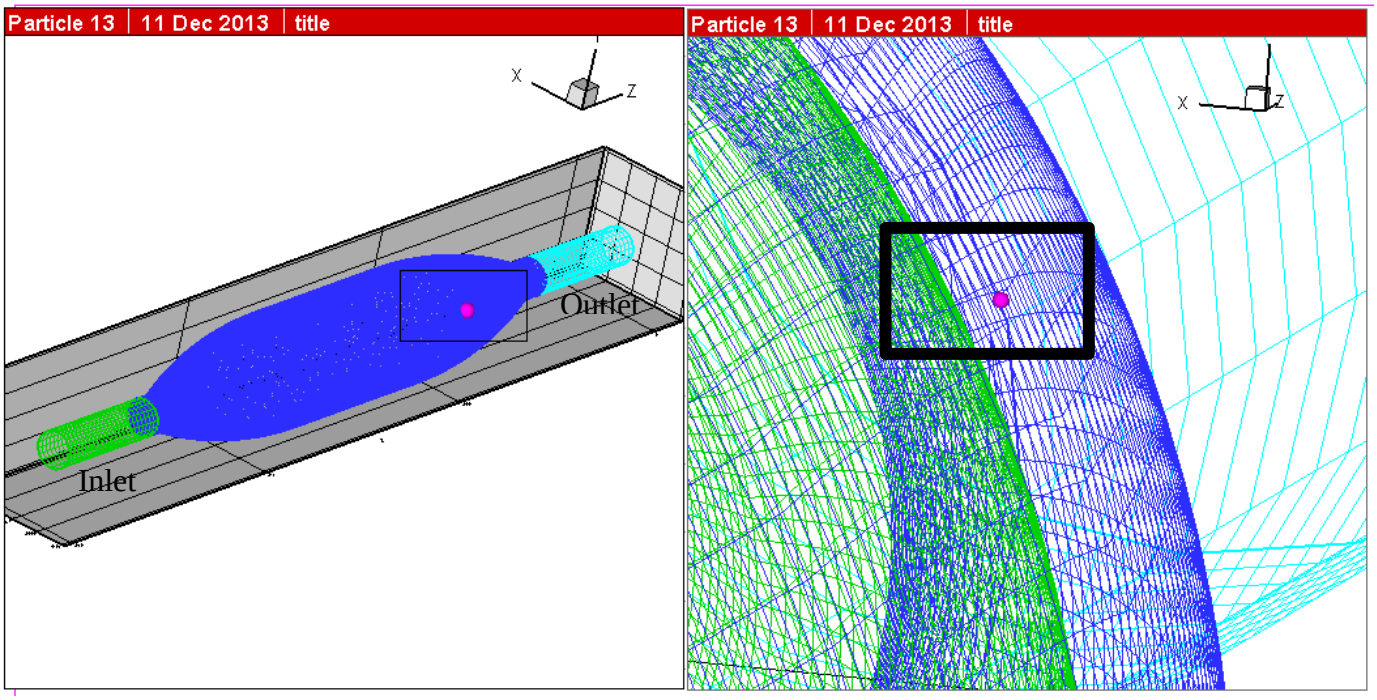

Figure 3.4.36 Particle 13 trapped near the outer wall.

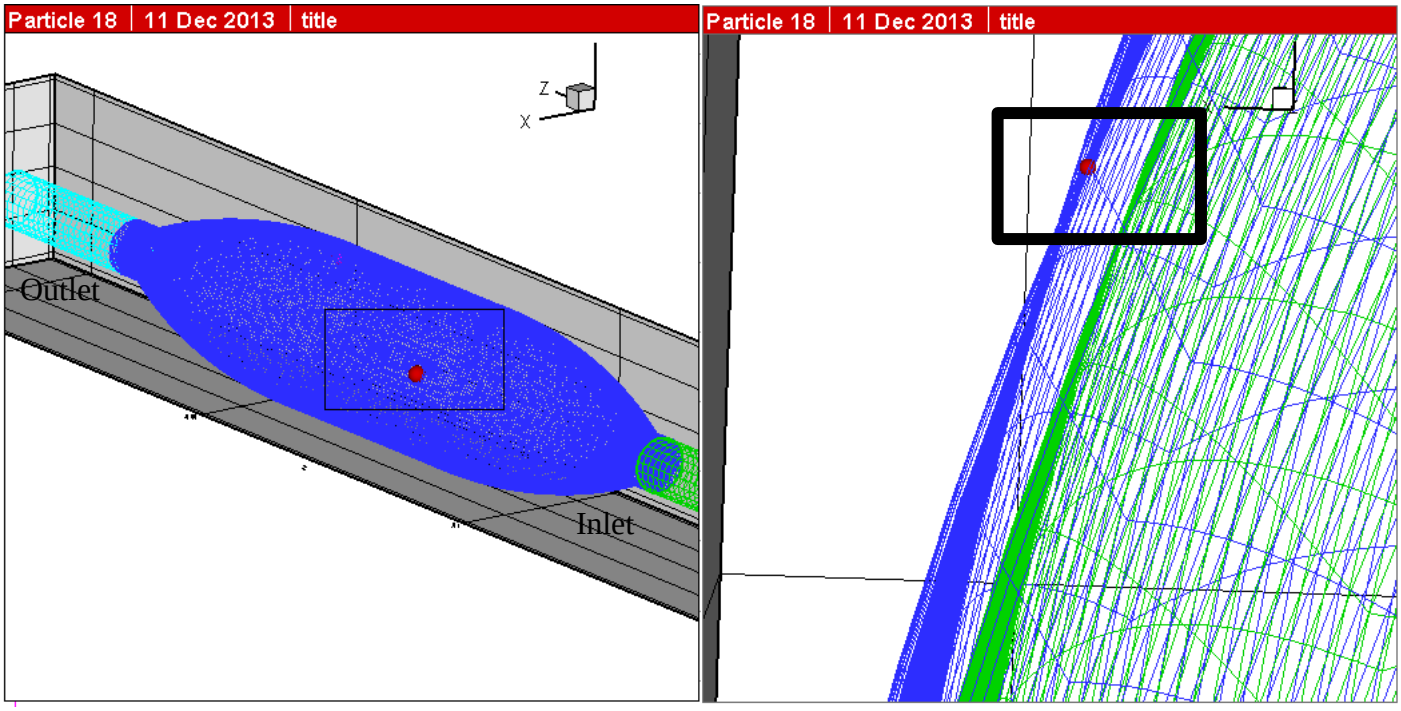

Figure 3.4.37 Particle 18 trapped near the outer wall.

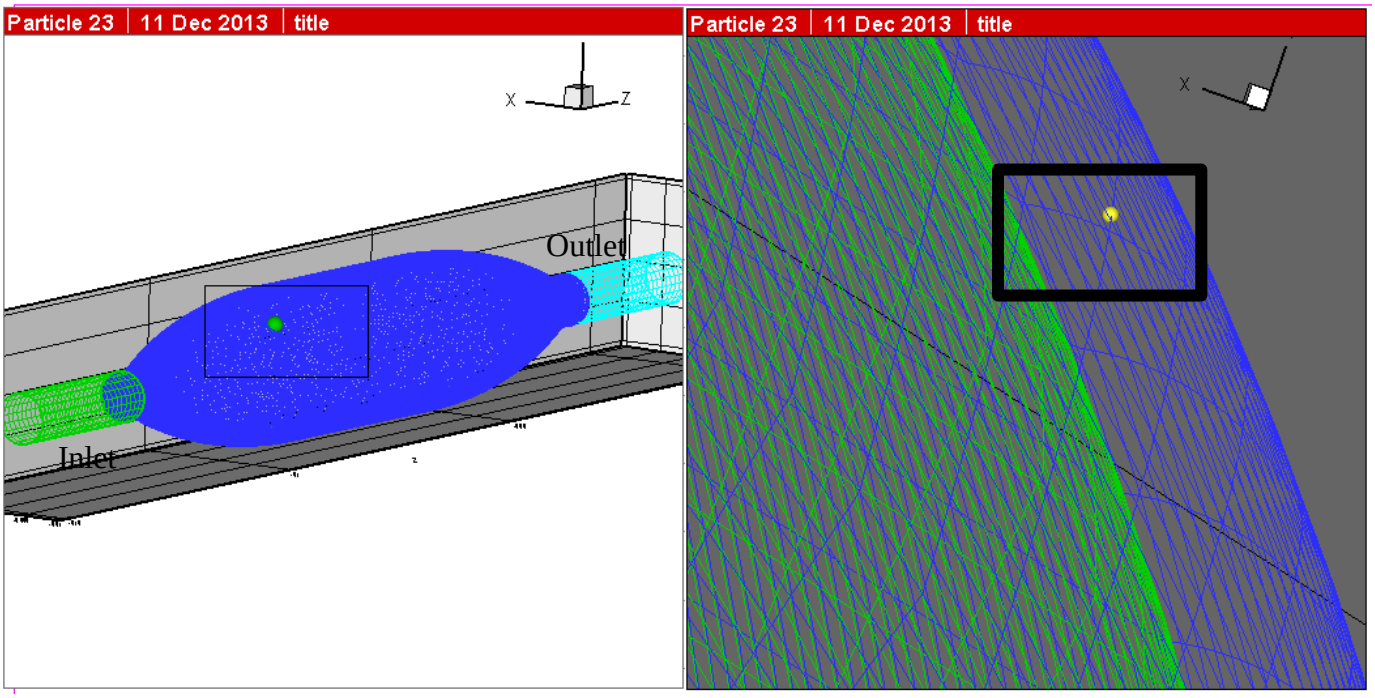

Figure 3.4.38 Particle 23 trapped near the outer wall.

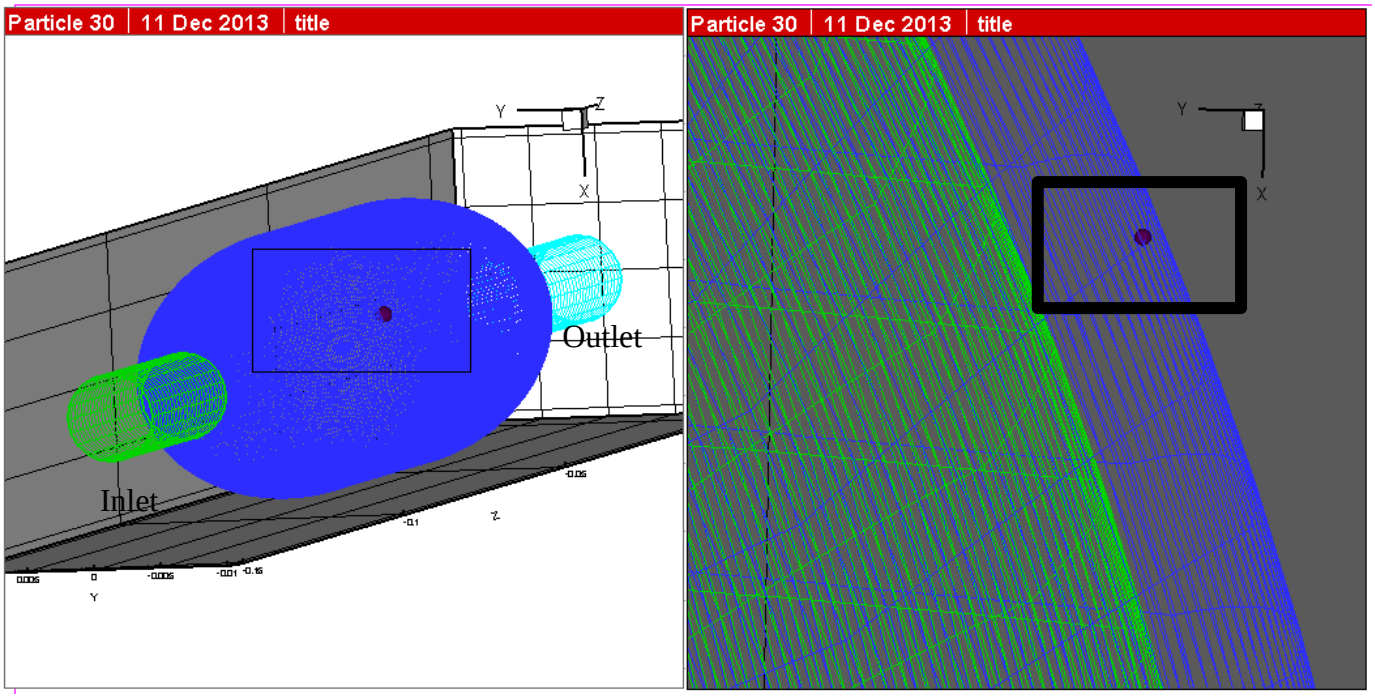

Figure 3.4.39 Particle 30 trapped near the outer wall.

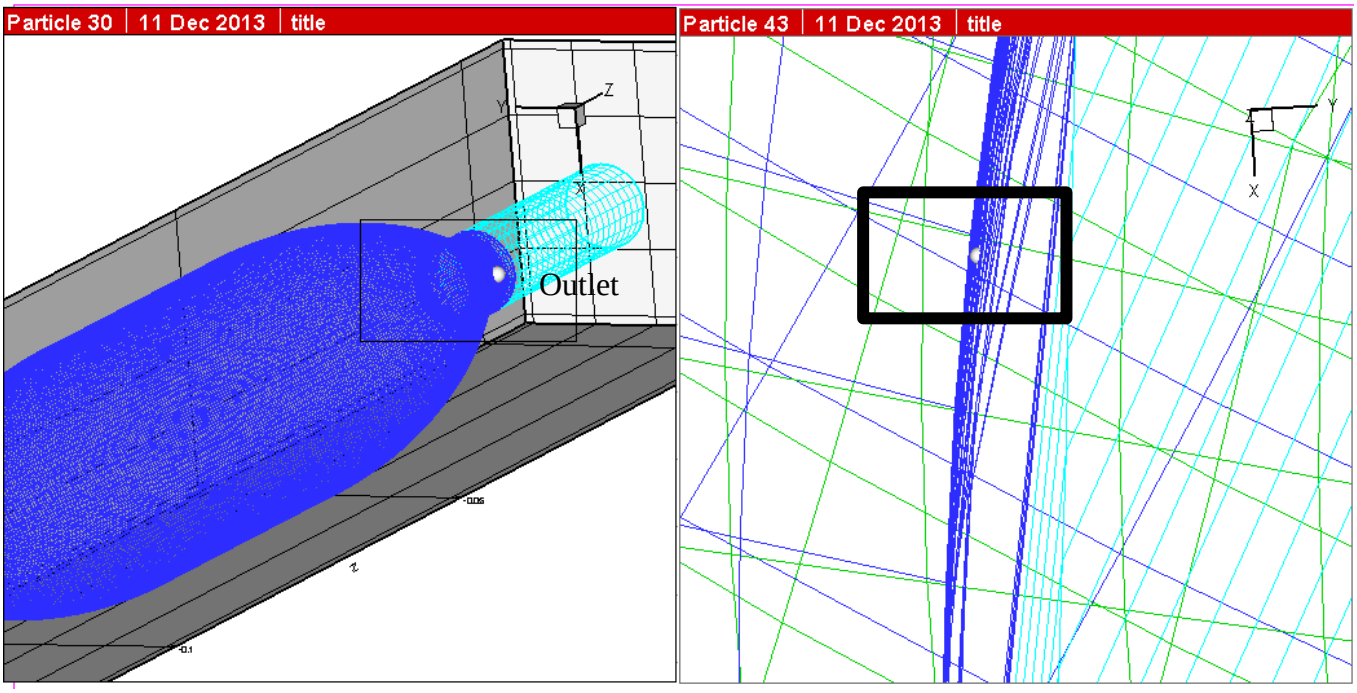

Figure 3.4.40 Particle 43 trapped near the outer wall.

Chapter 4

Hemolysis Analysis

4.1 Hemolysis calculations

The Eulerian hemolysis model was programmed and compiled into CFD solver using User Defined Functions (UDF). Once the flow solution was obtained, the scalar transport equation was solved. The HI values for each computational cell were calculated by post processing the data. One sample data has been summarized for all sets of constants GW, HO, TZ,GW, Giersiepen and Wurzinger constants; HO, Heuser and Opitz constants; TZ, Zhang *et al.* constants, at a test case of 0.1 lpm and 8000 rpm

For the Lagrangian models, the pathlines were obtained by post processing the flow solutions. Parameters for calculating the path lines were chosen so as to get as many path lines to reach the exit as possible. The HI calculations used Matlab (Matlab R2011a, The Math Works Inc. Natick, MA). All the computations were carried out on a PC workstation with Intel(R) Core(TM) 2 Quad CPU 2.40 GHz and 8.00 GB RAM with Windows 7 64-Bit operating system.

The Power Law Equation constants used for hemolysis calculations are summarized in the Table 4.1

Table 4.1 Power Law Equation Constants and their Covering Ranges

Range					
Model	Shear Stress(Pa)	Exposure Time (s)	C	α	β
GW	<255	<700	3.62E−05	0.785	2.416
HO	<700	<700	1.80E-06	0.765	1.991
TZ	50-322	<1500	1.23E-05	0.6606	1.9918

GW, Giersiepen *et al.* constants; HO, Heuser *et al,* constants; TZ, Zhang *et al.* constants;
C α β constants of the power law equation

4.2 Experimental Data Comparison

The experimental values used for comparison of Hemolysis are borrowed form Taskin *et. al.* [33]. The experiments were conducted using a modified Jarvik 2000 blood pump. It consists of a rotating inner spindle, instead of the impeller with blades, and housing without a diffuser and is named as eth Hemolyzer H. The smallest gap between the rotor middle surface and outer housing is 0.1 mm. When the spindle is rotated the, a uniform high shear stress is generated in this gap. The details of the calculations are explained next.

Details of the calculations

Figure 4.1was used to calculate the exposure time using the relation $t_{exp}=\frac{LA}{Q}$. Values of the length and are area were taken from Table 4.2. The values of exposure time were then correlated to HI (%) values from the graph. The values obtained are shown in Table 4.3. The flow rates used in the Mag-lev shearing device were the used for calculating the exposure time for the Mag-lev shearing device. Table 4.4 summarizes the values. These values were then compared with Exposure time vs. HI (%).

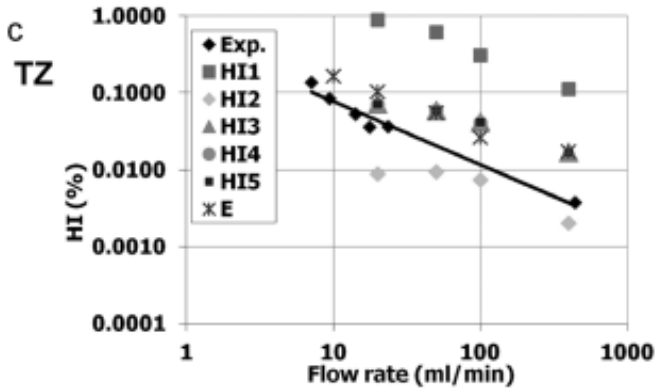

Figure 4.1 HI (%) vs. Flow rate for GW constant for Taskin, 2002

Dimensions[shear gap]	Modified Jarvik 2000	Mag-lev Shearing device Design 4
Length of Gap (mm)	2.5	27
Width of Gap (mm)	0.1	0.125
Radius of inner spindle (Ri) (mm)	7.01	9.55

Table 4.2 Dimensions of modified Jarvik 2000 and Mag-lev shearing dimensions

Flow rate (ml/min)	t exp(s)	HI%
8	8.32E-02	0.12
9	0.0664	0.09
25	0.0265	0.08
30	0.0221	0.06
40	0.0166	0.057
600	0.011	0.006

Table 4.3 Exposure time vs. HI(%) calculated from Taskin 2002

Flow rate (ml/min)	t exp(s)	HI%(HO)	HI%(GW)	HI%(TZ)
50	0.2347	0.2207	32.67	4.097948
100	0.1171	0.1718	26.5	3.3451
150	0.0782	0.0918	13.5	1.7333
200	0.0587	0.0897	12.23	1.6871

Table 4.4 Exposure time and HI% or Mag-lev

4.3 HI Predictions

The HI predictions from two different approaches (one Lagrangian and one Eulerian) each with three sets of power law constants, along with experimental results, are presented in the ensuing sections for varying flow rate conditions and a constant rotational speed of 8000 rpm. The calculations with GW constants over estimated for every HI (%) calculation method. With HO constants the damage was under predicted for Eulerian damage model while using the Lagrangian model the damage values were closest to the experimental values used for comparison. With TZ constants the Lagrangian method overestimated the result while Eulerian method was closest to the experimental values used for comparison. Table 4.5 summarizes the results.

Table 4.5 Hemolysis Prediction Summary

Mode Constants	Eulerian model prediction	Lagrangian Model prediction
GW	Over	Over
HO	Under	Close
TZ	Close	**Over**

4.3.1 Eulerian calculations

The whole fluid domain is considered for this calculation. The steps taken are as follows. Table 4.6 shows the results for each three model constants.

Step 1- Solution of Velocity and pressure

Step 2- Hemolysis analysis

Table 4.6 Custom field function results

Values	Fluent Setup	Result
Giersiepen	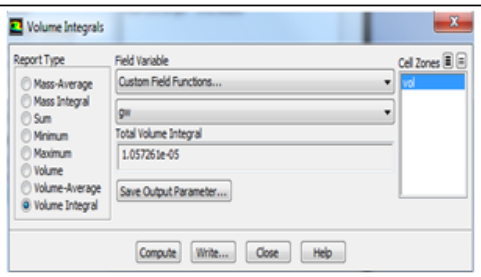	Total Volume Integral gw vol 1.0572612e-05 Net 1.0572612e-05
Heuser	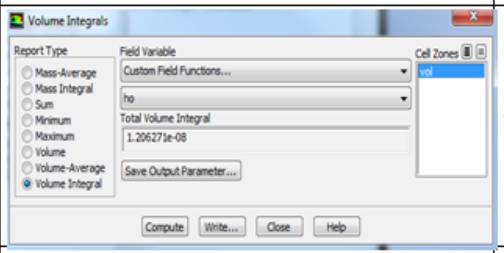	Total Volume Integral ho vol 1.2062706e-08 Net 1.2062706e-08
Taskin	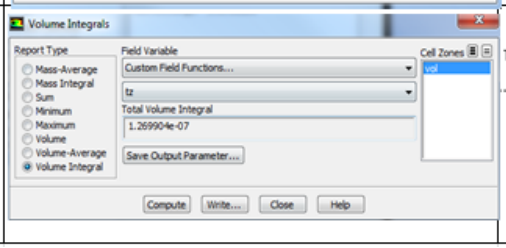	Total Volume Integral tz vol 1.269904e-07 Net 1.269904e-07

Hemolysis prediction by Eulerian approach for the case of 100 ml/min with 8000 rpm was given in Table 4.7. The Eulerian approach with Giersiepen, Heuser and Taskin model predicts 4.26% and 0.023% and 0.18% hemolysis, respectively. Table 4.8 gives the value of HI (%) for different flow rates.

		Giersiepen			Heuser			Taskin		
Total Vol	Q [m^3/s]	I	D	D^0.785	I	D	D^0.765	I	D	D^0.6606
Vol	1.67E-06	1.06E-05	6.34E+00	4.26E+00	1.26E-08	7.56E-03	2.38E-02	1.26E-07	7.56E-02	1.82E-01

Table 4.7 Hemolysis analysis using Eulerian Approach (100ml/min 8000rpm)

Flow rate (ml/min)	HI (%)		
	HIGW	HIHO	HITZ
50	7.27	0.0388	0.2861
100	4.26	0.023	0.1825
150	3.08	0.0168	0.1388
200	2.48	0.0136	0.1157

Table 4.8 HI (%) values calculated by Eulerian method (0.1 lpm, 8000rpm)

Eulerian contour plots at varying flow rate

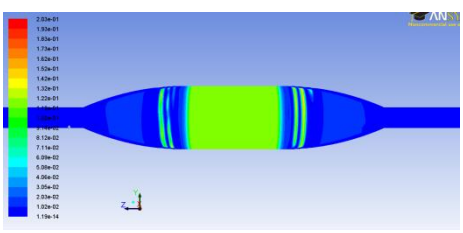

Flow rate 0.05 l/min

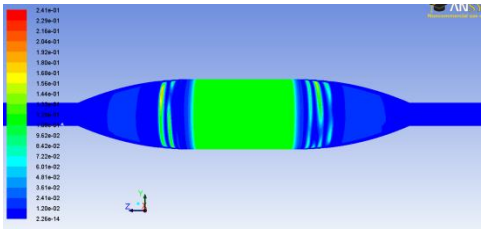

Flow rate 0.1 l/min

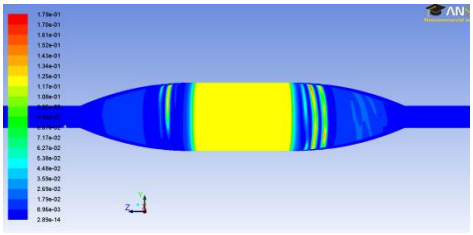

Flow rate 0.15 l/min

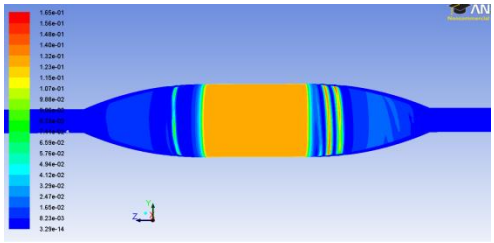

Flow rate 0.2 l/min

Figure 4.2 Eulerian contour plots for damage source source term for increasing flow rates using the HO, Heuser Opitz constants

The plots Figure 4.2 show the contour plots for the damage source term for Eulerian method. The concentration of plasma hemoglobin in the shear gap is visibly higher than the remaining regions. The concentrations in the shear spots are highest, but since their volume is localized the damage can be neglected.

4.3.2 Lagrangian calculations

The Lagrangian path lines were obtained by releasing pseudo particles from the inlet surface of the Maglev-shearing device, design 4. The *HI* accumulations were calculated along the path lines to the outlet. The path lines varied according to the flow rate and the rotational speed. For the considered case of 0.1 l/min at 8000 rpm 48 path lines were tracked out of the 72 released. To check if the path lines were enough the same HI calculations were performed with half of these path lines and the percentage difference was calculated to be 0.11%.

Once the particles successfully escaped the strain rate, velocity magnitude, Z position and time required by each particle was exported for analysis in Matlab. The results are summarized in Figure 4.3. All the values predicted by GW constants over predict the damage. The values predicted by Lagrangian model with HO constants and Eulerian model using TZ constants were closest to the experimental values used for comparison.

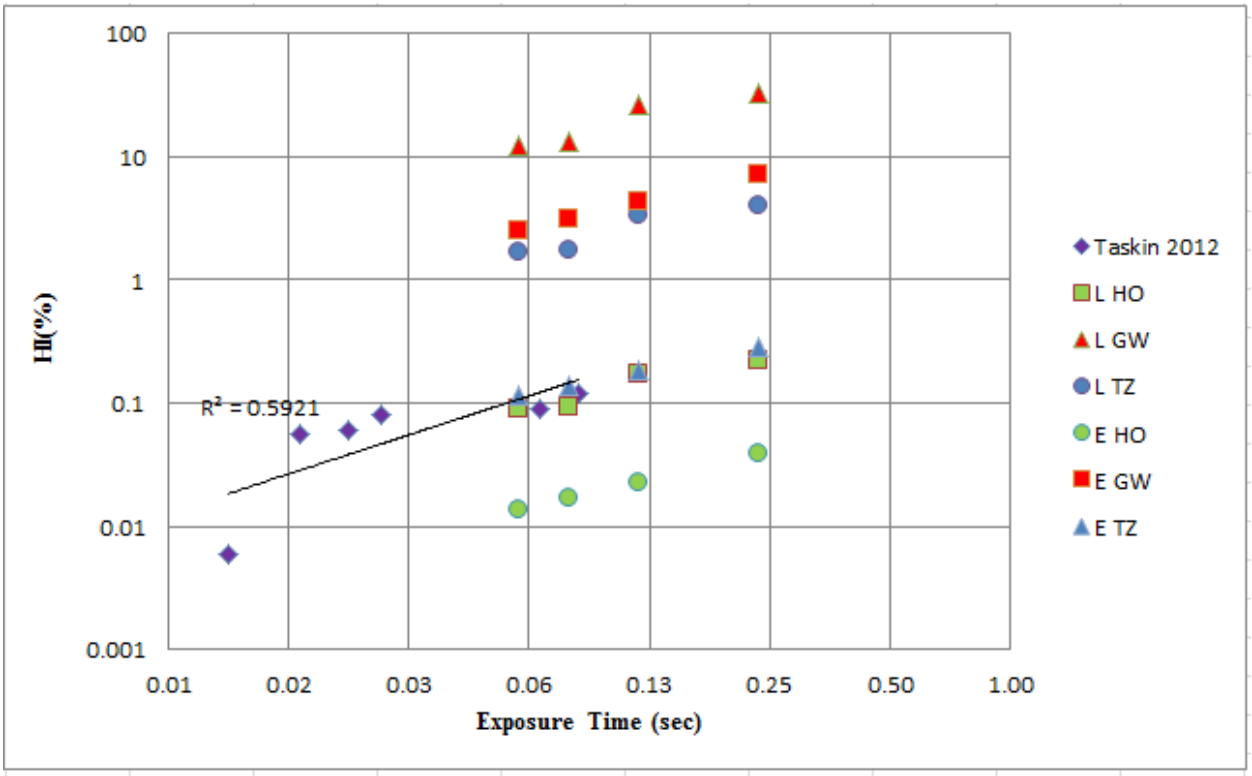

Figure 4.3 HI(%) vs. Exposure time for Design 4 for different set of power law constants. GW, Giersiepen and Wurzinger constants; HO, Heuser and Opitz constants; TZ, Zhang *et al.* constant. E- Eulerian Model, L- Lagrangian Model.

Figure 4.4 to Figure 4.6 show the variation in hemolysis prediction HI(%) for increasing rpm values.

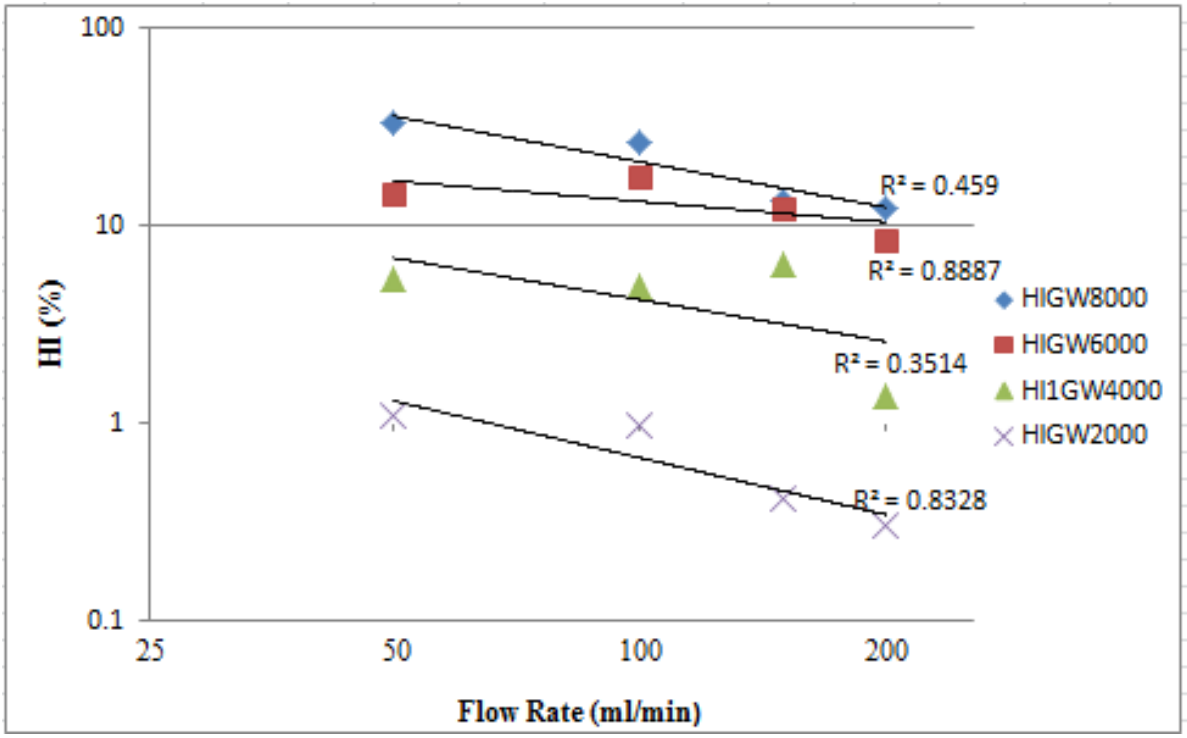

Figure 4.4 Hemolysis HI(%) for Increasing rpm for GW constants

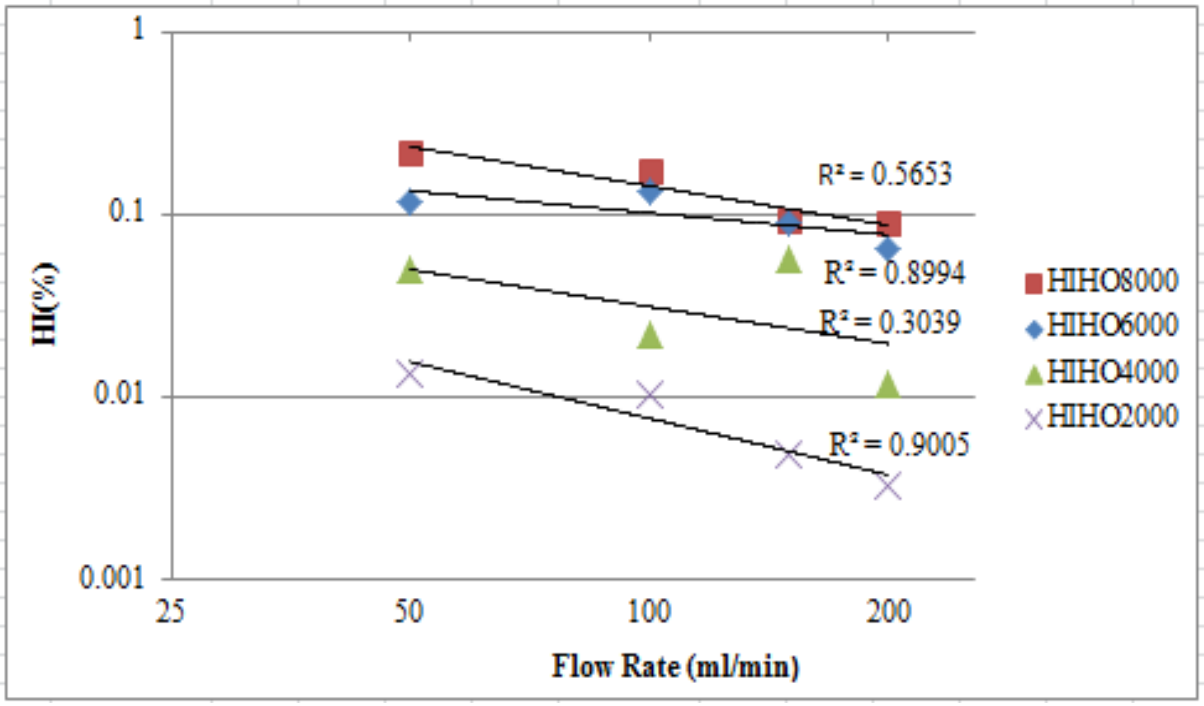

Figure 4.5 Hemolysis HI(%) for Increasing rpm for HO constants

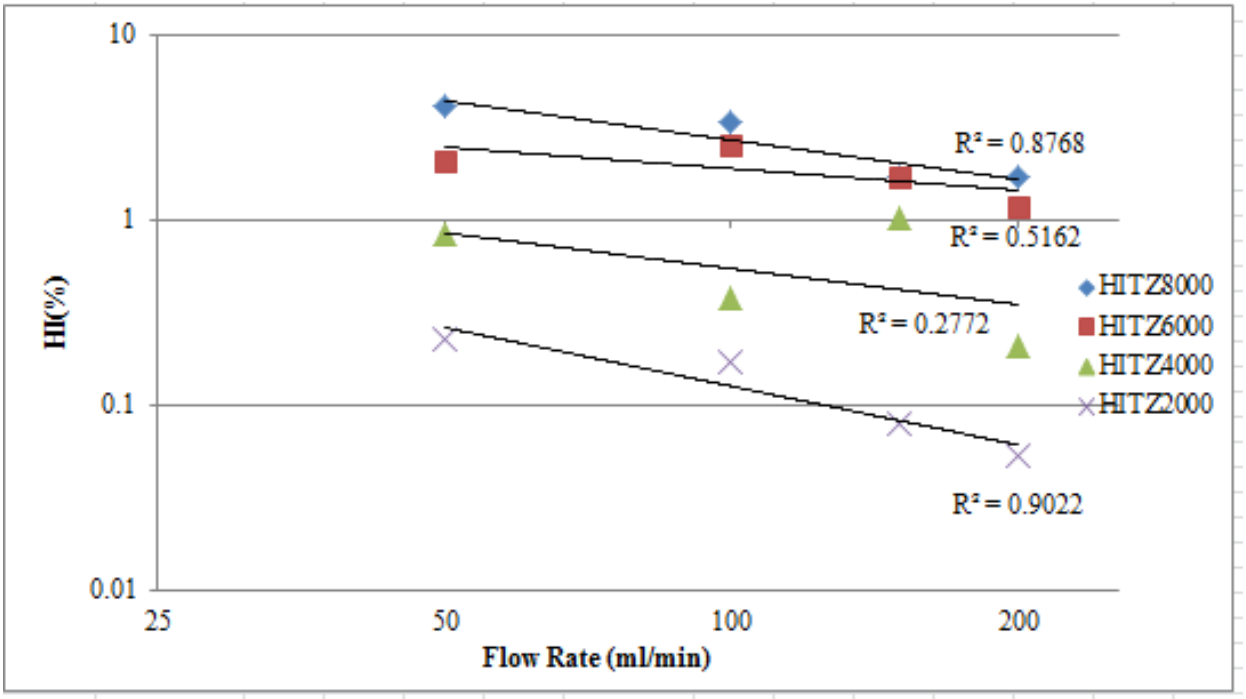

Figure 4.6 Hemolysis HI(%) for Increasing rpm for TZ constants

Figure 4.7 to Figure 4.9 shows the damage distribution along the z-axis. GW power law constants, GW; Giersiepen Wurzinger, have been used for the graphs.

Hemolysis HI distribution plots along path lines for varying flow rate and test case of 8000 rpm

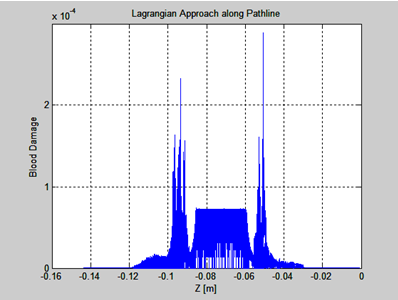

Figure 4.8 HI distribution along path line at 50 ml/min

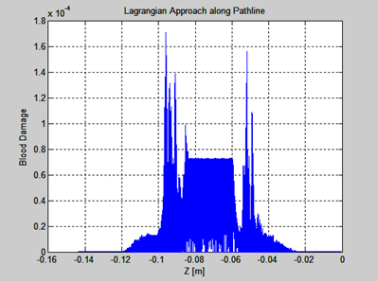

Figure 4.7 HI distribution along path line at 100 ml/min

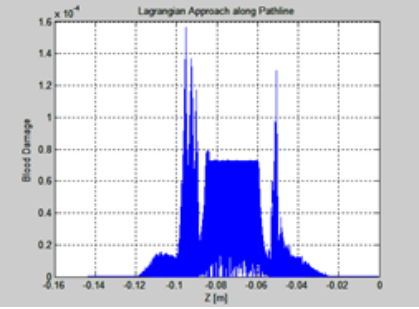

Figure 4.9 HI distribution along path line at 150 ml/min

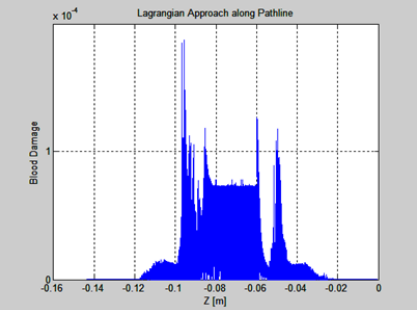

Figure 4.9 HI distribution along path line at 200 ml/min

Figure 4.10 shows the damage distribution for three different constants

Hemolysis HI distribution plots along path lines for three set of power coefficient's at test case of 8000 rpm

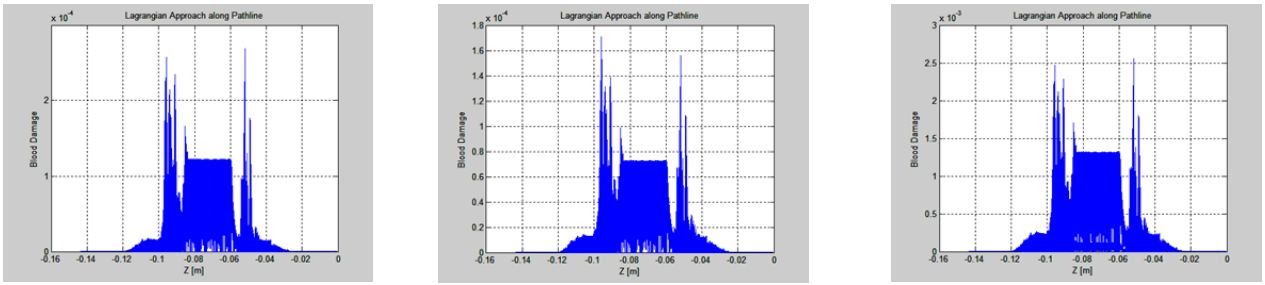

GW HO TZ

Figure 4.10 Hemolysis index distribution along the path lines for different GW, HO and TZ power law constants. GW, Giersiepen and Wurzinger constants; HO, Heuser and Opitz constants; TZ, Zhang *et al.* constants

4.4 Limitations

4.4.1 Lagrangian model using Pathlines

It is important to note that the path lines do not fully represent the complicated flow domains that exist in the actual flow in the Mag-Lev shearing device. For example the path lines that are seeded in the recirculation zone will never exit the device. This can be the case for the design 4 hemolysis. A single extended recirculation zone was observed, however 48 particles were traced out of 72 (66.66%) at 0.1 l/min and 55 out of 72 at 0.2l/min (76.38%).

4.4.2 Meshing

It was observed that more pathlines escape through the outlet for a mesh with higher orthogonal quality and lesser aspect ratio. Orthogonal quality and aspect ratio are used by Fluent to indicate the mesh quality. The orthogonal quality ranges from 0 to 1 with values closer to zero corresponding to low quality. The orthogonal quality increases and the aspect ratio decreases with the mesh fineness. The smallest interval size that could be used for meshing for all the simulations carried over here was 0.4 in Gambit. Due to limited available resources a mesh with an interval size of 0.3 or 0.2 could not be tested. Thus mesh fineness was limited to element/interval size of 0.4, in Gambit. A summary of orthogonal quality and aspect ratio for each design meshed in Gambit is listed in Table 4.9

Table 4.9 Mesh Orthogonal quality and Aspect ratio

Design	Orthogonal Quality	Aspect ratio
1	1.30E-01	1.41E+02
2	2.56E-01	9.34E+02
3	6.35E-02	2.35E+02
4	4.12E-01	5.02E+01

Table 4.10, explains the situation for pathlines escaping the out let at specific rotational speeds and the designs for which the testing is done. It can be noted that, for designs 1 and 2 path lines did not escape beyond 1000 rpm. The simulation was carried out at 2000 rpm for design 1 and 2. The path lines failed to exit through the out let at this rpm. It was assumed that the presence of recirculation zones/ Taylor vortices could be a reason for this and the axial velocity vector contour plots were plotted for design 1 and 2 along with the axial velocity profile plot in the wide gap region for design 1 and linearly increasing gap region for design 2.Figure 4.11, Figure 4.12**,** shows the axial velocity vector plot for the design 1 and 2. Recirculation zones can be clearly seen to be present in the wide gap region for design 1 and the linearly increasing gap of Design 1 and 3. The axial velocity profile plot is also sinusoidal which confirms the existence

of a non–Couette flow in wide gap region and the linearly increasing gap region for Design 1 and 3 in Figure 4.13 Figure 4.14. Thus it was assumed that the reason the pathlines did not escape the outlet was due to the presence of recirculation zones/ Taylor vortices. Figure 4.15, Figure 4.16 show the incomplete path lines for Design 1 and 3.

Table 4.10 Summary for Path line escaping outlet at specific rotational four designs tested.

		Design			
Rpm	pathlines	1	2	3	4
1000	atleast one path line escaped	✓	✓	✓	✓
2000	atleast one path line escaped	×	×	✓	✓
6000	atleast one path line escaped	×	×	×	✓

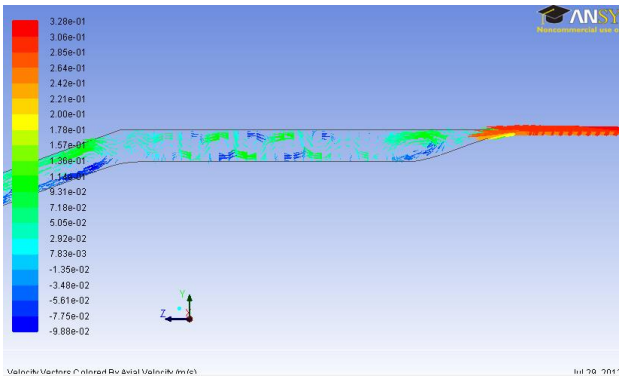

Figure 4.12 Axial velocity vector plot, design 1

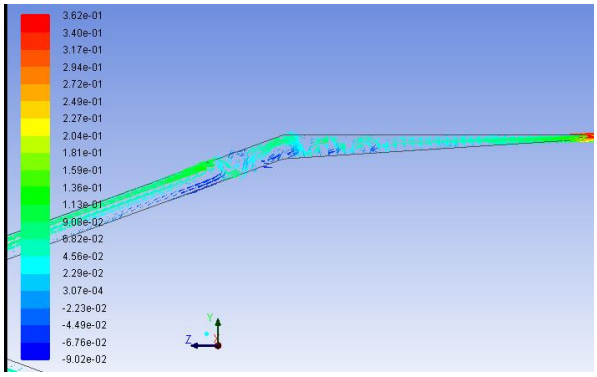

Figure 4.11 Axial velocity vector plot, design 3

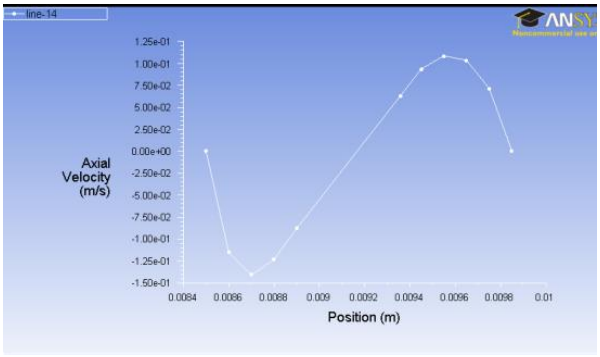

Figure 4.14 Axial velocity plot, design 1

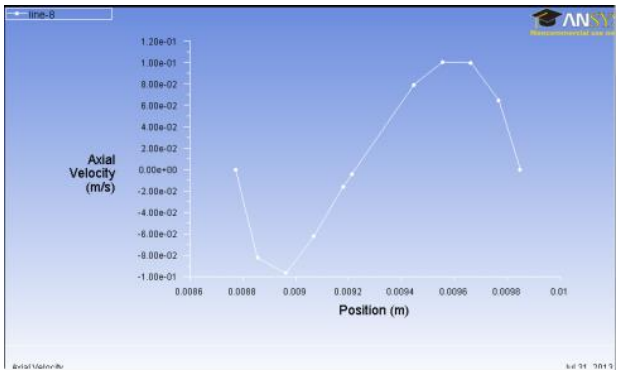

Figure 4.13 Axial velocity plot, design 2

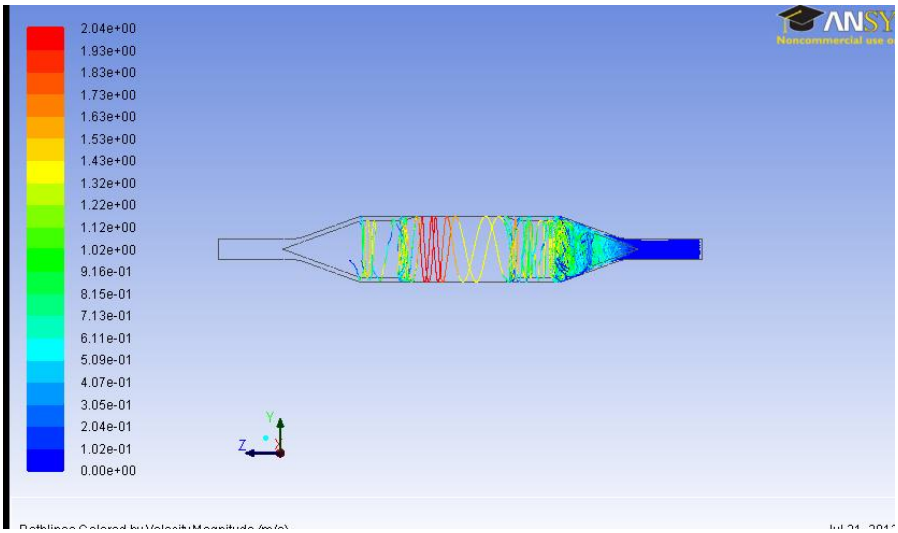

Figure 4.15 Pathline for design 1 (original design)

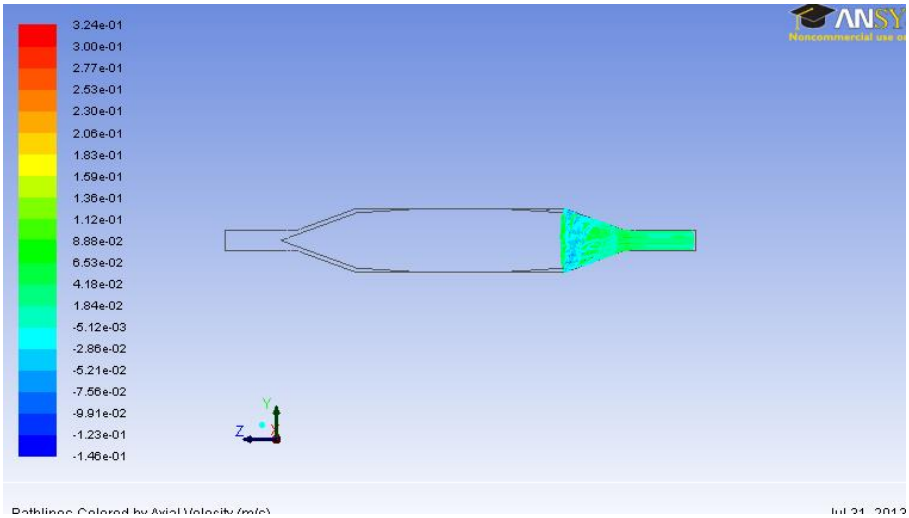

Figure 4.16 Path lines for design 3 (Linear incereasing gap)

However in case of design 3, in spite of having no recirculation zones, no path lines escaped beyond 6000 rpm, and flow rate of 100 ml/min. Figure 4.17 shows the vector velocity plot for design 3 at 100ml/min at 6000 rpm while Figure 4.18 shows the path lines tracked. It is important to note that the path lines stop just before the uniform gap starts where no negative velocity exists, so they are not trapped by any Taylor vortices or recirculation zones. Figure 4.19 shows the axial velocity profile in the uniform gap, which is parabolic in nature conforming a Couette flow.

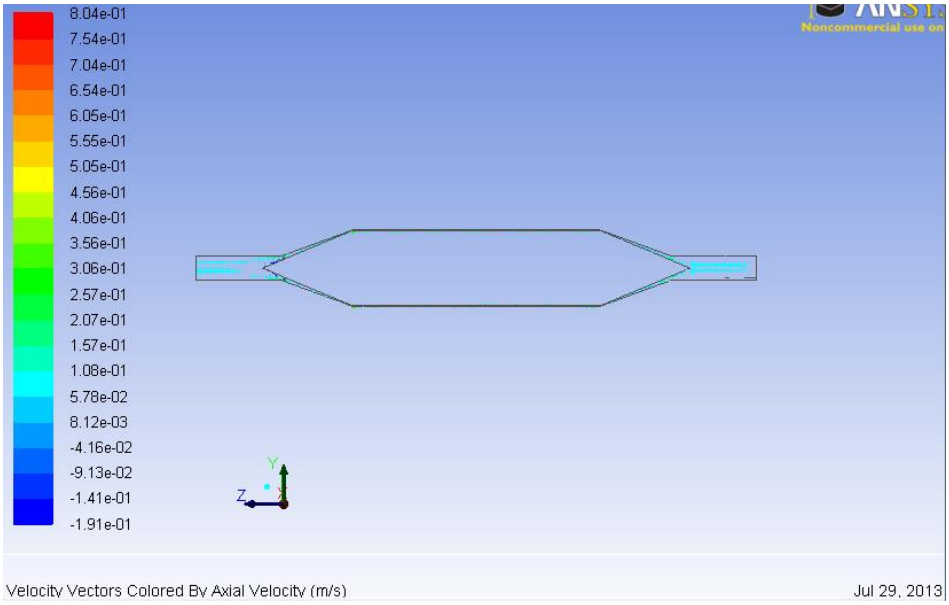

Figure 4.17 Axial velocity Vector plot for design 2

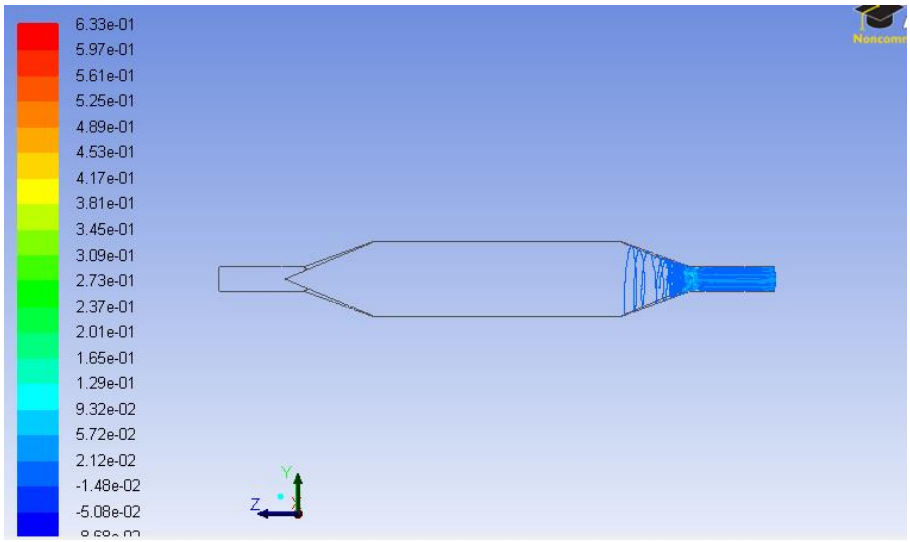

Figure 4.18 Path lines tracked at 6000 rpm for design 2

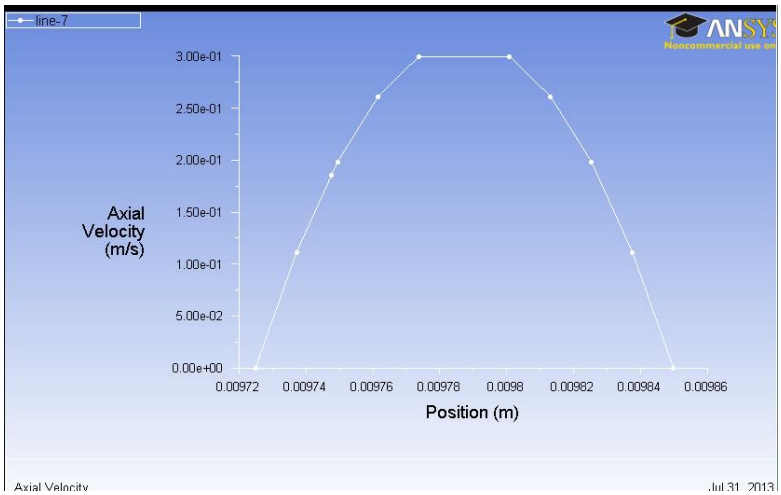

Figure 4.19 Axial velocity profile in thin gap region for design 2 at 6000 rpm and 100 ml/min

For design 4, 48 particles were traced out of 72 (66.66%) at 0.1 l/min and 55 out of 72 at 0.2l/min (76.38%) at rotational speed of 8000 rpm. The simulation at, at 8000 rpm and 100 ml/min showed the existence of an elongated Taylor vortex or recirculation zone, Figure 4.20. Figure 4.21 shows they close up of axial velocity vector plot. More than 50 % particles make it to the outlet. The particles that do not make it to the outlet might have been trapped in the recirculation zone. These trapped particles never make it to the outlet while the ones that make it to the outlet never really get trapped in eth Taylor vortices, hence the data for hemolysis is acquired from particles, are in fact the particles that have not been seeded in the Taylor vortex. The Mat lab graphs of shear stress vs. exposure time, from hemolysis evaluation for design 4 at 8000 rpm and 100ml/min show the exposure time for which the particles are subjected to uniform shear stress. The Table 4.11 summarizes the results and it can be seen that the exposure time from simulation is close to the analytical value suggesting that, the particles used to acquire that data are not seeded in the Taylor vortices, since if they were trapped the exposure times would be higher. Figure 4.23, Figure 4.24 show the shear stress vs. exposure times for 100 ml/min and 200 ml/min.

At 25000 rpm the path lines did not exit the outlet. Figure 4.22 shows the path lines traced at 25000 rpm at 100 ml/min.

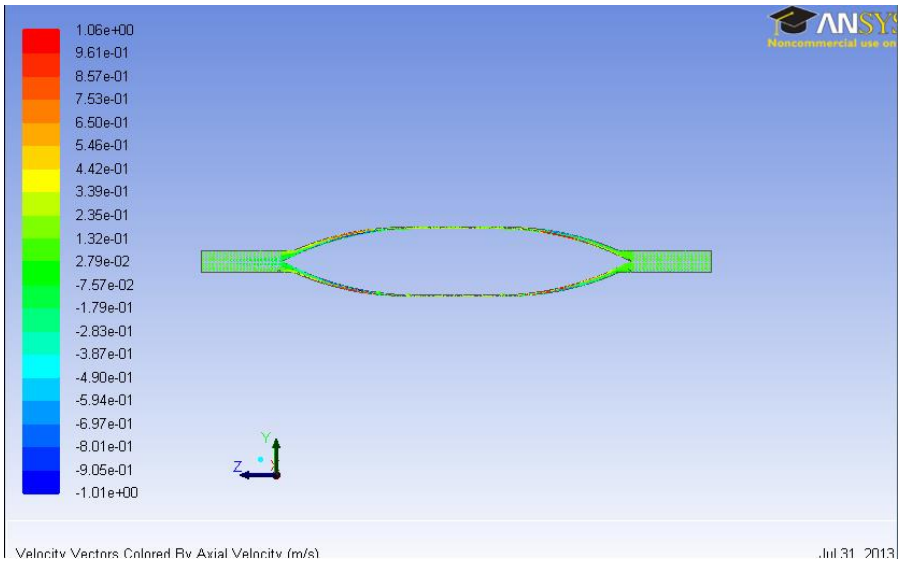

Figure 4.20 Axial velocity vector plot for design 4

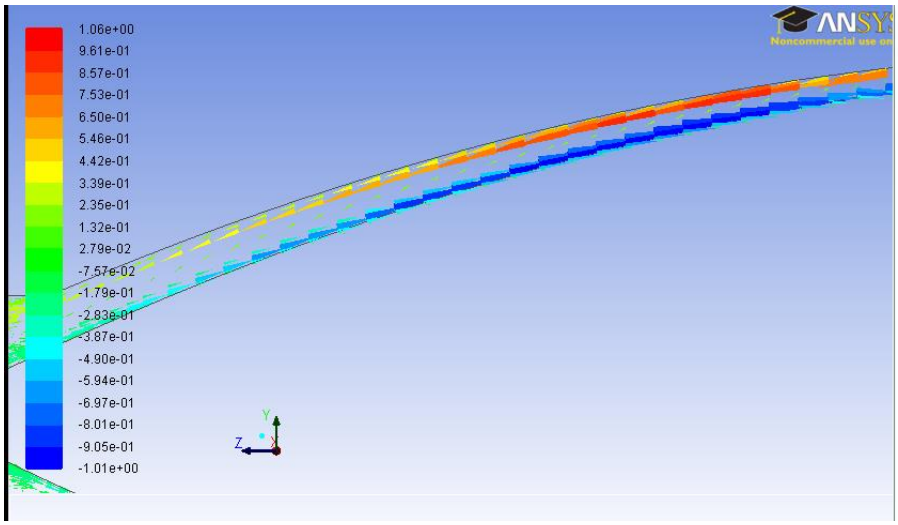

Figure 4.21 Axial velocity vector plot for design 4 (Close up of the elongated vortex)

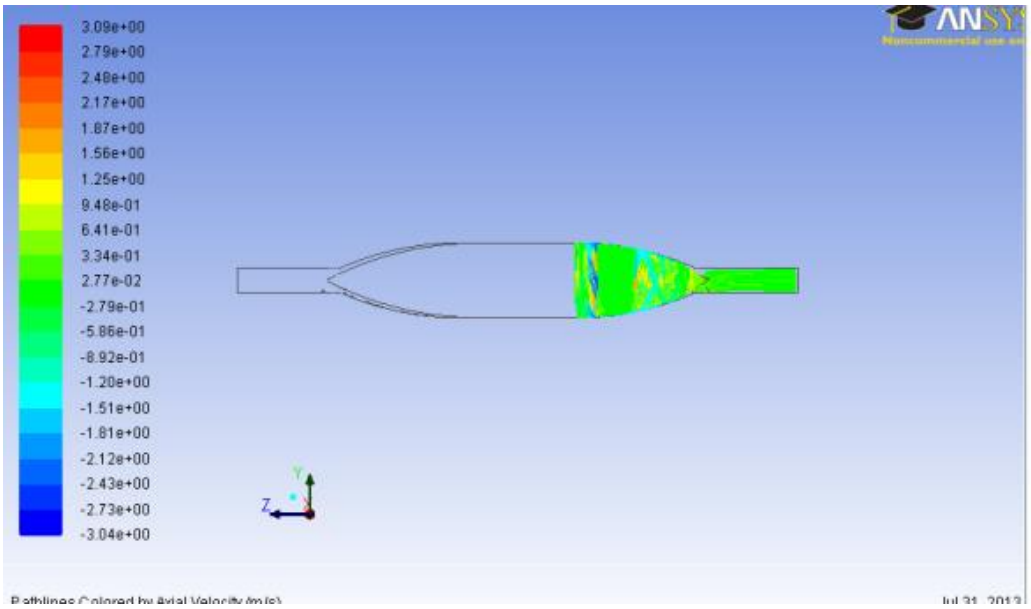

Figure 4.22 Pathlines traced at 25000 rpm at 100 ml/min

	Shear stress-τ (Pa)	Exposure time-texp(s) 100 [ml/min]	Exposure time-texp(s) [200ml/min]
Simulation	248	0.08	0.040
Analytical	240	0.11	0.058

Table 4.11 Shear stress and exposure time for Design 4 at 8000 rpm

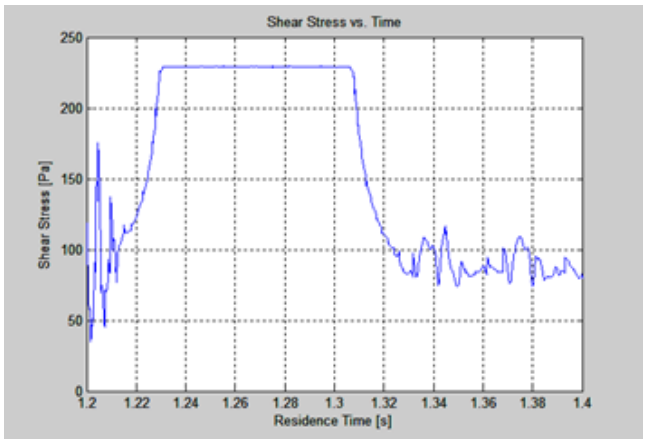

Figure 4.23 Shear stress vs. Exposure time for 8000 rpm at 100 ml/min

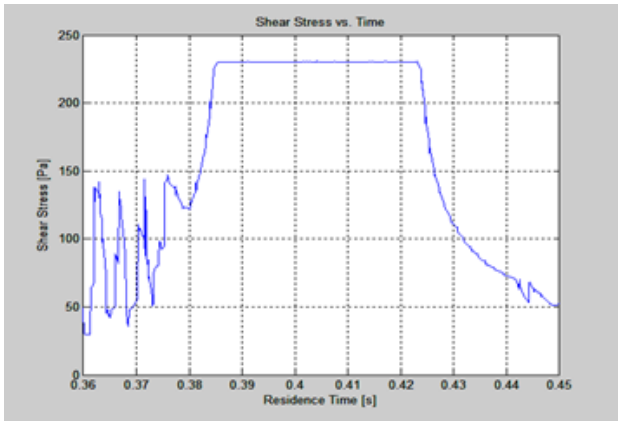

Figure 4.24 Shear stress vs. Exposure time for 8000 rpm at 200 ml/min

To summarize the results it was assumed that the path lines did not escape for design 1 and 2 due to the presence of Taylor vortices. The presence was confirmed by the axial velocity vector plots and axial velocity profile plots in the wide and linearly increasing gap regions. However for design 3 the path lines failed to exit the outlet even when a Couette flow existed within the entire gap. Path lines successfully exited design 4 in spite of having an elongated vortex in the gap region upstream and downstream the shear gap. The results are summarized in Figure 4.25

0.1 lpm, 3000 rpm	Design
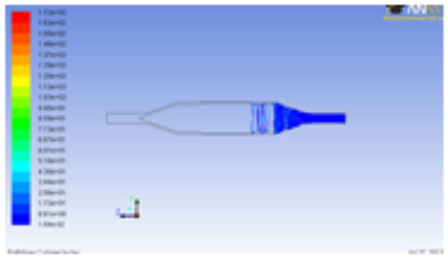	Design 1
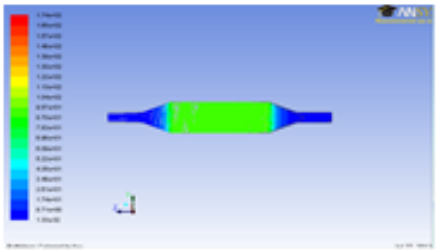	Design 2
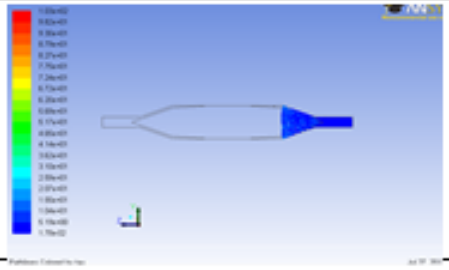	Design 3
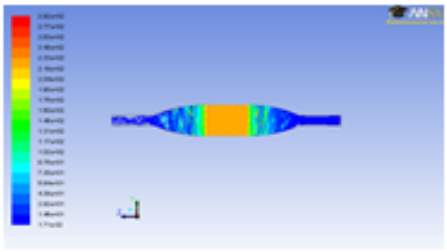	Design 4

Figure 4.25 Pathlines for all Designs at a test case of 3000 rpm and 0.1 ml/min flow rate

Table 4.12 shows the orthogonal quality and the aspect ratio for four different designs. It was observed that for the design meshes with higher orthogonal quality and lesser aspect ratios, higher number of path lines escaped the outlet for increasing rotational speeds.

Table 4.12 Orthogonal quality aspect ratio for all the meshes

	Design			
Orthogonal quality (Descending order)	4	1	2	3
Aspect ratio (Descending order)	3	2	1	4

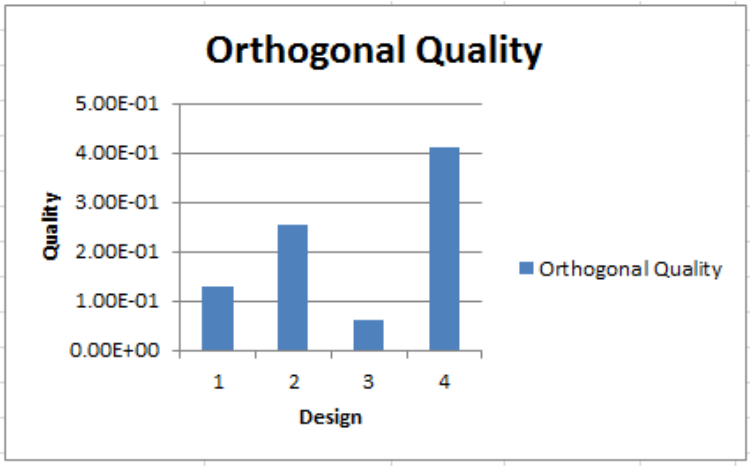

Figure 4.26 Orthogonal Quality for each design at 0.4 interval size

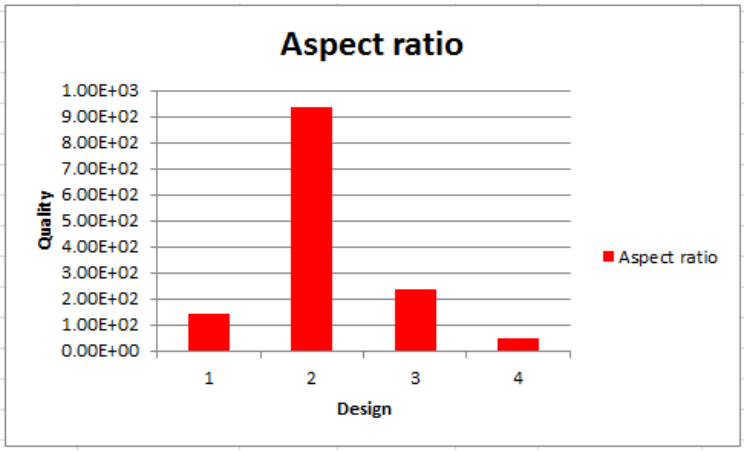

Figure 4.27 Aspect ratio for each design at 0.4 interval size

Figure 4.27, Figure 4.26 show the variation in Orthogonal Quality and Aspect ratio with respect to each design

4.4.3 Orthogonality and successful path line tracking

Design 3 had the least orthogonal quality and highest aspect ratio, a bad combination for higher number of path lines escaping the outlet. Thus, path lines were not able to escape design 3 beyond 6000 rpm even when it did not have any recirculation zones in the flow path. For Design 4 which has higher orthogonal quality and least aspect ratio the path lines escaped beyond 6000

rpm in spite of a recirculation zone in the flow path. Path lines did not escape design 4 beyond 25000 rpm. It is possible that path lines escaping the out let are influenced by the mesh fineness, since this dictates the orthogonal quality. As the interval size decreases the mesh orthogonal quality increases. However the least interval size that could be used for meshing in Gambit was 0.4, due to limited resources available for Fluent. Inc. Design 1 and design 2 were midway w.r.t the orthogonal quality and aspect ratio; however path lines did not escape the outlet beyond 2000 rpm. Path lines not exiting the outlet for design 1 and 2 could be well because of the mesh fine ness and not because of the recirculation zones. It is also possible that path lines get stuck in the Taylor vortices for design 1 and 2. If we are able to increase the mesh fineness for design 1 and 2 we can find out if the path lines really get seeded in the Taylor vortices for design 1 and design 3, since then the mesh fineness would not be an issue for path lines successfully escaping the outlet. The mesh fineness can be increased by using an interval size of 0.2 or 0.3 in Gambit while meshing. However, due to the available resources for Fluent Inc. a finer mesh size for design 1 and 3 could not be tested here. They could be studied in future work

The table below summarizes the path lines tracked for all the designs for a sample case of 3000 and 6000 rpm at 100 ml/min while the Table 4.13 shows the path lines tracked at 300 rpm at 100 ml/min

Table 4.13 Summary for escaping path lines for different designs

	#	RPM	Atleast one pathline escaped	Recircualtion
Design	1	3000	×	✓
		6000	×	✓
	2	3000	✓	×
		6000	×	×
	3	3000	×	✓
		6000	×	✓
	4	3000	✓	✓
		6000	✓	✓

4.4.4 Pathlines

For this study massless particles were used for particle tracking. These massless particles were released from the inlet of the device and they escaped from the outlet of the device. Ideally, the particles need to be designed as blood particles by modeling them as a custom “blood-particle” with constant blood density of 1050 kg/m3.

An attempt was made to model the particles as blood particles; however these blood particles did not escape the outlet for cases in which the massless particles were able to escape the outlet. The exact reason for this could not be determined. This could be because of the mesh inaccuracies. However this is something that could be studied in future work

4.4.5 Hemolysis

The study does not account for the complicated flows *in vivo* and only assesses hemolysis models for reproducing *in vitro* hemolysis. When VADs are implanted, the flow through them is determined by the interaction of the VAD and the native cardio vascular system and therefore has a pulsatile component. *IN vivo*, the plasma free hemoglobin is a balance between the amount of hemoglobin coming from the RBCs and the amount being processed by the kidneys. These hemolysis models cannot calculate the *in vivo* hemolysis[33]

Chapter 5

Conclusion and Discussion

The gap region for the original geometry, upstream and downstream the shear gap was changed to a curved shape to observe the effect on the Taylor vortices. It is observed that a single elongated recirculation zone exists for the changed design, Design 4. This however does not affect the residence time of the particles released for hemolysis analysis for Design 4as discussed in Section 3.4.3 for a single particle. The exposure time calculated analytically for Design 4 is 0.11 msec while that found from simulation is 0.08 msec at a rotational speed was set at 8000 rpm and flow rate of 100 ml/min. The difference in values is very small (0.03msec, 6% difference). Also, the exposure time found from analysis for a single particle at 200 ml/min, 8000 rpm was 0.058 msec while that found from simulation is 0.040 msec (0.018 msec a 12% difference). Since the difference is small it can be concluded that the simulation results are consistent. The analysis for the other escaping particles is not done in this case. However, this discussion of residence time and exposure time can be extended to other blood particles that escape through the outlet, 48 particles in case of 100 ml/min flow and 55 in case of 200ml/min at 8000 rpm case.

So we observe that when the rotational speed of the inner cylinder is set at 8000 rpm a single elongated Taylor vortex is generated. Also, the exposure time values obtained from the

data analyzed for a single massless blood particle escaping through the outlet is close to the analytical value with a (6% difference for 8000 rpm 100ml/min case and 12% difference for 8000 rpm and 200ml/min case) while the residence time for the single blood particle passing through the device observed is not affected by the vortices. Thus as the escaping particles are not affected by the elongated vortex and the difference between the analytical and simulation exposure time values is small the hemolysis results will be more accurate. Hence, Design 4 is a better design in which only a single elongated vortex forms upstream and downstream the shear gap region at high rotational speeds and thus allows to achieve a higher shear stress value of up to 230 Pa i.e. >150 Pa.

The particles that did not escape the outlet were analyzed using Tec plot to find their final locations. Careful inspection of the particle trajectories showed that the particles that fail to escape are trapped on the outer wall (housing) of the device. This could be because of the mesh fineness. This was not studied in detail and thus could be something to look into for future work

Hemolysis was analyzed using the Eulerian scalar transport and Lagrangian particle tracking methods for the improved design, Design 4. It was found that the Eulerian damage model with the TZ constants and Lagrangian damage models with HO constants detected hemolysis closest to the experimental values taken from Taskin et.al 2012. These values should be cross checked with experiments using a physical Mag-lev shearing device of Design 4.

The meshing of the geometry also plays an important role in analysis. The mesh independence was done using the interval size in this work which decreases the length of each

cell thus increasing the number of total cells along a particular length. The mesh independence for cells in between the inner rotating and outer stationary cylinder was not done in this work. It is important to conduct mesh independence in between the cylinders to take into the boundary effects accurately. A total of 8 boundary layers were specified in this work. Four boundary layers were attached to the outer stationary cylinder and four layers were attached to the inner rotating cylinder. The boundary layers were the most that could be specified on each cylinder before they interfered with the boundary layer on the other cylinder. The spacing between each boundary layer was also maintained constant. The spacing between these layers can be changed. The mesh independence of the boundary layers specified can be carried out in future work and the results can be compared with this work.

To summarize, Design 4 of Mag-lev shearing device is a better design that can provide a good platform for better hemolysis evaluation.

Completed work

Design 1- Original Design

The original design for the Mag-lev shearing device was remodeled in solid works and it was analyzed in Fluent Inc. This was named as design 1.The wide gap region was affected by Taylor vortices beyond 500 rpm. Pathlines were released from the inlet; however no path lines escaped through the outlet beyond a speed of 2000 rpm. Hence in order to track path lines at

higher rpm shape modifications to the gap region upstream and downstream were made and analysis was undertaken.

Design 2- Linearly increasing gap design

A uniform gap throughout the length of the device was modeled and analyzed for hemolysis prediction. This was named as design 2. It was observed that the path lines did not successfully escape after 3000 rpm. Nonetheless the highest shear stress and exposure time was recorded for this case along with the hemolysis. The highest hear stress recorded was 87 Pa.

Design 3-Uniform gap design

The uniform gap shape design was then changed to a linearly increasing gap shape which was denoted as design 3. Even for this design Taylor vortices were predicted for rpm higher than 500 rpm. Path lines did not escape beyond 2000 rpm; hence further shape modification for the gap region was undertaken.

Design 4- Curved gap design

The wide gap design was then changed to a curved shape upstream and downstream the shear gap region. Of all the designs this design had the highest orthogonal quality and the lowest aspect ratio. The design 4, had an elongated vortex along the upstream and the downstream region of shear gap as compared to the wide gap completely filled with vortices. Path lines

successfully escaped the outlet at 8000 rpm for which hemolysis has been calculated. This speed was selected since using this speed the results could be compared to experimental data from the reference paper named Evaluation of Eulerain and Lagrangian models for Hemolysis Estimation by Taskin. *et. al.* Path lines did not escape beyond 25000 rpm. Hemolysis has been evaluated using three sets of constants viz. (A) GW constants (B) HO constants (C) TZ constants.GW, Giersiepen and Wurzinger constants; HO, Heuser and Opitz constants; TZ, Zhang *et al.* constants.

Future Work

1. The Boundary layers between the outside stationary and inner rotating cylinder was maintained constant. A total of 8 boundary layers were modeled with 4 attached to the outer cylinder and 4 attached to the inner cylinder. Mesh refinement can be done for the boundary layers to determine if it affects the solution and the simulation hemolysis results.
2. It would also be beneficial to use a ANSYS Fluent package that reads more than 5e+5 cells. This will allow one to create a finer mesh with more number of cells and determine if this affects the particles getting trapped on the outer cylinder wall currently. A 2D section of the geometry can also be modeled since the geometry is symmetric. This will allow the use of an interval size lesser than 0.4 mm to create a finer mesh while using the student version of ANSYS Fluent (one that has the 5e+5 cell reading limitation) Analysis can be conducted to see if it affects the particles that get stuck on the outer wall (housing).
3. Analysis can done to find out why the particles are stuck on the outer wall (housing) as is seen using Tec-plot graphs. One can also determine if the use of a finer mesh affects the particles that get stuck on the housing walls.
4. Analysis of the exposure times for the other particles that escaped the outlet for the flow rates 100 ml/min and 200 ml/min at 8000 rpm can be carried out.

5. In this study the particles used for particle tracking were massless. It will be beneficial to model the particles as blood particles with a density of 1050 kg/m^3
6. Once the numerical modeling is complete the next step would be to fabricate the new design for the Mag-lev shearing device that could be used for experimental analysis.

References

[1] J. Wu, J. F. Antaki, T. a Snyder, W. R. Wagner, H. S. Borovetz, and B. E. Paden, "Design optimization of blood shearing instrument by computational fluid dynamics.," *Artif. Organs*, vol. 29, no. 6, pp. 482–9, Jun. 2005.

[2] O. Myagmar, "Evaluation of CFD based Hemolysis Prediction Methods," no. August, 2011.

[3] A. Untaroiu, H. G. Wood, P. E. Allaire, A. L. Throckmorton, S. Day, S. M. Patel, P. Ellman, C. Tribble, and D. B. Olsen, "Computational design and experimental testing of a novel axial flow LVAD.," *ASAIO J.*, vol. 51, no. 6, pp. 702–10.

[4] T. A. L P Chua, "Measurements of gap pressure and wall shear stress of a blood pump model.," *Med. Eng. Phys.*, vol. 22, no. 3, pp. 175 – 88, 2000.

[5] M. Behbahani, M. Behr, M. Hormes, U. Steinseifer, D. Arora, O. Coronado, and M. Pasquali, "A review of computational fluid dynamics analysis of blood pumps," *Eur. J. Appl. Math.*, vol. 20, no. 04, p. 363, Mar. 2009.

[6] L. J. Wurzinger, R. Opitz, P. Blasberg, and H. Schmid-Schönbein, "Platelet and coagulation parameters following millisecond exposure to laminar shear stress.," *Thrombosis and haemostasis*, vol. 54, no. 2. pp. 381–6, 30-Aug-1985.

[7] "Estimation of Shear Stress-related blood damage in heart valve prostheses.pdf." .

[8] R. J. Donnelly, "Experiments on the Stability of Viscous Flow Between Rotating Cylinder. III. Enhancement of Stability by Modulation," *Proc. R. Soc. A Math. Phys. Eng. Sci.*, vol. 281, no. 1384, pp. 130–139, Aug. 1964.

[9] R. Paul, J. Apel, S. Klaus, F. Schügner, P. Schwindke, and H. Reul, "Shear stress related blood damage in laminar couette flow," *Artif. Organs*, vol. 27, no. 6, pp. 517–529, 2003.

[10] G. Heuser and R. Opitz, "A Couette viscometer for short time shearing of blood.," *Biorheology*, vol. 17, no. 1–2. pp. 17–24, Jan-1980.

[11] C. D. Andereck, S. S. Liu, and H. L. Swinney, “Flow regimes in a circular Couette system with independently rotating cylinders,” *J. Fluid Mech.*, vol. 164, no. -1, p. 155, Apr. 2006.

[12] G. Baier, “LIQUID-LIQUID EXTRACTION BASED ON A NEW FLOW PATTERN : TWO-FLUID TAYLOR-COUETTE FLOW By.”

[13] H. Oualli, S. Hanchi, A. Bouabdallah, and B. El Bahri, “TAYLOR-VORTEX FLOW CONTROL USING RADIALLY OSCILLATING INNER CYLINDER,” vol. C, no. June, pp. 14–17, 2010.

[14] R. C. Diprima, “The stability of a viscous fluid between rotating cylinders with an axial flow,” *J. Fluid Mech.*, vol. 9, no. 04, p. 621, Mar. 2006.

[15] H.-C. Hu and R. Kelly, “Effect of a time-periodic axial shear flow upon the onset of Taylor vortices,” *Phys. Rev. E*, vol. 51, no. 4, pp. 3242–3251, Apr. 1995.

[16] B. Denne and M. Wimmer, “Travelling Taylor vortices in closed systems,” *Acta Mech.*, vol. 133, no. 1–4, pp. 69–85, Mar. 1999.

[17] M. Wimmer and J. Zierep, “Transition from Taylor vortices to cross-flow instabilities,” *Acta Mech.*, vol. 140, no. 1–2, pp. 17–30, Mar. 2000.

[18] C. Egbers and G. Pfister, Eds., *Physics of Rotating Fluids*, vol. 549. Berlin, Heidelberg: Springer Berlin Heidelberg, 2000.

[19] R. C. Diprima, “The stability of a viscous fluid between rotating cylinders with an axial flow,” *J. Fluid Mech.*, vol. 9, no. 04, p. 621, Mar. 2006.

[20] G. G. and danny Blestein, “Biological effects of dynamic shear stress in cardiovascular pathologies and devices.pdf,” 2008.

[21] S. DONG, “Direct numerical simulation of turbulent Taylor–Couette flow,” *J. Fluid Mech.*, vol. 587, pp. 373–393, Aug. 2007.

[22] A. Garon and M.-I. Farinas, “Fast three-dimensional numerical hemolysis approximation.,” *Artif. Organs*, vol. 28, no. 11, pp. 1016–25, Nov. 2004.

[23] J. Zhang, B. Gellman, A. Koert, K. A. Dasse, R. J. Gilbert, B. P. Griffith, and Z. J. Wu, "Computational and experimental evaluation of the fluid dynamics and hemocompatibility of the CentriMag blood pump.," *Artif. Organs*, vol. 30, no. 3, pp. 168–77, Mar. 2006.

[24] W. K. Chan, Y. W. Wong, Y. Ding, L. P. Chua, and S. C. M. Yu, "Numerical investigation of the effect of blade geometry on blood trauma in a centrifugal blood pump.," *Artif. Organs*, vol. 26, no. 9, pp. 785–93, Sep. 2002.

[25] X. Song, H. G. Wood, and D. Olsen, "Computational Fluid Dynamics (CFD) Study of the 4th Generation Prototype of a Continuous Flow Ventricular Assist Device (VAD)," *J. Biomech. Eng.*, vol. 126, no. 2, p. 180, 2004.

[26] D. Arora, M. Behr, and M. Pasquali, "Hemolysis estimation in a centrifugal blood pump using a tensor-based measure.," *Artif. Organs*, vol. 30, no. 7, pp. 539–47, Jul. 2006.

[27] A. Arvand, N. Hahn, M. Hormes, M. Akdis, M. Martin, and H. Reul, "Comparison of hydraulic and hemolytic properties of different impeller designs of an implantable rotary blood pump by computational fluid dynamics.," *Artif. Organs*, vol. 28, no. 10, pp. 892–8, Oct. 2004.

[28] T. Yano, K. Sekine, A. Mitoh, Y. Mitamura, E. Okamoto, D.-W. Kim, I. Nishimura, S. Murabayashi, and R. Yozu, "An estimation method of hemolysis within an axial flow blood pump by computational fluid dynamics analysis.," *Artif. Organs*, vol. 27, no. 10, pp. 920–5, Oct. 2003.

[29] D. Arora, M. Behr, and M. Pasquali, "Hemolysis estimation in a centrifugal blood pump using a tensor-based measure.," *Artif. Organs*, vol. 30, no. 7, pp. 539–47, Jul. 2006.

[30] R. Paul, J. Apel, S. Klaus, F. Schügner, P. Schwindke, and H. Reul, "Shear stress related blood damage in laminar couette flow.," *Artif. Organs*, vol. 27, no. 6, pp. 517–29, Jun. 2003.

[31] G. Heuser and R. Opitz, "A Couette viscometer for short time shearing of blood.," *Biorheology*, vol. 17, no. 1–2, pp. 17–24, Jan. 1980.

[32] M. E. Taskin, K. H. Fraser, T. Zhang, C. Wu, B. P. Griffith, and Z. J. Wu, "Evaluation of Eulerian and Lagrangian models for hemolysis estimation.," *ASAIO J.*, vol. 58, no. 4, pp. 363–72.

[33] M. E. Taskin, K. H. Fraser, T. Zhang, C. Wu, B. P. Griffith, and Z. J. Wu, “Evaluation of Eulerian and Lagrangian models for hemolysis estimation.,” *ASAIO J.*, vol. 58, no. 4, pp. 363–72, 2012.

[34] L. B. Leverett, J. D. Hellums, C. P. Alfrey, and E. C. Lynch, “Red blood cell damage by shear stress.,” *Biophys. J.*, vol. 12, no. 3, pp. 257–73, Mar. 1972.

[35] S. S. Deshmukh, S. Vedantam, J. B. Joshi, and S. B. Koganti, “Computational Flow Modeling and Visualization in the Annular Region of Annular Centrifugal Extractor,” *Ind. Eng. Chem. Res.*, vol. 46, no. 25, pp. 8343–8354, Dec. 2007.

[36] P. Desevaux, “Numerical flow visualization of the formation of taylor cells in a laminar taylor-couette flow,” *J. Vis.*, vol. 12, no. 2, pp. 91–92, Jun. 2009.

Appendix

Matlab Code to read single particle data [2] , HO-Heuser Opitz constants

```
clear all; clc;

    pathFiles = ['time.txt' 0 0 0;
        'strain.txt' 0;
        'vel.txt' 0 0 0 0;
        'z.txt' 0 0 0 0 0 0;];

    j=0;
    maxNumDataPoints = 0;
    data= ones(200,5,1000)*NaN;
    for filestr=pathFiles'
        j=j+1;
        disp(filestr');
        file = fopen(filestr');
        %file = fopen('path_6_6000_vel.txt');
        fgets(file);%read in title
        fgets(file);%read in labels
        while not( feof(file) )
            fgets(file);%read in empty line
            particle = fscanf(file, '((xy/key/label \"particle-%i\")');
            flag = true;
            i=0;
            while(flag)
                i=1+i;
                if (i> maxNumDataPoints)
                     maxNumDataPoints=i;
                     data(:,:,i)= NaN;
                end
                [values,readNum]=fscanf(file,'%g\t%g',2);
                if readNum == 2
                    if j==1
                        data(particle,1,i)=values(1);%pathlength
                    end
                    data(particle,j+1,i)=values(2);%velocity
                else
                    flag = false;
                end
            end
            fgets(file);%read in ) line
        end
        fclose(file);
    end
```

```
   % Track Single particle


    mu=3.5e-3; % [Pa] Blood Viscosity
n=48;
i=3;
for i=1:n
    path(i,:)=data(i,1,:);
    time(i,:)=data(i,2,:);
    strain(i,:)=data(i,3,:);
    vel(i,:)=data(i,4,:);
    z(i,:)=data(i,5,:);
end
tau=mu*strain

figure (1) % z
plot( z(i,:), path(i,:)); hold on;  grid on;
ylabel('Path length [m]')
xlabel('Z position [m]')
title('Pathlength vs. Z')

figure (2) % exposure time
plot(z(i,:), time(i,:)); hold on; grid on;
xlabel('Z [m]')
ylabel('Residence time[sec]')
title('Residence along Z')

figure (3) % velocity
plot(z(i,:), vel(i,:)); hold on; grid on;
xlabel('Z [m]')
ylabel('Velocity [m/s]')
title('Velocity along Z')

figure (4) % strain rate
plot(z(i,:), strain(i,:)); hold on; grid on;
xlabel('Z [m]')
ylabel('Strain [1/s]')
title('Strain Rate along Z')
figure(5) % Shear Stress
plot(z(i,:),tau(i,:),'b'); grid on; hold on;
xlabel('Z [m]');    ylabel('Shear Stress [Pa]');
title('Scalar Shear Stress');

figure(6) % Threshold limit of Hemolysis
plot(time(i,:),tau(i,:),'b'); grid on; hold on;
xlabel('Residence Time [s]');    ylabel('Shear Stress [Pa]');
title('Shear Stress vs. Time');
```

```
figure(7) % Hemolysis model
for j=1:length(data)-1
    t(i,j)=time(i,j+1)-time(i,j);
    LA(i,j)=1.8e-6*(tau(i,j).^1.991).*(t(i,j)).^0.765;
end
plot(z(i,1:length(data)-1),abs(LA(i,:))); hold on; grid on;
xlabel('Z [m]');    ylabel('Blood Damage');
title('Lagrangian Approach along Z');
D=0; % integration of blood damage
 for j=1:length(data)-1
        if isnan(LA(i,j))
            LA(i,j)=0;
        end
    D=D+abs(LA(i,j));
 end
```

Matlab Code to read multiple particle data [2]**, HO- Heuser Opitz constants.**

```
clear all; clc;

    pathFiles = ['time.txt' 0 0 0;
        'strain.txt' 0;
        'vel.txt' 0 0 0 0;
        'z.txt' 0 0 0 0 0 0;];

    j=0;
    maxNumDataPoints = 0;
    data= ones(200,5,1000)*NaN;
    for filestr=pathFiles'
        j=j+1;
        disp(filestr');
        file = fopen(filestr');
        %file = fopen('path_6_6000_vel.txt');
        fgets(file);%read in title
        fgets(file);%read in labels
        while not( feof(file) )
            fgets(file);%read in empty line
            particle = fscanf(file, '((xy/key/label \"particle-%i\")');
            flag = true;
            i=0;
            while(flag)
```

```
                i=1+i;
                if (i> maxNumDataPoints)
                     maxNumDataPoints=i;
                     data(:,:,i)= NaN;
                end
                [values,readNum]=fscanf(file,'%g\t%g',2);
                if readNum == 2
                    if j==1
                        data(particle,1,i)=values(1);%pathlength
                    end
                    data(particle,j+1,i)=values(2);%velocity
                else
                    flag = false;
                end
            end
            fgets(file);%read in ) line
        end
        fclose(file);
    end


    %Ttrack Multiple particles


    mu=3.5e-3; % [Pa] Blood Viscosity
n=48;

for i=1:n
    path(i,:)=data(i,1,:);
    time(i,:)=data(i,2,:);
    strain(i,:)=data(i,3,:);
    vel(i,:)=data(i,4,:);
    z(i,:)=data(i,5,:);
end


figure (1) % z
for i= 1;n
path(i,:)= data(i,1,:);
plot( z(i,:), path(i,:)); hold on;  grid on;
end
ylabel('Path length [m]')
xlabel('Z position [m]')
title('Pathlength vs. Z')
```

```
figure (2) % exposure time
for i=1:n
z(i,:)=data(i,5,:);
time(i,:)=data(i,2,:);
plot(z(i,:), time(i,:)); hold on; grid on;
end
xlabel('Z [m]')
ylabel('Residence time [sec]')
title('Residence time along Z')

figure (3) % velocity
for i=1:n
vel(i,:)=data(i,4,:);
plot(z(i,:), vel(i,:)); hold on; grid on;
end
xlabel('Z [m]')
ylabel('Velocity [m/s]')
title('Velocity along Z')

figure (4) % strain rate
for i= 1;n
strain(i,:)=data(i,3,:);
plot(z(i,:), strain(i,:)); hold on; grid on;
end
xlabel('Z [m]')
ylabel('Strain [1/s]')
title('Strain Rate along Z')


figure(5) % Shear Stress
tau=mu*strain
for i= 1:n
plot(z(i,:),tau(i,:),'b'); grid on; hold on;
end
xlabel('Z [m]');    ylabel('Shear Stress [Pa]');
title('Scalar Shear Stress');

figure(6) % Threshold limit of Hemolysis
for i=1:n
plot(time(i,:),tau(i,:),'b'); grid on; hold on;
end
xlabel('Residence Time [s]');    ylabel('Shear Stress [Pa]');
title('Shear Stress vs. Time');

figure(7) % Hemolysis model
for i=1:n
for j=1:length(data)-1
```

```
    t(i,j)=time(i,j+1)-time(i,j);
    LA(i,j)=1.8e-6*(tau(i,j).^1.991).*(t(i,j)).^0.765;
end
plot(z(i,1:length(data)-1),abs(LA(i,:))); hold on; grid on;
end
xlabel('Z [m]');    ylabel('Blood Damage');
title('Lagrangian Approach along Pathline');
D=0; % integration of blood damage
for i=1:n
 for j=1:length(data)-1
        if isnan(LA(i,j))
            LA(i,j)=0;
        end
    D=D+abs(LA(i,j));
 end
end
 D=D/n;
```

Matlab Code to read multiple particle data [2]**, GW- Giersiepen Wurzinger constants**

```
clear all; clc;

    pathFiles = ['time.txt' 0 0 0;
        'strain.txt' 0;
        'vel.txt' 0 0 0 0;
        'z.txt' 0 0 0 0 0 0;];

    j=0;
    maxNumDataPoints = 0;
    data= ones(200,5,1000)*NaN;
    for filestr=pathFiles'
        j=j+1;
        disp(filestr');
        file = fopen(filestr');
        %file = fopen('path_6_6000_vel.txt');
        fgets(file);%read in title
        fgets(file);%read in labels
        while not( feof(file) )
            fgets(file);%read in empty line
            particle = fscanf(file, '((xy/key/label \"particle-%i\")');
            flag = true;
            i=0;
            while(flag)
                i=1+i;
                if (i> maxNumDataPoints)
                     maxNumDataPoints=i;
```

```
                    data(:,:,i)= NaN;
                end
                [values,readNum]=fscanf(file,'%g\t%g',2);
                if readNum == 2
                    if j==1
                        data(particle,1,i)=values(1);%pathlength
                    end
                    data(particle,j+1,i)=values(2);%velocity
                else
                    flag = false;
                end
            end
            fgets(file);%read in ) line
        end
        fclose(file);
    end


    %Ttrack Multiple particles


    mu=3.5e-3; % [Pa] Blood Viscosity
n=48;

for i=1:n
    path(i,:)=data(i,1,:);
    time(i,:)=data(i,2,:);
    strain(i,:)=data(i,3,:);
    vel(i,:)=data(i,4,:);
    z(i,:)=data(i,5,:);
end


figure (1) % z
for i= 1;n
path(i,:)= data(i,1,:);
plot( z(i,:), path(i,:)); hold on;  grid on;
end
ylabel('Path length [m]')
xlabel('Z position [m]')
title('Pathlength vs. Z')


figure (2) % exposure time
for i=1:n
z(i,:)=data(i,5,:);
```

```
time(i,:)=data(i,2,:);
plot(z(i,:), time(i,:)); hold on; grid on;
end
xlabel('Z [m]')
ylabel('Exposure time [sec]')
title('Exposure time along Z')

figure (3) % velocity
for i=1:n
vel(i,:)=data(i,4,:);
plot(z(i,:), vel(i,:)); hold on; grid on;
end
xlabel('Z [m]')
ylabel('Velocity [m/s]')
title('Velocity along Z')

figure (4) % strain rate
for i= 1;n
strain(i,:)=data(i,3,:);
plot(z(i,:), strain(i,:)); hold on; grid on;
end
xlabel('Z [m]')
ylabel('Strain [1/s]')
title('Strain Rate along Z')


figure(5) % Shear Stress
tau=mu*strain
for i= 1:n
plot(z(i,:),tau(i,:),'b'); grid on; hold on;
end
xlabel('Z [m]');    ylabel('Shear Stress [Pa]');
title('Scalar Shear Stress');

figure(6) % Threshold limit of Hemolysis
for i=1:n
plot(time(i,:),tau(i,:),'b'); grid on; hold on;
end
xlabel('Residence Time [s]');    ylabel('Shear Stress [Pa]');
title('Shear Stress vs. Time');

figure(7) % Hemolysis model
for i=1:n
for j=1:length(data)-1
    t(i,j)=time(i,j+1)-time(i,j);
    LA(i,j)=3.62e-5*(tau(i,j).^2.416).*(t(i,j)).^0.785;
end
```

```
plot(z(i,1:length(data)-1),abs(LA(i,:))); hold on; grid on;
end
xlabel('Z [m]');    ylabel('Blood Damage');
title('Lagrangian Approach along Pathline');
D=0; % integration of blood damage
for i=1:n
 for j=1:length(data)-1
        if isnan(LA(i,j))
            LA(i,j)=0;
        end
    D=D+abs(LA(i,j));
 end
end
 D=D/n;
```

Matlab Code to read multiple particle data [2]**, TZ- Taskin Zhang constants**

```
clear all; clc;

    pathFiles = ['time.txt' 0 0 0;
        'strain.txt' 0;
        'vel.txt' 0 0 0 0;
        'z.txt' 0 0 0 0 0 0;];

    j=0;
    maxNumDataPoints = 0;
    data= ones(200,5,1000)*NaN;
    for filestr=pathFiles'
        j=j+1;
        disp(filestr');
        file = fopen(filestr');
        %file = fopen('path_6_6000_vel.txt');
        fgets(file);%read in title
        fgets(file);%read in labels
        while not( feof(file) )
            fgets(file);%read in empty line
            particle = fscanf(file, '((xy/key/label \"particle-%i\")');
            flag = true;
            i=0;
            while(flag)
                i=1+i;
                if (i> maxNumDataPoints)
                     maxNumDataPoints=i;
```

```
                    data(:,:,i)= NaN;
                end
                [values,readNum]=fscanf(file,'%g\t%g',2);
                if readNum == 2
                    if j==1
                        data(particle,1,i)=values(1);%pathlength
                    end
                    data(particle,j+1,i)=values(2);%velocity
                else
                    flag = false;
                end
            end
            fgets(file);%read in ) line
        end
        fclose(file);
    end


    %Ttrack Multiple particles


    mu=3.5e-3; % [Pa] Blood Viscosity
n=48;

for i=1:n
    path(i,:)=data(i,1,:);
    time(i,:)=data(i,2,:);
    strain(i,:)=data(i,3,:);
    vel(i,:)=data(i,4,:);
    z(i,:)=data(i,5,:);
end


figure (1) % z
for i= 1;n
path(i,:)= data(i,1,:);
plot( z(i,:), path(i,:)); hold on;  grid on;
end
ylabel('Path length [m]')
xlabel('Z position [m]')
title('Pathlength vs. Z')


figure (2) % exposure time
for i=1:n
z(i,:)=data(i,5,:);
```

```
time(i,:)=data(i,2,:);
plot(z(i,:), time(i,:)); hold on; grid on;
end
xlabel('Z [m]')
ylabel('Exposure time [sec]')
title('Exposure time along Z')

figure (3) % velocity
for i=1:n
vel(i,:)=data(i,4,:);
plot(z(i,:), vel(i,:)); hold on; grid on;
end
xlabel('Z [m]')
ylabel('Velocity [m/s]')
title('Velocity along Z')

figure (4) % strain rate
for i= 1;n
strain(i,:)=data(i,3,:);
plot(z(i,:), strain(i,:)); hold on; grid on;
end
xlabel('Z [m]')
ylabel('Strain [1/s]')
title('Strain Rate along Z')


figure(5) % Shear Stress
tau=mu*strain
for i= 1:n
plot(z(i,:),tau(i,:),'b'); grid on; hold on;
end
xlabel('Z [m]');    ylabel('Shear Stress [Pa]');
title('Scalar Shear Stress');

figure(6) % Threshold limit of Hemolysis
for i=1:n
plot(time(i,:),tau(i,:),'b'); grid on; hold on;
end
xlabel('Residence Time [s]');    ylabel('Shear Stress [Pa]');
title('Shear Stress vs. Time');

figure(7) % Hemolysis model
for i=1:n
for j=1:length(data)-1
    t(i,j)=time(i,j+1)-time(i,j);
    LA(i,j)=1.228e-5*(tau(i,j).^1.9918).*(t(i,j)).^0.6606;
end
```

```
plot(z(i,1:length(data)-1),abs(LA(i,:))); hold on; grid on;
end
xlabel('Z [m]');    ylabel('Blood Damage');
title('Lagrangian Approach along Pathline');
D=0; % integration of blood damage
for i=1:n
 for j=1:length(data)-1
        if isnan(LA(i,j))
            LA(i,j)=0;
        end
    D=D+abs(LA(i,j));
 end
end
 D=D/n;
```